ADVANCED MONTE CARLO METHODS for ANALYSIS of VERY HIGH TEMPERATURE REACTORS: ON-THE-FLY DOPPLER BROADENING and DETERMINISTIC/MONTE CARLO METHODS

by

Gokhan Yesilyurt

A dissertation submitted in partial fulfillment
of the requirements for the degree of
Doctor of Philosophy
(Nuclear Engineering and Radiological Sciences)
in The University of Michigan
2009

Doctoral Committee:

Professor William R. Martin, Chair
Professor Iain D. Boyd
Professor Thomas J. Downar
Professor John C. Lee
Forrest B. Brown, Los Alamos National Laboratory

To my family Ozlem, Batu and Ata
For their love, patience, and understanding

ACKNOWLEDGEMENTS

I would like to express profound gratitude to my advisor, Professor William R. Martin, for his support, assistance, encouragement, supervision, and suggestions throughout my research at the University of Michigan. His moral support and continuous guidance let me finish my work successfully. I am also very grateful to Doctor Forrest B. Brown and Professor John C. Lee for their valuable guidance and assistance in this dissertation. I also wish to thank Professors Thomas J. Downar and Iain D. Boyd for serving on my doctoral committee.

I also would like to thank my colleagues Shikha Prasad, Wei Ji, Kaushik Banerjee, Jeremy L. Conlin, Eva Sunny and Benjamin Robert Betzler for their friendship and many helpful discussions on my research.

I am as ever, especially indebted to my parents, Mr. Nuri and Mrs. Hulya Yesilyurt for their love and support throughout my life.

My biggest thanks go to my wife, Ozlem Yesilyurt, whose positive, informed, and encouraging nature has been an inspiration throughout. I am also indebted to my children Batu and Ata Yesilyurt for their patience during my time at the University of Michigan.

This study was supported by the DOE NERI grant DE-FC07-06ID14745.

TABLE OF CONTENTS

LIST OF TABLES

LIST OF FIGURES

ABSTRACT

Two of the primary challenges associated with the neutronic analysis of the Very High Temperature Reactor (VHTR) are accounting for resonance self-shielding in the particle fuel (contributing to the double heterogeneity) and accounting for temperature feedback due to Doppler broadening. The research reported in this thesis addresses both of these challenges. The double heterogeneity challenge is addressed by defining a "double heterogeneity factor" (DHF) that allows conventional light water reactor (LWR) lattice physics codes to analyze VHTR configurations. The challenge of treating Doppler broadening is addressed by a new "on-the-fly" methodology that is applied during the random walk process with negligible impact on computational efficiency. Although this methodology was motivated by the need to treat temperature feedback in a VHTR, it is applicable to any reactor design.

With the on-the-fly Doppler method, the Monte Carlo code only requires 0K cross sections for each isotope. This method broadens the 0K cross sections for any isotope in the library to any temperature in the range 77K-3200K. The methodology is based on a combination of Taylor series expansions and asymptotic series expansions. The type of series representation was determined by investigating the temperature dependence of U238 resonance cross sections in three regions: near the resonance peaks, mid-resonance, and the resonance wings. The coefficients for these series expansions were determined by

regressions over the energy and temperature range of interest. The comparison of the broadened cross sections using this methodology with the NJOY cross sections was excellent over the entire temperature range (77K-3200K) and energy range. A Monte Carlo code was implemented to apply the combined regression model and used to estimate the additional computing cost which was found to be less than 1%.

The DHF accounts for the effect of the particle heterogeneity on resonance absorption in particle fuel. The first level heterogeneity posed by the VHTR fuel particles is a unique characteristic that cannot be accounted for by conventional LWR lattice physics codes. On the other hand, Monte Carlo codes can take into account the detailed geometry of the VHTR including resolution of individual fuel particles without performing any type of resonance approximation. Furthermore, resonance cross-shielding effects due to the presence of different strong absorber nuclides can be accounted for by Monte Carlo codes, eliminating the need for approximate methods to treat this effect. The DHF accounts for all these effects, basically allowing a conventional LWR lattice physics code to analyze a VHTR configuration with accuracy comparable to Monte Carlo code. The DHF, basically a self shielding factor, was found to be weakly dependent on space and fuel depletion. The DHF only depends strongly on the packing fraction in a fuel compact. Therefore, it is proposed that DHFs be tabulated as a function of packing fraction to analyze the heterogeneous fuel in VHTR configuration with LWR lattice physics codes.

CHAPTER 1

INTRODUCTION

Very High Temperature Reactors (VHTRs) are very challenging for reactor analysts. The particle fuel, actually a stochastic mixture of tiny particles, leads to the well-known double heterogeneity, which is a substantial effect (~10% on k_{eff}) that must be accounted for. Monte Carlo methods can be used to treat this effect but deterministic methods, such as advanced lattice physics codes that are used for light water reactor (LWR) analysis, cannot account for this effect without substantial changes to the methodology to account for transport in a binary stochastic mixture. This work has led to the coupling of Monte Carlo methods and LWR lattice physics codes to analyze VHTR configurations, accounting for the double heterogeneity. In addition, the strong temperature feedback in a VHTR, primarily due to Doppler broadening of the resonance cross sections, poses another challenge for the coupled neutronic-thermal-hydraulic (NTH) analysis of a VHTR, because conventional methodology to account for temperature changes during the NTH iterations is not practical for realistic VHTR configurations. This temperature effect is complicated by the double heterogeneity. The difficulty of treating Doppler broadening of cross sections in VHTR configurations led to the development of the on-the-fly Doppler method for Monte Carlo codes, and this methodology can be used for other reactor types as well. This thesis will address these two methodologies that have been developed for the accurate and efficient neutronic analysis of VHTRs.

The gas cooled reactor concept has been studied by several countries since the 1950s. The DRAGON, Peach Bottom, and AVR pebble-bed reactors were operated successfully in the 1960s in England, the United States and Germany, respectively. These earlier designs finally led to a commercial design known as the High Temperature Gas-cooled Reactor (HTGR). The Fort St. Vrain Generating Station was operated as an HTGR from 1979 to 1989 in the United States and decommissioned due to economic factors. Today, the improved design known as the VHTR is among the Generation IV[1] reactor concepts.

The VHTR is a graphite-moderated, helium-cooled reactor with a once-through uranium fuel cycle. Its design was selected as one of the most promising concepts to meet the Generation IV goals in the areas of economics, safety, reliability, sustainability and hydrogen production. Generation IV nuclear systems are planned to reach technical maturity by 2030.

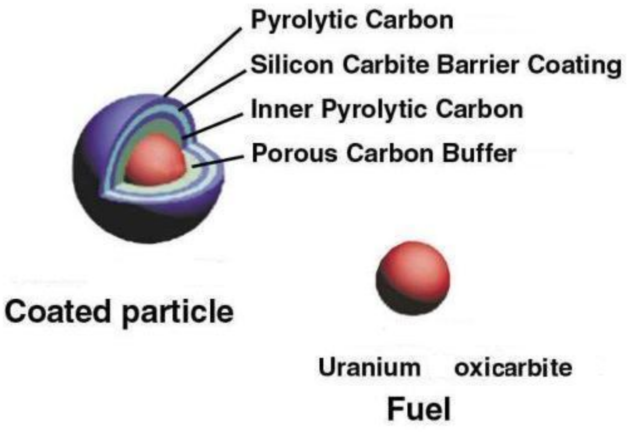

Figure 1.1. Coated microsphere fuel particle.

The first level of the double heterogeneity is due to the fuel particles which are randomly distributed in the fuel compacts for the prismatic design or in the fuel pebbles for the pebble-bed design. The second level of the double heterogeneity is represented by spatial distribution of the fuel compacts in fuel blocks for the prismatic design or fuel pebbles in reactor core for the pebble-bed design. The second level of the double heterogeneity is similar to the fuel pin heterogeneity in a LWR. The resultant double heterogeneous system is a unique characteristic of the VHTR. The construction of the prismatic reactor core starting from the microspheres is shown in Figure 1.2.

Figure 1.2. The construction stages of the prismatic VHTR core.

1.1 Challenges in VHTR Analysis

For realistic, detailed reactor calculations, Monte Carlo codes are part of a multi-physics simulation involving thermal-hydraulic feedback to adjust temperatures and densities which in turn affects the neutronic analysis. This process can result in 10,000s of material temperatures in LWRs when broadened cross sections are needed. The number of material regions becomes much higher for VHTR configurations due to the need to resolve the particle fuel. Existing Monte Carlo codes (e.g., MCNP[2]) were not designed to accommodate this need. Therefore, a new closed-form formulation in temperature was derived to allow on-the-fly Doppler broadening of the cross sections during the random walk of the neutrons for an unlimited number of material temperatures while maintaining a modest computing cost and at the same time accounting for resonance overlapping effects between closely spaced resonances in the keV range.

The second challenge, accounting for the double heterogeneity without resorting to full core Monte Carlo analysis, has been addressed with a coupled Monte Carlo/deterministic approach that enables a conventional LWR lattice physics code to analyze VHTR configurations. The first level heterogeneity posed by the VHTR fuel particles cannot be accounted for by traditional LWR lattice physics codes as they cannot resolve the individual fuel particles. Consequently, a new methodology has been developed to analyze VHTR fuel correctly and efficiently, accounting for the double heterogeneity. This will allow VHTR analysts to take advantage of the highly developed capabilities of lattice physics codes available for LWR neutronic analysis, including depletion and coupling to 3D nodal codes for efficient full core simulation.

1.1.1 Doppler Broadening of Cross Sections for Monte Carlo Codes

Doppler broadening of nuclear cross sections is one of the most important phenomena during nuclear reactor operation and has important implications for reactor safety. Resonance capture and fission cross sections change significantly due to the relative motion between the incoming neutron and the target nucleus. As the material temperature increases, a wider range of relative energy is generated due to the increase in the motion of the target nuclei. Summed over all resonance energies, the overall effect of the increased Doppler broadening at higher temperatures is to increase the total resonance absorption (or fission) in the material region, hence giving a strong neutronic feedback as a result of temperature changes.

Low lying resonances (i.e., in the eV range) of the strong absorber nuclides are widely spaced, whereas they are closely spaced in the keV range. As the temperature increases, resonances in the keV range may overlap (interfere) with each other. For example, two adjacent, but resolved, resonances at low temperature may merge together when broadened to a higher temperature. The evolution of the U-238 total cross section with temperature in the low and high energy regions is illustrated in Figure 1.3.

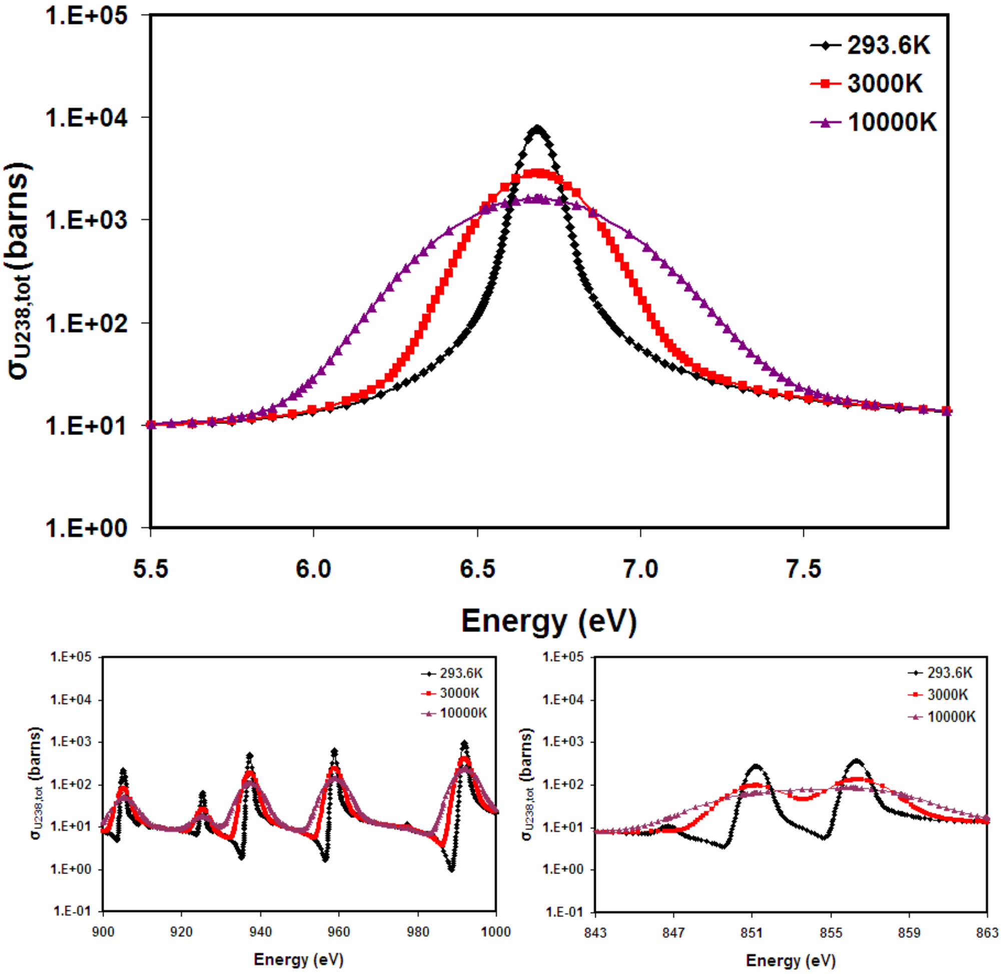

Figure 1.3. Evolution of σ_{tot}^{U238} with temperature.

The traditional approach to obtain the Doppler broadened cross sections for use in continuous energy Monte Carlo codes is based on the interpolation of cross section libraries generated at reference temperature points. This approach was found to be prohibitively memory expensive and not practical for applications involving thermal-hydraulic feedback.

Other methods, based on the direct use of resonance parameters to broaden the cross sections, are not accurate enough. As an alternative approach, utilization of the exact Doppler broadening equation in Monte Carlo codes was found during the course of this research to be very expensive.

The methods summarized above are not practical and/or do not provide sufficient accuracy. Computing time and memory requirement can be prohibitively large for realistic reactor configurations. Details on these existing Doppler broadening methods will be presented in the next Chapter.

1.1.2 Representation of the Double Heterogeneity in Lattice Physics Codes

In LWR lattice physics codes, resonance integrals for the strong absorber nuclides are calculated by using approximate methods for a homogeneous mixture of fuel regions, ignoring the pronounced self-shielding effect due to the randomly dispersed fuel particles in the fuel compacts. On the other hand, any physical model with complicated geometry features can be explicitly represented by Monte Carlo codes (e.g. MCNP) accurately, including the resolution of fuel particles for VHTR configurations.

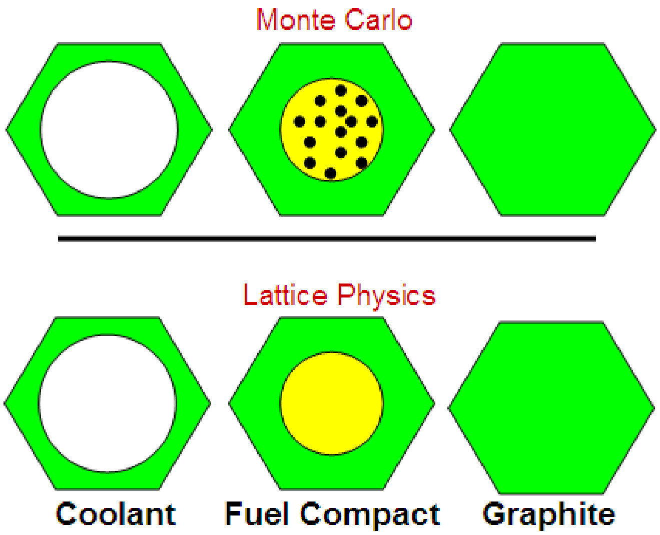

Figure 1.4. Comparison of modeling features: Monte Carlo vs. lattice physics codes.

Furthermore, resonance cross-shielding effects due to the presence of different strong absorber nuclides can be accounted for by Monte Carlo codes, eliminating the need for approximate methods to treat this effect. It should also be noted that multi-group cross sections used by lattice physics codes are obtained using a generic weighting spectrum with an approximate resonance model for the resonance cross sections. Monte Carlo codes eliminate the need to use approximate resonance models since they can in principle model the exact geometry with the exact physics, to the extent these quantities are known. Therefore, inconsistencies in multi-group cross sections due to assumed weighting functions, resonance approximation models and multi-group energy structures are avoided.

As long as the continuous energy nuclear data is correct, Monte Carlo codes can calculate the shielded cross sections with excellent accuracy for all detailed geometries, provided there is a sufficient number of histories to obtain acceptable statistics. On the other hand, the computing cost of the Monte Carlo simulations can be very prohibitive to perform a full core neutronic analysis as a function of depletion. Therefore, effort has been focused on developing an accurate and efficient methodology to allow a conventional LWR lattice physics code to analyze VHTR fuel with the help of Monte Carlo codes, accounting for the double heterogeneity due to TRIstructural-ISOtropic (TRISO) fuel. Previous methods to account for the double heterogeneity will be presented in the next Chapter.

CHAPTER 2

LITERATURE SURVEY

2.1 Doppler Broadening of Cross Sections for Monte Carlo Codes

Current Monte Carlo particle transport codes rely on the nuclear data files generated at specific reference temperatures. These temperature dependent nuclear data files are generated by the Nuclear Data Processing (NDP) codes such as NJOY[3] which can produce temperature dependent point-wise and multi-group cross sections and related quantities from evaluated nuclear data in the ENDF format. Doppler broadening of the cross sections in NJOY can be performed based on either the exact Doppler broadening equation developed by Cullen[4] or direct use of resonance parameters. We have found that the former approach is not practical for realistic configurations while the latter approach is not very accurate.

2.1.1 Exact Doppler Broadening Equation

The well-known Doppler broadening equation developed by Cullen[4] is given in Eq. (2.1). It is equally applicable to neutron or charged particles.

$$\sigma\left(y,T_2\right)=\frac{1}{y^2}\left(\frac{1}{\pi}\right)^{\frac{1}{2}}\int_0^{\infty}\sigma\left(x,T_1\right)x^2\left\{\exp\left[-\left(x-y\right)^2\right]-\exp\left[-\left(x+y\right)^2\right]\right\}dx \qquad (2.1)$$

where x, y, α , and β are defined as:

$$x^2 = \alpha E_r = \beta V_r^2 \tag{2.2}$$

$$y^2 = \alpha E = \beta V^2 \tag{2.3}$$

$$\alpha = \frac{A}{k\left(T_2 - T_1\right)} \tag{2.4}$$

$$\beta = \frac{M_t}{2k\left(T_2 - T_1\right)} \tag{2.5}$$

where M_t is the target nuclei mass, M_p is the projectile mass, A is the weight ratio (M_t/M_p), k is Maxwell-Boltzmann's constant, $\sigma\left(x,T_1\right)$ is the base cross section at T_1 and $\sigma\left(y,T_2\right)$ is the Doppler broadened cross section at T_2. The velocity-like terms y and x are related with incoming neutron velocity V and relative velocity V_r respectively. Relative velocity is defined as $V_r = |V - V_t|$ where V_t is the target nucleus velocity. E and E_r are the incoming neutron energy and relative energy, respectively.

The derivation of the exact Doppler broadening Eq. (2.1) begins with the definition of reaction rate, $R\left(V,T\right) = V\sigma\left(V,T\right) = \int\limits_{all\ V_t} V_r\sigma\left(V_r,0\right)P\left(V_t\right)dV_t$ where the cross sections are defined to conserve the observed reaction rates, and $P\left(V_t\right)$ is the normalized Maxwell-Boltzmann distribution.

The numerical discretization of Eq. (2.1) allows us to calculate Doppler broadened cross sections of any type at T_2 based on the reference cross sections generated at T_1. It is assumed that the cross sections are given as a table of energy versus cross section with linear-linear interpolation in energy and cross section between tabulated values. Exact Doppler broadening of the cross sections, as given in Eq. (2.1), is performed in NJOY with the BROADR module. Cross sections can be broadened based on nuclear data at 0K (default) or higher temperatures. 0K cross sections are usually generated by using multi-level resonance representations (e.g. Multilevel Breit-Wigner, Reich-Moore, Adler-Adler, etc…) for strong resonance absorbers.

However, as will be shown in detail in the next chapter, the discretized form of the exact Doppler broadening expression in Eq. (2.1) requires an unacceptable computing time due to the cost of evaluating complementary error functions. Therefore, exact Doppler broadening of the cross sections during the random walk of the neutrons in Monte Carlo codes is not practical.

2.1.2 PSI-CHI Representation

The psi-chi method[5,6,7] is the only single level resonance representation where Doppler broadening of cross sections can be performed based on the resonance parameters in NJOY. For large values of neutron energy, this model assumes that the second exponential can be ignored in Eq. (2.1). However, this approximation overestimates the Doppler-broadened cross sections for lower values of neutron energy. Secondly, since the significant contribution to the remaining integral usually comes from a very narrow range of E$_r$ close to E, it is also assumed that $\sqrt{E_r}$ can be expanded in Taylor series about E. Ignoring the higher terms leads to the following equation, where the error introduced increases with decreasing energy:

$$\alpha\left(\sqrt{E_r}-\sqrt{E}\right)^2 \approx \left[\left(E_r-E\right)/\Delta\right]^2 \qquad (2.6)$$

where Δ and ΔT are defined as:

$$\Delta = 2\left(E_A/\alpha\right)^{1/2} = \left(4k\Delta T E_A/A\right)^{1/2} \qquad (2.7)$$

$$\Delta T = T_2 - T_1 \qquad (2.8)$$

The last approximation introduced for the psi-chi method is to change the lower limit of integration to $-\infty$, assuming that the interval $(-\infty,0)$ has negligible contribution to the integral:

$$\sqrt{E}\sigma(E,T_2)=\frac{1}{\Delta\sqrt{\pi}}\int_{-\infty}^{\infty}\sqrt{E_r}\sigma(E_r,T_1)\exp\left\{-\left[\frac{(E_r-E)}{\Delta}\right]^2\right\}dE_r \tag{2.9}$$

The psi-chi method also assumes that the 0K cross sections are composed of a series of single-level Breit-Wigner resonances:

$$\sigma_{cap,fis}(E,0)=(E_R/E)^{1/2}\frac{(\Gamma_T/2)A}{(\Gamma_T/2)^2+(E-E_R)^2} \tag{2.10}$$

$$\sigma_{scat}(E,0)=\frac{(\Gamma_T/2)A}{(\Gamma_T/2)^2+(E-E_R)^2}+\frac{B(E-E_R)}{(\Gamma_T/2)^2+(E-E_R)^2} \tag{2.11}$$

where E_R, Γ_T, and B are resonance energy, total resonance width, and elastic interface strength, respectively. Therefore, the Doppler-broadened cross sections become:

$$\sigma_{cap,fis}(E,T)=\left(\frac{2}{\Gamma_T}\right)\left(\frac{E_R}{E}\right)^{1/2}A\psi(x,\xi_R) \tag{2.12}$$

$$\sigma_{scat}(E,T)=\left(\frac{2}{\Gamma_T}\right)\left[A\psi(x,\xi_R)+B\chi(x,\xi_R)\right] \tag{2.13}$$

where $\psi(x,\xi_R)$ and $\chi(x,\xi_R)$ are defined as;

$$\psi(x,\xi_R)=\frac{\xi_R}{2\sqrt{\pi}}\int_{-\infty}^{\infty}\exp\left\{-\left[\frac{(x-y)}{2}\xi_R\right]^2\right\}\frac{dy}{y^2+1} \tag{2.14}$$

$$\chi(x,\xi_R)=\frac{\xi_R}{2\sqrt{\pi}}\int_{-\infty}^{\infty}\exp\left\{-\left[\frac{(x-y)}{2}\xi_R\right]^2\right\}\frac{ydy}{y^2+1} \tag{2.15}$$

The line shapes $\psi(x,\xi_R)$ and $\chi(x,\xi_R)$ are given in terms of complex functions in the MC^2 code[8]:

$$\psi\left(x,\xi_R\right)=\frac{\xi_R}{2\sqrt{\pi}}\operatorname{Re}\left\{\exp\left(\left[i\frac{\left(x+i\right)}{2}\xi_R\right]^2\right)erfc\left(-i\frac{\left(x+i\right)}{2}\xi_R\right)\right\} \tag{2.16}$$

$$\chi\left(x,\xi_R\right)=\frac{\xi_R}{2\sqrt{\pi}}\operatorname{Im}\left\{\exp\left(\left[i\frac{\left(x+i\right)}{2}\xi_R\right]^2\right)erfc\left(-i\frac{\left(x+i\right)}{2}\xi_R\right)\right\} \tag{2.17}$$

where ξ_R, x, and y are defined as:

$$\xi_R \approx \Gamma_T / \Delta_R = \Gamma_T\left(A/4kTE_R\right)^{1/2} \tag{2.18}$$

$$x = 2\left(E_r - E_R\right)/\Gamma_T \tag{2.19}$$

$$y = 2\left(E - E_R\right)/\Gamma_T \tag{2.20}$$

The psi-chi method is not as accurate as the exact Doppler broadening equation because the terms important for energies less than about $16kT/A$ are neglected. More importantly, cross sections in current evaluations are not represented as a series of single-level Breit-Wigner resonances. Strong absorber nuclides use resonance formulations that differ from the single-level representations (e.g., multilevel Breit-Wigner, Reich-Moore, Adler-Adler, etc…). In the case of light nuclides, cross sections are usually tabulated functions or do not use resonance parameters.

2.1.3 TEMPO Representation

In the TEMPO method[9,10], $\sqrt{E}\sigma(E,T_1)$ is assumed to be a tabulated function with linear-linear variation in energy:

$$\sqrt{E}\sigma(E,T_2) = \frac{1}{\Delta\sqrt{\pi}}\int_0^{\infty}\sqrt{E_r}\sigma(E_r,T_1)\exp\left\{-\left[\frac{(E_r - E)}{\Delta}\right]^2\right\}dE_r \qquad (2.21)$$

So the Doppler-broadened reaction rate can be written as follows:

$$R(E,T_2) = \frac{1}{\Delta\sqrt{\pi}}\sum_k\int_{E_k}^{E_{k+1}}(P_k + Q_k E_r)\exp\left\{-\left[\frac{(E_r - E)}{\Delta}\right]^2\right\}dE_r \qquad (2.22)$$

where Q_k and P_k are defined as:

$$Q_k = \left[\frac{R(E_{k+1},T_1) - R(E_k,T_1)}{E_{k+1} - E_k}\right] \qquad (2.23)$$

$$P_k = R(E_k,T_1) - Q_k E_k \qquad (2.24)$$

Introducing $x = (E - E_r)/\Delta$, the integration of Eq. (2.22) yields:

$$R(E,T_2) = \frac{1}{2}\sum_k\left\{(P_k + Q_k E)\left[ERF(x_{k+1}) - ERF(x_k)\right] + \frac{\Delta}{\sqrt{\pi}}\left[\exp(-x_k^2) - \exp(-x_{k+1}^2)\right]\right\} \qquad (2.25)$$

This algorithm has the same limitations as the psi-chi method.

2.1.4 Other Approximate Methods

Another approach, proposed by Marable[11] of Oak Ridge National Laboratory (ORNL) in the 1960s, requires resonance parameters in order to Doppler broaden the cross sections and was based on the psi-chi resonance representation. Therefore, this approach inherits all of the approximations inherent in the psi-chi approach mentioned above.

An alternative method that has been used frequently is based on the interpolation of the cross sections at the temperature of interest T between the nuclear data files generated by NJOY at bracketing reference temperatures, e.g., $T_1 < T < T_2$. A detailed study was performed by Trumbull[12] from Knolls Atomic Power Laboratory (KAPL) by applying several different interpolation schemes over various temperature intervals. Interpolated cross sections at intermediate temperatures were compared to NJOY Doppler broadened results for the same temperature. Differences relative to the Doppler broadened results were calculated in order to judge the suitability of the interpolation scheme and temperature interval. Since the exact Doppler broadening equation given in Eq. (2.1) does not admit a simple interpolation scheme, five different interpolation schemes were applied, including linear-linear, log-log, sqrt-linear, linear-log and sqrt-log in temperature and cross section respectively. The study showed that cross sections can be interpolated within an accuracy of 0.1% over a temperature interval of 111 K for light nuclides such as H-1, B-10, and O-16. Smaller temperature intervals were required for nuclides with more complex resonance behavior. Some values of the interpolated cross sections for natural Zr, U-238, and U-235 remain greater than the target 0.1% relative difference even with a 28K interval, suggesting that a smaller interval is necessary for these nuclides. It was shown that all of the proposed interpolation schemes were not found to be within the target 0.1% maximum relative difference with 28K interval for U-238. Log-log interpolation was found to be the best scheme among the others, resulting in 0.296% maximum relative difference (well beyond the target 0.1% accuracy) with 28K intervals for U-238.

The third approach, developed by Conlin[13], was the pseudo material construct which depends on the interpolation of cross section libraries at a few temperature points generated by the NJOY code. As temperature increases, the width of a given resonance varies as a function of $\sqrt{T}$. Therefore, the pseudo number density fractions, f_L and f_H, for the low and the high temperature cross sections for a given nuclide can be calculated as follows;

$$f_L = \frac{\sqrt{T_H} - \sqrt{T}}{\sqrt{T_H} - \sqrt{T_L}} \tag{2.26}$$

$$f_H = \left(1 - f_L\right) \tag{2.27}$$

where $T_L < T < T_H$. A cross-section for pseudo material at T becomes;

$$\Sigma\left(T\right) = f_L\,\Sigma\left(T_L\right) + \left(1 - f_L\right)\Sigma\left(T_H\right) \tag{2.28}$$

The number density fractions can be interpreted as fractional pseudo material densities and allow one to interpolate the cross sections between high and low temperature nuclear data files (NDFs) with $\sqrt{T}$ dependence. The interpolation is performed by the MCNP input processor which is tantamount to a stochastic mixing of the two cross section fields.

As in the previous methodology developed by Trumbull, the pseudo material approach depends on using pre-generated nuclear data files at fine temperature intervals. As the number of the resonance materials increases for a given problem, the size of the nuclear data that should be loaded in the memory may be unacceptable for the Monte Carlo calculations.

Finally, an integral representation for the Doppler broadening function $\psi\left(x, \xi_R\right)$ was proposed by Goncalves[14] to obtain an analytical solution based on elementary functions by using the Fourier cosine transform. The final form of the equation was found to be the same as the $\psi\left(x, \xi_R\right)$ function in terms of complex probability function as reported in MC^2 and NJOY manuals.

All of the methods summarized above to Doppler broaden cross sections for reactor physics applications are not practical and/or do not provide sufficient accuracy. They also require unacceptable amounts of storage, memory space, and computing time for realistic nuclear reactor configurations.

2.2 Double Heterogeneity Treatment for Lattice Physics Codes

Recent versions of the codes such as SCALE and WIMS have the capability of analyzing the double heterogeneity posed by the VHTR fuel. The SCALE code uses the Nordheim Integral Method[15] to calculate shielded group cross sections while WIMS uses equivalence theory. Both of these methods are approximate and assume a two region geometry for the microsphere and surrounding graphite.

An alternative method, called reactivity-equivalent physical transformation[16] (RPT), was developed to account for the particle level heterogeneity posed by the VHTR fuel. Volumetric homogenization of the fuel compact region, including fuel particles and binder, overestimates the absorption and underestimates the reactivity due to reduced self-shielding of the fuel. The RPT method was developed without modeling a fuel particle explicitly. In this method, the fuel region was represented by an equivalent cell of two homogeneous zones:

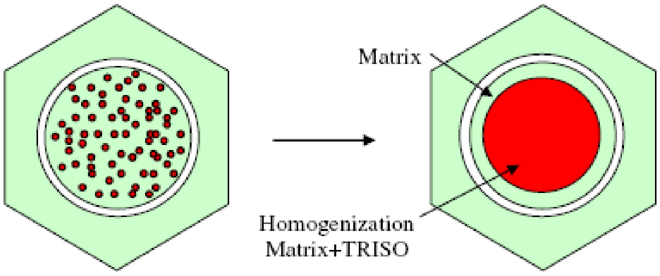

Figure 2.1. The RPT homogenization method.

As seen in Figure 2.1, the fuel compact dimension is reduced, preserving the number of fuel particles and homogenized with a graphite matrix by a simple volume-weighting. The radius of the resultant fuel compact region was calculated such that k_∞ is equal to the reference solution, which was calculated with Monte Carlo. Reaction rates as well as k-inf are conserved with the RPT method.

In the MICROX code, developed by General Atomics (GA), shielded cross sections due to fuel kernels were calculated by Wälti[17] to account for the particle level heterogeneity. The collision probability method was utilized to calculate grain shielding factors for a two-region lattice cell. Cross sections, computed for the corresponding homogenized fuel compacts, were multiplied by the energy dependent grain shielding factors $\Gamma(E)$ to compute shielded cross sections. The grain shielding factor was defined as the ratio of the mean flux inside the fuel particles to the mean flux inside the moderator region (coatings + binder):

$$\Gamma(E)=\frac{\phi_0(E)}{\phi_1(E)} \tag{2.29}$$

where $\phi_0(E)$ and $\phi_1(E)$ are the spatially averaged fluxes at energy E in fuel kernels and moderator regions, respectively. The resulting equation was found to be as:

$$\Gamma(E)=\frac{1}{1+\frac{\tau_{x,0}}{1+\rho Q}W} \tag{2.30}$$

where $\tau_{x,0}=l_0\sum_{x,0}$ is the optical distance, $l_0=4V_0/S$ is the mean chord length, $\rho=l_0/l_1=V_0/V_1$ is the ratio of volumes , $Q=Q_0/Q_1$ is the ratio of the source densities, and the subscripts 0 and 1 correspond to fuel kernel and moderator (coatings + binding) regions, respectively. Also, W is defined as $W = 1 + \tilde{H}_0\left(\tau_{t,0}\right) + \tilde{H}_1\left(\tau_{t,1}\right)$ where $\tilde{H}_0$ and $\tilde{H}_1$ are numerically calculated for spherical kernels. In Eq. (2.30), ρ was found to be very small (~0.1) so the dependence of Eq. (2.30) on Q becomes very weak. Therefore, the grain shielding factor depends mainly on $\tau_{x,0}$: the product of the mean chord length and the unshielded removal cross section in the fuel kernels.

The GAROL[18] code, developed by General Atomics, analyzes the same problem with two regions. In addition, it accounts for resonance cross-shielding effects by solving the slowing down equations based on the collision probability method. All of these approximate methods that involve a two-region cell do not account for the effect of neighboring regions such as reflectors or control rods, and have difficulty dealing with resonance overlapping effects.

As an alternative approach, Monte Carlo codes have been used to perform neutronic analysis of gas cooled reactors, accounting for the double heterogeneity due to the VHTR particle fuel. The complex geometry modeling capability of Monte Carlo codes allows one to account for the double heterogeneity. Monte Carlo can also account for the resonance cross-shielding effect caused by the presence of multiple resonance materials provided a sufficient number of histories are utilized. In addition, the random distribution of the fuel kernels[19,20] can be handled by assuming the fuel kernels are placed in a regular lattice. This has been shown to be an acceptable model by several researchers. More accurate models allow the particles to vary randomly within a simple cubic lattice ("jiggling") but this effect has been shown to be small. In summary, Monte

Carlo codes have the unique advantage of calculating the shielded cross sections accurately as long as the continuous energy nuclear data is accurate.

Explicit modeling of fuel particles was performed by W. Ji[21,22] for the VHTR full core configurations in MCNP5, accounting for the double heterogeneity. A general method was developed to derive the closed form for the average Dancoff factors using the chord length sampling method in a stochastic environment. Average Dancoff factors were calculated for fuel compacts and fuel pebbles in both finite and infinite geometries[23-31].

In lattice physics codes, the second level heterogeneity due to fuel compacts or pebbles is handled by the well known shielding factor method that is used for LWR analysis. The proposed methodology is validated mostly with the CPM3[32] lattice physics code which is based on Carlvik's two-term rational approximation method[32,33]. This method is summarized next.

2.2.1 Resonance Treatment in CPM3

In CPM3, the 97 group cross section data was processed with the NJOY code system by averaging point-wise nuclear data (ENDF/B-VI) with an energy dependent weighting spectrum. In fact, the true spectrum varies within the reactor lattice due to different dimensions and compositions. The flux spectrum, caused by resonance reactions, is very sensitive to the relative concentrations of absorber and moderator materials as well as spatial heterogeneities in the lattice. Therefore the generic spectrum function is not adequate to yield acceptable cross sections for resonance materials. For this reason, microscopic cross sections, processed by NJOY, must be corrected to obtain problem-specific values for a particular lattice of interest.

In CPM3, a variation of the widely used shielding factor method is utilized. Pre-calculated, infinitely-dilute cross sections as well as shielding factors are tabulated in the nuclear data files (NDFs). This allows shielded multi-group cross sections to be calculated for a particular lattice of interest. Shielding factors, which indicate the degree of resonance self-shielding, are tabulated in NDFs as a function of temperature and background cross section:

$$f_i^r\left(T,\sigma_0\right)=\frac{\sigma_i^r\left(T,\sigma_0\right)}{\sigma^r\left(T,\infty\right)} \tag{2.31}$$

where $\sigma_i^r\left(T,\sigma_0\right)$ is the shielded cross section at the temperature and background cross section of interest and $\sigma^r\left(T_0,\infty\right)$ is the infinitely dilute unshielded cross section at reference temperature T$_0$ (=300K):

$$\sigma_i^r\left(T,\sigma_0\right)=\frac{\int\limits_E \sigma^r\left(E;T\right)\phi_i\left(E;T,\sigma_0\right)dE}{\int\limits_E \phi_i\left(E;T,\sigma_0\right)dE} \tag{2.32}$$

$$\sigma^r\left(T_0,\infty\right)=\frac{\int\limits_E \frac{\sigma^r\left(E;T_0\right)}{E}dE}{\Delta u} \tag{2.33}$$

In NJOY, the solution to the transport equation in an infinite, homogeneous medium is used for the flux spectrum that is needed to process the CPM3 multi-group cross sections. The homogeneous medium consists of a single resonance absorber and a non-absorbing moderator with a constant potential scattering cross section:

$$\left(N^r\sigma^r\left(E\right)+N^m\sigma_p^m\right)\phi\left(E\right)=N^rS^r\left(E\right)+N^mS^m\left(E\right) \tag{2.34}$$

where the superscripts r and m stand for resonance and moderator materials, respectively. The quantities N , σ , σ_p and S are number density, microscopic total cross section, microscopic potential scattering cross section and down-scattering source, respectively. The source term is the scattering source above the resonance energy and is defined as:

$$S\left(E\right)=\int_{E}^{E/\alpha}\frac{\sigma_s\phi\left(E^{'}\right)}{E^{'}\left(1-\alpha\right)}dE^{'} \tag{2.35}$$

The Intermediate Resonance (IR) approximation was used by introducing a factor λ^m such that the Narrow Resonance (NR) and Wide Resonance (WR) approximations and the infinitely dilute absorber case are all covered. For example, the parameter λ^m is 0 or 1 for NR and WR approximations, respectively. Therefore, Eq. (2.34) can be rewritten as:

$$\left(\sigma^r\left(E\right)+\sigma_0\right)\phi\left(E\right)=S^r\left(E\right)+\frac{\sigma_0\phi_\infty}{E} \tag{2.36}$$

The background cross section, σ_0, is defined as:

$$\sigma_0=\frac{\lambda^m\sigma_p^mN^m}{N^r} \tag{2.37}$$

When multiple moderators exist, σ_0 is expressed as:

$$\sigma_0=\frac{\sum_m\lambda^m\Sigma_p^m}{N^r} \tag{2.38}$$

The degree of the self-shielding is represented with the background cross section. Dilute concentrations have large values of σ_0 with no self-shielding, whereas high concentrations have low values of σ_0 with significant self-shielding.

In realistic reactor analysis, the homogeneous medium expressions must be related to the actual heterogeneous lattice configurations, using the "Equivalence Theorem" of lattice physics theory. The flux in absorber region F of a lattice is given by:

$$\Sigma_F(E)\phi_F(E)V_F = P_{F\to F}(E)N^F S_F(E)V_F + P_{F'\to F}(E)N^{F'} S_{F'}(E)V_{F'} + P_{M\to F}(E)N^M S_M(E)V_M \quad (2.39)$$

where Σ_F, S and N are macroscopic cross section for absorber body F, microscopic down-scatter source and number density, respectively. $P_{F\to F}$ is the probability that a neutron born in body F will have its first collision in F. $P_{F'\to F}$ is the probability that a neutron born within another absorber body F' will have its next collision in F. $P_{M\to F}$ is the probability that a neutron born within a non-absorber region of the lattice will have its next collision in absorber body F. Using the flat flux approximation ($S_{F'} \approx S_F$) and the reciprocity theorem relating $P_{F\to M}$ and $P_{M\to F}$ as well as the identity $P_{F\to F} + P_{F\to F'} + P_{F\to M} = 1$, Eq. (2.39) can be rewritten as:

$$\Sigma_F(E)\phi_F(E) = \left(1 - P_{F\to M}\right)N^F S_F(E) + \frac{P_{F\to M} N^M S_M(E)\Sigma_F}{\Sigma_M} \quad (2.40)$$

where $P_{F\to M}$ is given by the “Wigner rational approximation”:

$$P_{F\to M}(E) = \frac{\Sigma_e}{\Sigma_F(E) + \Sigma_e} \quad (2.41)$$

where Σ_e is the escape cross section. If Eq. (2.41) is inserted into Eq. (2.40) with the IR approximation and the flat flux assumption in the moderator region, the following Eq. (2.42) is obtained:

$$\left(\sigma^r(E) + \sigma_0\right)\phi(E) = S^r(E) + \frac{\sigma_0\phi_\infty}{E} \quad (2.42)$$

where the new background cross section is defined as:

$$\sigma_0 = \frac{\sum_{m\in F} \lambda^m \Sigma_p^m}{N^r} + \frac{\Sigma_e}{N^r} \tag{2.43}$$

As can be seen, Eqs. (2.36) and (2.42) are equivalent except the formulation for σ_0. The escape cross section in the Wigner approximation is defined as:

$$\Sigma_e = \Sigma_{e,0}\left(1-C\right) \tag{2.44}$$

where C is the Dancoff factor. It is defined as the probability that a neutron escaping the absorber body F will enter in another absorber body $F^{'}$. $\Sigma_{e,0} = 1/\overline{R}$ is the reciprocal of the average chord length through the absorber body and the average chord length is defined as $\overline{R} = 4V_F / A_F$.

Although the Wigner rational approximation is satisfactory at both the white and black limits, it is too low for gray absorbers. Therefore Carlvik[34] derived a more accurate expression for the escape probability:

$$1 - P_{F-M}\left(E\right) = x\left(\frac{\beta_1}{x+\alpha_1} + \frac{\beta_2}{x+\alpha_2}\right) \tag{2.45}$$

where α 's and β 's are constants, and $x = \overline{R}\Sigma_F\left(E\right)$. Eq. (2.45) reduces to the Wigner form if one rational term is used in the summation. The constants (α 's and β 's) provides more degrees of freedom to match physical conditions placed on the escape probability. For an *isolated* cylindrical absorber body, $P_{F\to M}$ is equal to the isolated rod escape probability, $P_{esc,F}$.

$$1 - P_{F-M}^{isolated} = 1 - P_{esc,F} = x\left(\frac{4}{x+2} + \frac{3}{x+3}\right) \tag{2.46}$$

In the case of a lattice of absorbers, $P_{F\rightarrow M}$ will not be equal to $P_{esc,F}$. The neutron may have its next collision in another absorber body in F'. Therefore, it was shown that $P_{F\rightarrow M}$ for a lattice can be approximated in terms of the isolated rod escape probability and the Dancoff factor:

$$P_{F\rightarrow M} = P_{esc,F}\left[\frac{1-C}{1-C\left(1-xP_{esc,F}\right)}\right] \tag{2.47}$$

The constants α and β can be obtained as a function of the Dancoff factor by using Eqs. (2.45)-(2.47). A non-uniform lattice configuration is accounted for by the Dancoff factor C:

$$\alpha_1 = \frac{\left(5+C\right)-\sqrt{C^2+34C+1}}{2} \tag{2.48}$$

$$\alpha_2 = \frac{\left(5+C\right)+\sqrt{C^2+34C+1}}{2} \tag{2.49}$$

In CPM3, a ray-tracing technique is used to compute the Dancoff factor for an arbitrary geometry. Dancoff factors are computed for different resonance absorber materials, including fuel materials, burnable absorber materials, and control rod materials.

The average flux in absorber body F can be given as the sum of two solutions:

$$\phi_F\left(E\right) = \beta\phi_1\left(E;T,\sigma_{0,1}\right)+\left(1-\beta\right)\phi_2\left(E;T,\sigma_{0,2}\right) \tag{2.50}$$

where $\beta_2 = 1-\beta_1$ and $\beta = \left(2C+4-\alpha_1\right)/\left(\alpha_2-\alpha_1\right)$. The solutions $\phi_n\left(E;T,\sigma_{0,n}\right)$ are two pseudo solutions to Eq. (2.42) in terms of the background cross section:

$$\sigma_0 \rightarrow \sigma_{0,n} = \frac{\sum\limits_{m\in F}\lambda^m\Sigma_p^m}{N^r}+\frac{\alpha_n\Sigma_{e,0}}{N^r} \tag{2.51}$$

Inserting the flux spectrum from Eq. (2.50) into Eq. (2.32):

$$\sigma_F^r = \frac{\beta \int_E \sigma^r(E;T)\phi_1(E;T,\sigma_{0,1})dE + (1-\beta)\int_E \sigma^r(E;T)\phi_2(E;T,\sigma_{0,2})dE}{\beta \int_E \phi_1(E;T,\sigma_{0,1})dE + (1-\beta)\int_E \phi_2(E;T,\sigma_{0,2})dE} \tag{2.52}$$

Eq. (2.52) can also be expressed in terms of group resonance integrals:

$$\sigma_F^r = \frac{\beta I(\sigma_{0,1},T) + (1-\beta) I(\sigma_{0,2},T)}{\beta \frac{\int_E \phi_1(E;T,\sigma_{0,1})dE}{\phi_\infty} + (1-\beta)\frac{\int_E \phi_2(E;T,\sigma_{0,2})dE}{\phi_\infty}} \tag{2.53}$$

Using the following relationship:

$$\frac{I(\sigma_{0,1})}{\sigma(\sigma_0)} = \frac{\int_E \phi_1(E;\sigma_0)dE}{\phi_\infty} \tag{2.54}$$

and performing some algebraic manipulation, the following expression can be obtained for the average multi-group cross section of absorber body F:

$$\sigma_F^r = \frac{\beta \frac{\sigma_{0,1}\sigma_{F,1}^r}{\sigma_{F,1}^r + \sigma_{0,1}} + (1-\beta)\frac{\sigma_{0,2}\sigma_{F,2}^r}{\sigma_{F,2}^r + \sigma_{0,2}}}{1 - \beta \frac{\sigma_{F,1}^r}{\sigma_{F,1}^r + \sigma_{0,1}} - (1-\beta)\frac{\sigma_{F,2}^r}{\sigma_{F,2}^r + \sigma_{0,2}}} \tag{2.55}$$

where $\sigma_{F,1}^r$ and $\sigma_{F,2}^r$ are shielded cross sections at the two background cross section values, and are defined in terms of the group infinitely dilute cross sections and shielding factors by:

$$\sigma_{F,1}^r = f_F^r(\sigma_{0,1},T)\sigma_F^r(\infty) \tag{2.56}$$

$$\sigma_{F,2}^r = f_F^r(\sigma_{0,2},T)\sigma_F^r(\infty) \tag{2.57}$$

Shielding factors are tabulated in the nuclear data file at specific values of temperature, T, and background cross sections, σ_0 . To obtain the desired shielding factor characteristics for the problem of interest, a two dimensional interpolation of these data in T and σ_0 is performed.

CHAPTER 3

ON-THE-FLY DOPPLER BROADENING for MONTE CARLO CODES

3.1 Theory

In nuclear data processing codes such as NJOY, the 0K cross sections for the majority of the resonance nuclides are processed with the Reich-Moore representation. However, this model does not have any temperature dependence to broaden the cross sections. Since our Doppler formulation avoids using the resonance parameters, any multi-level resonance representation with temperature dependence can be used. Adler-Adler[3] is the only multilevel representation that allows Doppler broadening of cross sections, which can be performed with the help of temperature dependent complex probability functions. Furthermore, the proposed regression model based on the Adler-Adler representation does not use resonance parameters and involves only the temperature dependent part of the multilevel model.

The combined regression model to perform on-the-fly Doppler broadening of the cross sections at energy grid points during Monte Carlo simulation is based on series expansions of the multi-level Adler-Adler representation with temperature dependence. The constants of the combined regression model were adjusted for the temperature range of 77K - 3200K to accommodate important fields of study as shown in Table 3.1.

Table 3.1. Temperature range and corresponding field of study.

Temperature Range (K)	**Field of Study**
77 - 293.6	Cold Neutron Physics
293.6 – 550	Benchmarking Calculations
550 – 1600	Reactor Operation
1600 – 3200	Accident Conditions

3.1.1 Development of the Regression Model

In the Adler-Adler multilevel resonance model, the total, fission and capture cross sections are represented by the following equations:

$$\sigma_{tot}(E,\xi_R)=\frac{4\pi}{k^2}\sin^2\Phi_0+\frac{\pi\sqrt{E}}{k^2}\Bigg\{\sum_R\frac{2}{\Gamma_{R,t}}\Big[\left(G_R\cos 2\Phi_0+H_R\sin 2\Phi_0\right)\psi(x,\xi_R)$$

$$+\left(H_R\cos 2\Phi_0-G_R\sin 2\Phi_0\right)\chi(x,\xi_R)\Big]$$

$$+A_1+\frac{A_2}{E}+\frac{A_3}{E^2}+\frac{A_4}{E^3}+B_1E+B_2E^2\Bigg\} \qquad (3.1)$$

$$\sigma_{cap,fis}(E,\xi_R)=\frac{\pi\sqrt{E}}{k^2}\Bigg\{\sum_R\frac{2}{\Gamma_{R,t}}\Big[\left(G_R\psi(x,\xi_R)+H_R\chi(x,\xi_R)\right)\Big]$$

$$+A_1+\frac{A_2}{E}+\frac{A_3}{E^2}+\frac{A_4}{E^3}+B_1E+B_2E^2\Bigg\} \qquad (3.2)$$

where $x=2(E_r-E_R)/\Gamma_T$, $\xi_R=\Gamma_T(A/4kE_RT)^{1/2}$, $k=(2.196771\times10^{-3})\sqrt{E}A/(A+1)$ is the neutron wave number, Φ_l is the phase shift, G_R is the symmetric total parameter, H_R is the asymmetric total parameter, A_i and B_i are coefficients of the total background correction. The terms G, H, A_i and B_i are defined as needed for the desired reactions. It should be noted that the resonance scattering cross sections are included in Eq. (3.1). Resonance parameters Γ_T and x as well as k, Φ_l, G, H, A$_i$ and B$_i$ can be held constant for a given neutron energy and target nuclide. The quantity ξ_R is the only temperature dependent resonance parameter in the ψ and χ functions and it will be analyzed in detail. In the Adler-Adler representation, the resonance overlapping effects in the keV range are taken into account automatically. In addition, the background cross sections are broadened. For these reasons, the Adler-Adler representation is more accurate than the psi-chi representation.

Since the resonance parameters Γ_T in ξ_R and x are constant for a given neutron energy and nuclide, the functions $\psi\left(x,\xi_R\right)$ and $\chi\left(x,\xi_R\right)$ in Eq. (3.1) and Eq. (3.2) can be written as $\psi(T)$ and $\chi(T)$, respectively. Consequently, they can be expressed in terms of the following series representations as a function of T:

$$\psi_R\left(T\right)=\sum_i a_{R,i}f_i\left(T\right) \tag{3.3}$$

$$\chi_R\left(T\right)=\sum_i b_{R,i}h_i\left(T\right) \tag{3.4}$$

where $a_{R,i}$ and $b_{R,i}$ are constants corresponding to the temperature dependent functions f_i and h_i. Inserting the ψ_R and χ_R functions into the Adler-Adler resonance representation, and performing several algebraic manipulations, the temperature dependent cross section of any type can be represented as:

$$\sigma_R^x\left(T\right)=A_R+\sum_{R'}\left[B_{R'}\psi\left(T\right)+C_{R'}\chi\left(T\right)\right] \tag{3.5}$$

$$\sigma_R^x(T) = A_R + \sum_{R'} \left[B_{R'} \sum_i a_{R',i} f_i(T) + C_{R'} \sum_i b_{R',i} h_i(T) \right] \tag{3.6}$$

$$\sigma_R^x(T) = A_R + \sum_i f_i(T) \sum_{R'} a'_{R',i} + \sum_i h_i(T) \sum_{R'} b'_{R',i} \tag{3.7}$$

$$\sigma_R^x(T) = A_R + \sum_i f_i(T) a''_i + \sum_i h_i(T) b''_i \tag{3.8}$$

The constants in the above equations are specific to the reaction type for a given neutron energy and nuclide. Once the form of the temperature dependence of the functions f_i and h_i is found, the constants in the above regression models can be determined by applying the actual Doppler broadened cross sections (i.e., Cullen's model) over a given range of temperature.

For a given nuclide, cross sections at different resonance energy points show different temperature dependence. Therefore, the temperature dependence of the cross sections must be investigated by dividing the resonance energy range into several sub-regions. In particular, we have partitioned a typical resonance cross section into three regions: (1) near the peak of the resonance, (2) mid-resonance, and (3) the wings of the resonance. These energy regions are depicted for a typical resonance in Figure 3.1.

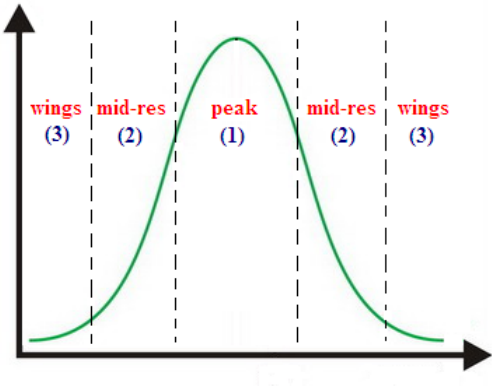

Figure 3.1. Energy regions for a typical resonance.

3.1.2 Broadened Cross Sections near the Peak of a Resonance

In this region, Doppler-broadened cross sections decrease with increasing material temperature. The spacing of energy grid points is chosen to satisfy a specified fractional tolerance criterion. The fractional tolerance is defined as the relative difference in cross sections between the values of actual and linearly interpolated cross sections at mid-points of successive energy grid intervals. (A more detailed explanation is given in Section 3.2.) Figure 3.2 shows the behavior of the Doppler-broadened cross sections as a function of material temperature for U238 around the resonance peak energy at 6.674eV. The plots in Figure 3.2 were produced by the auxiliary Doppler code (ADC) which will be explained in detail in Section 3.3.

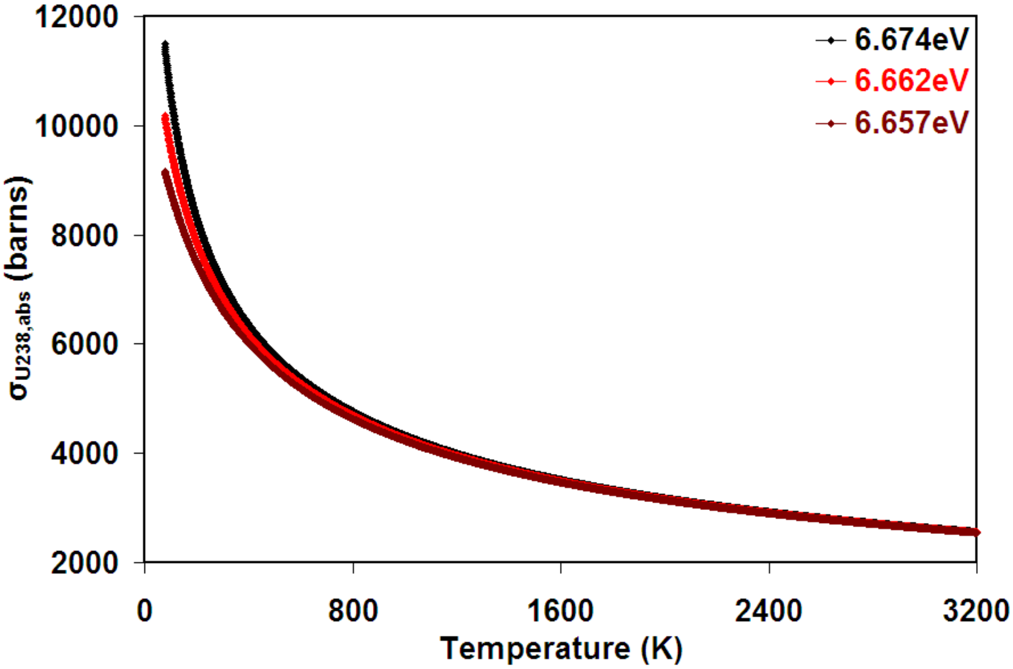

Figure 3.2. σ_a^{U238} as a function of temperature near the peak of a resonance.

Near the peak of the resonance, $E_r \cong E_R$ therefore $x = 2\left(E_r - E_R\right)/\Gamma_T \approx 0$ and a Taylor series expansion of ψ_R and χ_R in the variable z (which is defined below) is appropriate when x is small. The variable x can be interpreted as the distance from the peak of a resonance for a given neutron energy and nuclide. The temperature dependent terms in the resultant expansion can then be calculated using the actual broadened cross sections. This has been found to yield acceptable results for the least number of terms in the expansion. The resultant expansions may be expressed as follows:

$$\psi_R(z) = \frac{\xi_R}{2\sqrt{\pi}} \operatorname{Re}\left\{\exp\left(z^2\right) erfc(-z)\right\} \tag{3.9}$$

$$\chi_R(z) = \frac{\xi_R}{2\sqrt{\pi}} \operatorname{Im}\left\{\exp\left(z^2\right) erfc(-z)\right\} \tag{3.10}$$

where $z = i(x+i)\xi_R/2$. Taylor series expansions for the exponential and complementary error function are given by[35]:

$$\exp\left(z^2\right) = \sum_{n=0}^{\infty} \frac{z^{2n}}{n!} \tag{3.11}$$

$$erfc(-z) = 1 + \frac{2}{\sqrt{\pi}} \sum_{n=0}^{\infty} \frac{(-1)^n z^{2n+1}}{n!(2n+1)} \tag{3.12}$$

Since $\xi_R = \Gamma_T (A/4kE_R T)^{1/2}$, z can be written as $z = (b_R + c_R i)/\sqrt{T}$ for a given neutron energy and nuclide where b_R and c_R are constants. Therefore, we have

$$\psi_R(T) = \frac{a_R}{\sqrt{T}} \operatorname{Re}\left\{\exp\left[\left(\frac{b_R + c_R i}{\sqrt{T}}\right)^2\right] erfc\left(-\frac{b_R + c_R i}{\sqrt{T}}\right)\right\} = \sum_{i=1}^{\infty} \frac{d_{R,i}}{T^{i/2}} \tag{3.13}$$

$$\chi_R(T) = \frac{a_R}{\sqrt{T}} \operatorname{Im}\left\{\exp\left[\left(\frac{b_R + c_R i}{\sqrt{T}}\right)^2\right] erfc\left(-\frac{b_R + c_R i}{\sqrt{T}}\right)\right\} = \sum_{i=1}^{\infty} \frac{e_{R,i}}{T^{i/2}} \tag{3.14}$$

where d_R and e_R are constants. Therefore, $f_i(T) = d_{R,i}/T^{i/2}$ and $h_i(T) = e_{R,i}/T^{i/2}$. Inserting $f_i(T)$ and $h_i(T)$ into Eq. (3.8):

$$\sigma^{\sim peak}_{tot,cap,fis}\left(T\right)=\sum_{i=0}^{\infty}\frac{k_{R,i}}{T^{i/2}} \tag{3.15}$$

where k_R is constant.

3.1.3 Broadened Cross Sections near the Resonance Wings

In this region, Doppler-broadened cross sections increase with increasing material temperature. Energy grid points are widely spaced due to the slowly varying behavior of the cross sections as a function of energy. Figure 3.3 presents the behavior of the Doppler-broadened cross sections as a function of material temperature near the U-238 resonance wings at 6.674 eV. The plots in Figure 3.3 were produced by ADC.

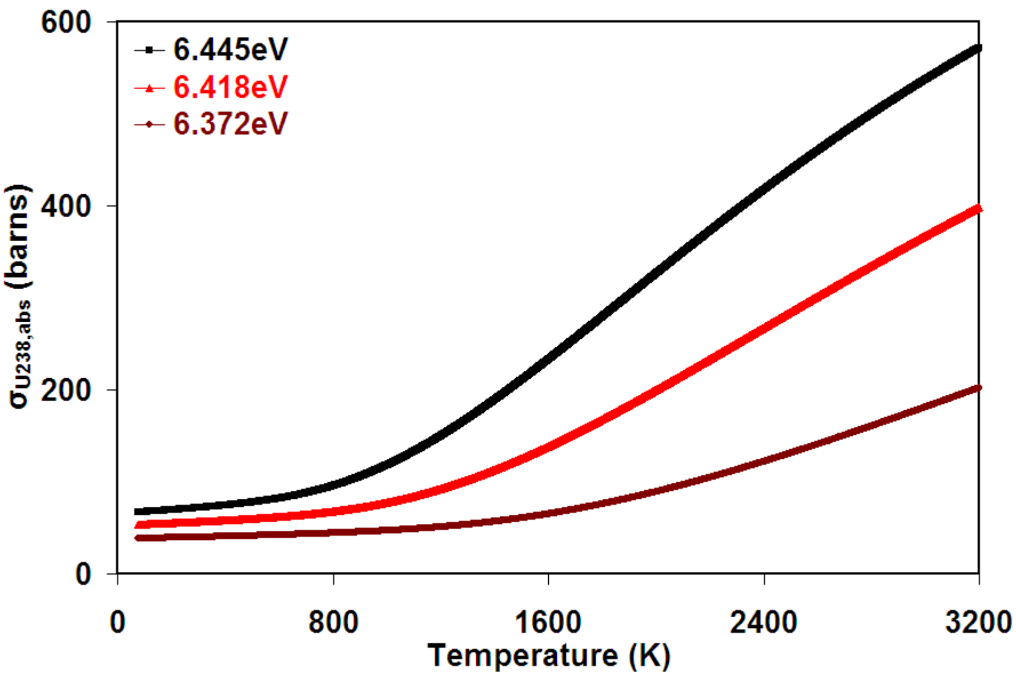

Figure 3.3. σ_a^{U238} as a function of temperature near the resonance wings.

Near the wings of the resonance, $2\left|E_r-E_R\right|>\Gamma_T$ therefore $x=2\left(E_r-E_R\right)/\Gamma_T>>1$ and an asymptotic series expansion of ψ_R and χ_R in z is appropriate when x is large, since a Taylor series expansion will converge very slowly, requiring many terms to obtain the same accuracy. The temperature dependent terms in the resultant expansion can then be calculated using the actual broadened cross sections as done earlier for energies near the peak of the resonance. This has been found to yield acceptable results for the least number of terms in the expansion. It should be noted that asymptotic expansions of $\exp\left(z^2\right)erfc\left(-z\right)$ are not convergent. This behavior is characteristic of the asymptotic expansion. However, only the first several terms are enough to obtain reasonable accuracy[35]. The resultant expansions may be expressed as follows:

$$erfc\left(-z\right)=-\frac{e^{-z^2}}{z\sqrt{\pi}}\sum_{n=0}^{\infty}\frac{(-1)^n(2n)!}{n!(2z)^{2n}} \tag{3.16}$$

This equation can be rewritten as:

$$\exp\left(z^2\right)erfc\left(-z\right)=-\frac{1}{z\sqrt{\pi}}\sum_{n=0}^{\infty}\frac{(-1)^n(2n)!}{n!(2z)^{2n}} \tag{3.17}$$

Since $\xi_R=\Gamma_T\left(A/4kE_RT\right)^{1/2}$, z can be written as $z=\left(b_R+c_Ri\right)/\sqrt{T}$ for a given neutron energy and nuclide where b_R and c_R are constants. Therefore, we have

$$\psi_R\left(T\right)=\frac{a_R}{\sqrt{T}}\mathrm{Re}\left\{\exp\left[\left(\frac{b_R+c_Ri}{\sqrt{T}}\right)^2\right]erfc\left(-\frac{b_R+c_Ri}{\sqrt{T}}\right)\right\}=\sum_{i=1}^{\infty}d_{R,i}T^i \tag{3.18}$$

$$\chi_R\left(T\right)=\frac{a_R}{\sqrt{T}}\mathrm{Im}\left\{\exp\left[\left(\frac{b_R+c_Ri}{\sqrt{T}}\right)^2\right]erfc\left(-\frac{b_R+c_Ri}{\sqrt{T}}\right)\right\}=\sum_{i=1}^{\infty}e_{R,i}T^i \tag{3.19}$$

where d_R and e_R are constants. Therefore, $f_i\left(T\right)=d_{R,i}T^i$ and $h_i\left(T\right)=e_{R,i}T^i$. Inserting $f_i\left(T\right)$ and $h_i\left(T\right)$ into Eq. (3.8):

$$\sigma_{tot,cap,fis}^{\sim wings}(T) = \sum_{i=0}^{\infty} l_{R,i} T^i \qquad (3.20)$$

where l_R is constant.

3.1.4 Broadened Cross Sections near the Mid-Resonance

In this region, Doppler-broadened cross sections first increase and then decrease with increasing material temperature. Figure 3.4 presents the behavior of the Doppler-broadened cross sections as a function of material temperature for the mid-resonance region of the U-238 resonance at 6.674 eV. The plots in Figure 3.4 were produced by ADC.

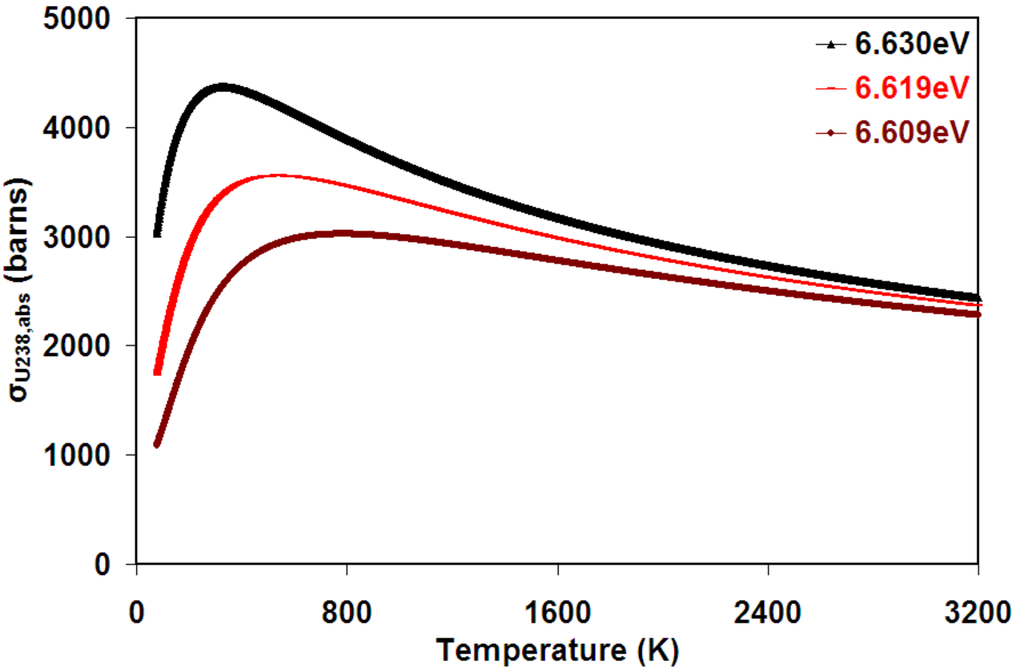

Figure 3.4. σ_a^{U238} as a function of temperature near the mid-resonance.

In this energy range, one obtains moderate values of $x = 2(E_r - E_R)/\Gamma_T \approx 1$ therefore z is also of moderate size, and there is no clear physical basis to choose a particular series representation in z that yields a functional expression in terms of T.

Therefore a computational investigation was performed for representative energy grid points in this region to identify the best polynomial representation among several models. The form of temperature dependence in each polynomial model is based on the paper by Trumbull[12] which was summarized in Section 2.1.4. Therefore linear, square-root and logarithmic models in temperature were analyzed. To be consistent with the final form of the combined regression model which can be found in the next Section 3.1.5, 12th order (13 terms) polynomial models were chosen. The SSE (sum of squares error) and RMSE (root mean square error) error terms were monitored to find the best fit for the range of resonance cross sections in this region. The results are presented in Table 3.2.

Table 3.2. Comparison of Different 12th–Order Regression Models.

	6.630eV		**6.619eV**		**6.609eV**	
	SSE	**RMSE**	**SSE**	**RMSE**	**SSE**	**RMSE**
$\sum_{n=0}^{12} m_n (T)^n$	1.23E+04	1.99E+00	8.98E+03	1.70E+00	1.72E+04	2.35E+00
$\sum_{n=0}^{12} m_n (T)^{n/2}$	2.94E+00	3.07E-02	2.66E+01	9.25E-02	2.68E+01	9.29E-02
$\sum_{n=0}^{12} m_n (\ln T)^n$	3.13E+08	3.17E+02	4.12E+08	3.64E+02	4.36E+08	3.75E+02
$\sum_{n=0}^{12} m_n (\ln T)^{n/2}$	2.94E+08	3.07E+02	4.07E+08	3.62E+02	3.70E+08	3.45E+02

As can be seen in Table 3.2, the second polynomial representation of the U-238 absorption cross section as a function of $\sqrt{T}$ provides the best accuracy among the others for a fixed number of terms.

$$\sigma_{tot,cap,fis}^{\sim mid-res}(T) \cong \sum_{i=0}^{\infty} m_i T^{i/2} \tag{3.21}$$

The physical basis of this observation can be explained as follows: It is already known that, as temperature increases, the width of a given resonance increases with $\sqrt{T}$ and this is observed near the mid-resonance region where the resonance width is defined.

3.1.5 Combined Doppler Broadening Model

Cross sections for the three energy regions (near the peak of the resonance, mid-resonance, and resonance wings) for any resonance based on the Adler-Adler multi-level representation was found in the previous sections. The mid-resonance representation in Eq. (3.21) already involves the temperature dependent terms found for the wings in Eq. (3.20). Therefore, the mid-resonance and resonance wing models can be combined into one model:

$$\sigma_{tot,cap,fis}^{\sim mid-res,wings}\left(T\right)=\sum_{i=0}^{\infty}n_i T^{i/2} \tag{3.22}$$

So cross sections as a function of temperature can be summarized by the following two series representations for the three regions:

$$\sigma_{tot,cap,fis}^{\sim peak}\left(T\right)=\sum_{i=0}^{\infty}\frac{k_{R,i}}{T^{i/2}},\quad \sigma_{tot,cap,fis}^{\sim mid-res,wings}\left(T\right)=\sum_{i=0}^{\infty}n_i T^{i/2} \tag{3.23}$$

A final numerical study was performed to find a single regression model by combining two different series solutions in Eq. (3.23) so that cross sections over all three energy ranges can be calculated accurately with a modest computing cost. The most challenging resonance absorber, U-238, was chosen for the numerical investigation. A numerical investigation was performed by combining different numbers of terms from each representation in Eq. (3.23), at the same time keeping the total number of terms constant in each outer iteration (outer iteration=total number of terms=10, .. 15) and providing excellent accuracy over all regions. Maximum relative error in absorption cross section over the entire energy interval was monitored to decide the optimum functional representation of cross sections as a function of temperature. The following equation was found as a result of the numerical investigation described above:

$$\sigma_{tot,cap,fis}\left(T\right) \cong \sum_{i=1}^{6} \frac{a_i}{T^{i/2}} + \sum_{i=1}^{6} b_i T^{i/2} + c \tag{3.24}$$

where a_i, b_i, c are the constants of the above regression model and depend on the specific nuclide and type of reaction. The combined regression model was successfully tested against several other resonance absorbers including plutonium isotopes and fission products, indicating that the U-238 cross section was a good choice for fitting the regression model.

The combined regression model requires pre-generated temperature dependent cross sections on an energy grid at every 1K to determine the constants a_i, b_i, c in Eq. (3.24) in order to satisfy a given fractional tolerance (FT), as discussed in the next section. However, the energy grid structure at different temperatures for a given nuclide needed to satisfy the FT will be different, resulting in disparate energy grids for the same nuclide. This will not allow a consistent regression in temperature for all energies, so a "union" energy grid is constructed for the temperature range of interest and for each nuclide, allowing the combined regression model to determine the constants over the temperature range of interest.

3.2 Construction of the Union Energy Grid

Continuous energy Monte Carlo codes require nuclear cross sections on a sufficiently fine energy grid structure to allow linear interpolation of cross sections within a given tolerance. The input parameter used by the nuclear data processing (NDP) codes to construct the energy grid is called the Fractional Tolerance (FT). It is defined as the relative difference in cross sections between the values of actual and linearly interpolated cross sections at mid-points between successive energy grid points.

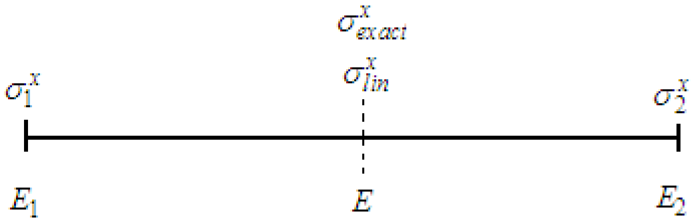

Figure 3.5. FT calculation for a given energy grid interval.

Figure 3.5 depicts a typical FT calculation where $E=\left(E_1+E_2\right)/2$ is the mid-point energy and $\sigma_{lin}^{x}=\left(\sigma_1^x+\sigma_2^x\right)/2$ is the corresponding linearly interpolated cross section.

In order to construct the 0K energy grid, the corresponding cross section data σ_1^x, σ_2^x, and σ_{exact}^{x} are calculated based on resonance parameters by using different multi-level representations (e.g. Multilevel Breit-Wigner, Reich-Moore, Adler-Adler, etc…) in NJOY. Then the following check is performed if an additional energy grid point is required to accurately represent the cross sections between energy grid points within a given FT:

$$\frac{\left|\sigma_{exact}^{x}-\sigma_{lin}^{x}\right|}{\sigma_{exact}^{x}} > FT \tag{3.25}$$

If Eq. (3.25) is satisfied (i.e., the FT criterion is not satisfied), a new energy grid point E is added halfway between E_1 and E_2. This process is performed in a cyclic fashion until convergence is reached over the entire energy grid for a given nuclide.

When Doppler broadened cross sections are needed, the exact Doppler broadening Eq. (2.1) is used to calculate cross sections $\sigma^{x}_{exact}(T)$ at the elevated temperature T based on the previously generated 0K nuclear data. An investigation was carried out to determine the number of energy grid points needed by NJOY at different elevated temperatures as a function of FT, using 0K data as the base set of cross sections. Results are given in Table 3.3 for U-238.

Table 3.3. Number of energy grid points as a function of temperature and FT for U238.

	Fractional Tolerance							
	0.1%	*0.3%*	*0.5%*	*1.0%*	*2.0%*	*3.0%*	*4.0%*	*5.0%*
T (K)	**Number of Energy Grid Points**							
0	193131	122935	100646	76856	57347	49659	44955	41676
77	103600	70240	59900	50049	43716	41408	40250	39514
293.6	85247	60192	52352	44810	39965	38089	37104	36494
500	77676	55786	49097	42506	38188	36509	35565	35006
1000	67437	50226	44773	39625	35957	34593	33810	33282
1500	62302	47227	42557	38000	34881	33616	32956	32490
2000	58735	45153	41098	36957	34109	32999	32384	31918
2500	56248	43774	39933	36177	33586	32543	31948	31560
3000	54282	42707	39051	35557	33208	32192	31661	31314

Figure 3.6 shows the energy grid structure for two temperature points of the U-238 resonance at 20.871eV. Two extreme temperature points were chosen to show the variation of energy grid points clearly in different portions of a given resonance. As shown in Figure 3.6, when the temperature increases, the number of the energy grid points to satisfy a given FT decreases near the peak of a resonance as it smooths out, resulting in a coarser energy grid structure. On the other hand, as shown in Figure 3.6,

when the temperature increases, more energy grid points are required for the middle and wings of a resonance to satisfy the same FT, yielding a finer energy grid structure. Although the overall effect is usually to decrease the final number of energy grid points with increasing temperature, the structure of the energy grid to satisfy a given FT depends on temperature, nuclide, and energy range within the resonance, Therefore, as explained above, the construction of a union energy grid is required in order to use the combined regression model over the entire temperature range of interest for a given nuclide.

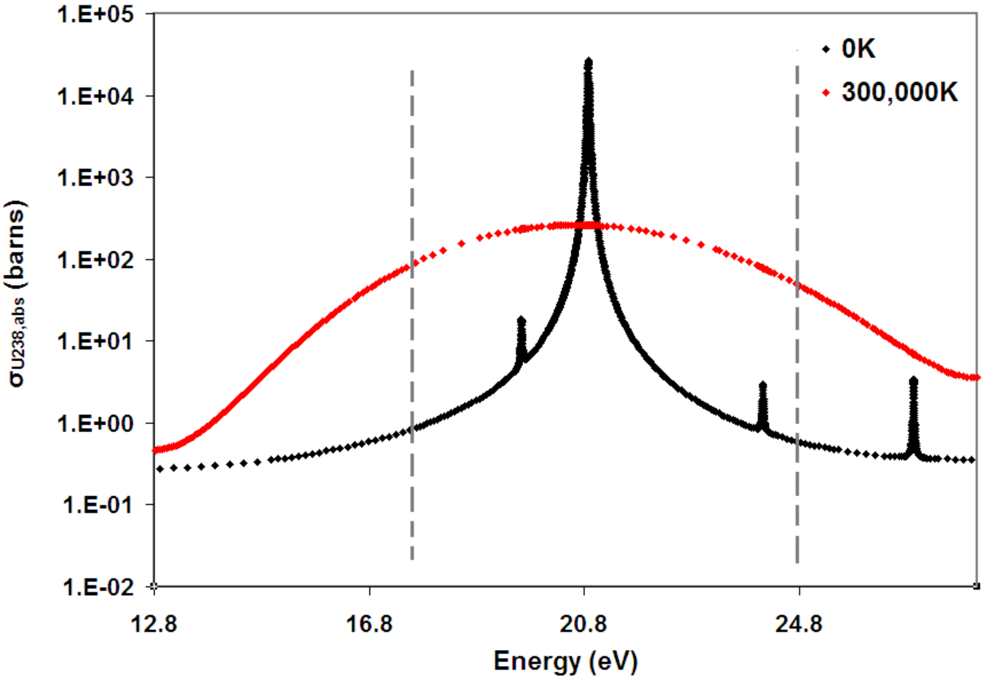

Figure 3.6. Evolution of energy grid structure with temperature.

Therefore, a union energy grid was developed to allow one to calculate the constants of the combined regression model that satisfy a single given FT for the temperature range of interest [77K-3200K] for U-238. For simplicity, only the absorption cross section was chosen to illustrate the methodology. In reality, this methodology should include all three cross sections (σ_{cap}, σ_{fis}, and σ_{scat}) at the same time to test the FT at every T between 77K and 3200K to determine the final union grid.

The algorithm depicted in Figure 3.7 was implemented to add new points to the 77K energy grid to find a union energy grid for the entire temperature range of interest [77K-3200K].

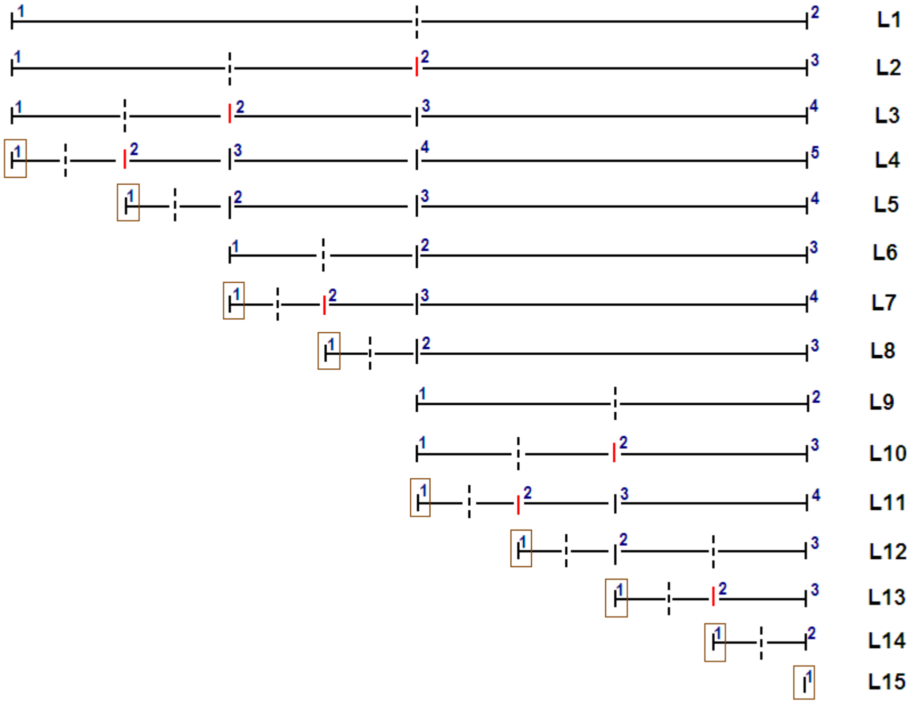

Figure 3.7. Algorithm to construct the union energy grid.

In Figure 3.7, new energy grid points were continuously added to the original grid at 77K until the convergence in FT was reached at every energy interval for the temperature range of interest. In line 1, new cross sections were calculated by Eq. (2.1) at the middle of the successive energy grid points at every T between 77K and 3200K. They are then compared with the linearly interpolated cross section at the same energy grid point for the same temperature range of interest [77K-3200K]. In this case, the cross sections, at least for one of the temperature points, were not within the given FT, so a new energy point was added to the original grid, marked with a red line, as can be seen in line 2. The energy grid vector is updated automatically when a new point is added. In lines 2 and 3, the same methodology was applied but the convergence in FT, at least for one of the temperature points, was not reached so additional energy points were added. In line 4, it was found that the first energy interval converged therefore the energy grid 1, marked with brown box, was recorded in a separate vector and deleted from the energy grid vector. The iteration is performed until one energy grid point is left in the energy grid vector. The energy grid points, recorded in the separate vector, represent the final union energy grid for the given nuclide and temperature range of interest.

However, the union energy grid, described above, cannot be generated by cross section processing codes such as NJOY. Therefore, a c++ code, named Auxiliary Doppler Code (ADC), was implemented to determine the union energy grid and the corresponding cross sections for a temperature range of interest and a given nuclide. The ADC code was tested against NJOY at different reference temperature points for several resonance absorbers and it was found that ADC is exactly (within 8 significant figures) consistent with NJOY. The ADC code is required to preprocess the 0K cross section data for the temperature range of interest to find a union energy grid and the corresponding cross sections for a given nuclide. The ADC code will be explained in detail in the next section.

It should be noted that the number of energy grid points at a given temperature can become very large for some nuclides that have narrow, high-energy resonances. This problem was solved in NJOY as follows. If the contribution to the resonance integral from any one interval is small, the interval will be declared converged. This residual resonance integral error was set at 0.001 barns in NJOY for a FT of 0.1%. Since important resonance integrals vary from a few barns to a few hundred barns, this yields an error in the resonance integral of less than 0.1%. This methodology was also implemented in ADC to end up with a reasonable file size.

Table 3.4. Union energy grid of σ_{abs}^{U238} for 77K-3200K.

	# of Union Grid Points (FT = 0.1%)		
ΔT (K)	**Res. Int. Err. = 0.001 b**	**Res. Int. Err. = 0.0001 b**	**Res. Int. Err. = 0**
100	109,134	148,366	360,129
50	109,154	148,614	363,513
25	109,159	148,692	364,525

The original energy grid of σ_{abs}^{U238} has 103,600 points at 77K to satisfy an FT of 0.1%. In Table 3.4, when NJOY's default resonance integral error (0.001b for an FT of 0.1%) is used, the increase in the number of grid points was found to be around 5500. A further decrease of resonance integral error to 0.0001b leads to a higher number of energy grid points. If the resonance integral error check is not performed (see the last column in Table 3.4), the number of union energy grid points can be several times larger than at 77K.

3.3 Auxiliary Doppler Code (ADC)

3.3.1 Discretization of Doppler Broadening Equation

According to Cullen[4], Eq. (2.1) can be simplified for $\sigma(y, T_2)$ as follows:

$$\sigma(y,T_2) = \sigma^*(y,T_2) - \sigma^*(-y,T_2) \tag{3.26}$$

$$\sigma^*(y,T_2)=\frac{1}{y^2}\frac{1}{\sqrt{\pi}}\int_0^\infty\left[x^2\sigma(x,T_1)\right]\exp\left[-(x-y)^2\right]dx \tag{3.27}$$

Zero temperature cross sections were tabulated as a function of energy with linear-linear interpolation. So $\sigma(y,T_1)$ can be written in a discretized form as follows;

$$\sigma_i(x,T_1)=\sigma_i(T_1)+s_i\left(x^2-x_i^2\right) \tag{3.28}$$

where s_i is defined as:

$$s_i=\frac{\sigma_{i+1}(T_1)-\sigma_i(T_1)}{x_{i+1}^2-x_i^2} \tag{3.29}$$

Inserting Eq. (3.28) into Eq. (3.27) and replacing the integral with a sum and letting z=x-y, we have:

$$\sigma^*(y,T_2)=\frac{1}{y^2}\frac{1}{\sqrt{\pi}}\sum_{i=0}^{N}\left\{\left[\sigma_i(T_1)-s_ix_i^2\right]\int_{x_i-y}^{x_{i+1}-y}(z+y)^2\exp\left[-z^2\right]dz+s_i\int_{x_i-y}^{x_{i+1}-y}(z+y)^4\exp\left[-z^2\right]dz\right\} \tag{3.30}$$

Eq. (3.30) can be rewritten in the following form;

$$\sigma^*(y,T_2)=\sum_{i=0}^{N}\left\{\left[\sigma_i(T_1)-s_ix_i^2\right]A_i+s_iB_i\right\} \tag{3.31}$$

where A_i and B_i are defined as follows;

$$A_i=\frac{1}{y^2}\frac{1}{\sqrt{\pi}}\int_{x_i-y}^{x_{i+1}-y}(z+y)^2\exp\left[-z^2\right]dz \tag{3.32}$$

$$B_i=\frac{1}{y^2}\frac{1}{\sqrt{\pi}}\int_{x_i-y}^{x_{i+1}-y}(z+y)^4\exp\left[-z^2\right]dz \tag{3.33}$$

Letting

$$H_n(x_i-y,x_{i+1}-y)=H_n(a,b)=\frac{1}{\sqrt{\pi}}\int_a^b z^n\exp\left(-z^2\right)dz \tag{3.34}$$

A_i and B_i are rewritten as;

$$A_i = \frac{1}{y^2}\left[H_2(a,b) + 2yH_1(a,b) + y^2H_0(a,b)\right] \tag{3.35}$$

$$B_i = \frac{1}{y^2}\left[H_4(a,b) + 4yH_3(a,b) + 6y^2H_2(a,b) + 4y^3H_1(a,b) + y^4H_0(a,b)\right] \tag{3.36}$$

where $H_n(a,b) = F_n(a) - F_n(b)$ are calculated based on the F functions defined as follows:

$$F_n(a) = \frac{1}{\sqrt{\pi}}\int_a^{\infty} z^n \exp\left(-z^2\right)dz \tag{3.37}$$

$$F_0(a) = \frac{1}{2}erfc(a) \tag{3.38}$$

$$F_1(a) = \frac{1}{2\sqrt{\pi}}\exp(a) \tag{3.39}$$

The F functions obey the following recurrence relation:

$$F_n(a) = \frac{n-1}{2}F_{n-2}(a) + a^{n-1}F_1(a) \tag{3.40}$$

Extra attention must be paid when $(a-b)$ gets small because $H_n(a,b)$ loses its significance. Therefore $H_n(a,b)$ must be calculated with a Taylor series expansion:

$$H_n(a,b) = \frac{b-a}{1!}G_n^{'}(a) + \ldots + \frac{(b-a)^m}{m!}G_n^m(a) + \ldots \tag{3.41}$$

$$G_n^m(x) = \frac{d^{m-1}}{dx^{m-1}}[x^n \exp(-x^2)] = \exp(-x^2)P_n^m(x) \tag{3.42}$$

$$P_n^m = \frac{d}{dx}P_n^{m-1}(x) - 2xP_n^{m-1}(x) \tag{3.43}$$

$$P_n^1 = x^n \tag{3.44}$$

Since the error function calculation was expensive, these relations were computed up to only 6 accurate decimal digits when the original broadening module was implemented in NJOY. In our ADC code, error functions are computed with 16 digit accuracy, eliminating the need for the Taylor series expansion when $(a-b)$ gets small. This makes ADC several times faster than the BROADR module of NJOY, while preserving the same accuracy.

For $\sigma^*(y,T_2)$, the exponential function in Eq. (3.27) limits the significant part of the integral to the range:

$$V-\frac{4}{\beta}<V_r<V-\frac{4}{\beta} \;\Leftrightarrow\; y-4<x<y+4 \;\Leftrightarrow\; -4<z<4$$

The limits of the summation in Eq. (3.31) are shown in Figure 3.8 for $\sigma^*(y,T_2)$. Cross sections between y-4 and y+4 are utilized in Eq. (3.31) to Doppler broaden the cross section y located at the grid point x_i as shown in Figure 3.8.

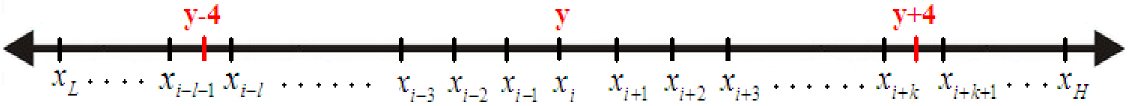

Figure 3.8. Integral limits for $\sigma^*(y,T_2)$.

Similarly, for $\sigma^*(-y,T_2)$, the exponential function in Eq. (3.27) limits the significant part of the integral to the range:

$$0\le V_r<\frac{4}{\beta} \quad\Leftrightarrow\quad 0\le x<4$$

The limits of the summation in Eq. (3.31) are shown in Figure 3.8 for $\sigma^*(-y,T_2)$. Cross sections between 0 and 4 are utilized in Eq. (3.31) to Doppler broaden the cross section y located at the grid point x_i as shown in Figure 3.9.

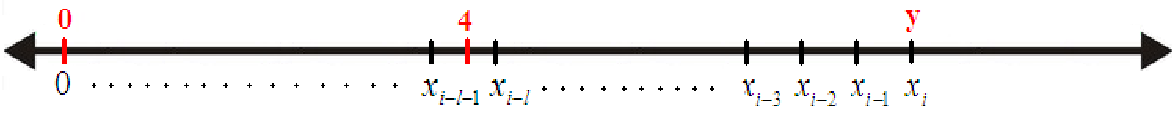

Figure 3.9. Integral limits for $\sigma^*(-y,T_2)$.

where x and y are velocity like terms which were defined in Eq. (2.2) and Eq. (2.3), respectively. Doppler broadening of the cross section located at the grid point xi requires

One needs to pay attention when broadening the cross sections close to the end points of the energy grid. As shown in the following Figure 3.10, cross sections may not be known in the range before y-4 or before y+4 and will need to be approximated in order to be integrated.

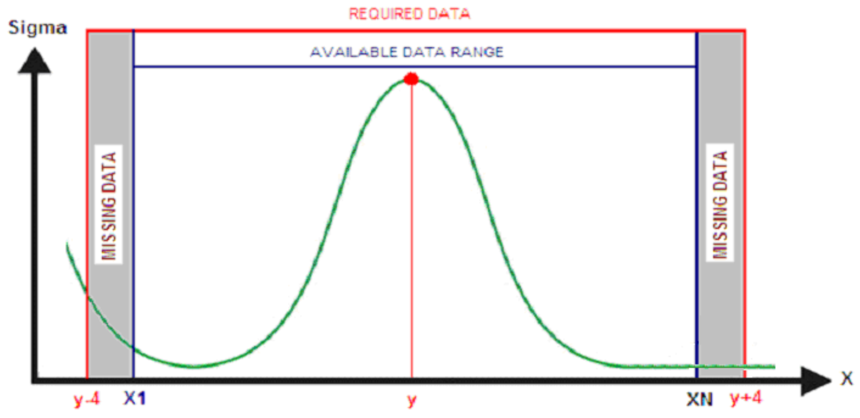

Figure 3.10. Low and high energy approximations.

3.3.1.1 Low Energy Approximation

When the tabulated low energy cross sections end before reaching the lower bound y-4, the cross sections are approximated as $1/v$ up to zero to broaden them at y. This is consistent with the theoretical low energy dependence of most nuclear cross sections:

$$\sigma\left(x,T_1\right)=\frac{C}{x} \tag{3.45}$$

where $C = x_1\sigma(x_1,T_1)$. Inserting Eq. (3.45) into Eq. (3.27) and letting z=x-y:

$$\sigma^*\left(y,T_2\right)=\frac{1}{y^2}\frac{1}{\sqrt{\pi}}\int_{-y}^{x_1-y}\left[\left(z+y\right)C\right]\exp\left[-z^2\right]dz \tag{3.46}$$

$$\sigma^*\left(y,T_2\right)=\frac{C}{y^2}\left[H_1\left(-y,x_1-y\right)+yH_1\left(-y,x_1-y\right)\right] \tag{3.47}$$

3.3.1.2 High Energy Approximation:

When the high energy cross sections are not known before reaching the upper bound y+4, the cross sections are assumed to be constant beyond the last data point:

$$\sigma\left(x_{N+1},T_1\right)=C \tag{3.48}$$

Inserting Eq. (3.48) into Eq. (3.27) and letting z=x-y:

$$\sigma^*\left(y,T_2\right)=\frac{1}{y^2}\frac{1}{\sqrt{\pi}}\int_{x_N-y}^{\infty}\left[\left(z+y\right)^2C\right]\exp\left[-z^2\right]dz \tag{3.49}$$

$$\sigma^*\left(y,T_2\right)=\frac{C}{y^2}\left[F_2\left(x_N-y\right)+2yF_1\left(x_N-y\right)+y^2F_3\left(x_N-y\right)\right] \tag{3.50}$$

3.3.2 Comparison of ADC with NJOY99

Absorption cross sections were Doppler broadened with ADC and results were compared against NJOY at different material temperatures for U-238, Pu-239, Xe-135 and Sm-149 at the peak of the most important resonance energy grid points. Results are presented in Table 3.5.

Table 3.5. Comparison of σ_a between NJOY and ADC.

	U-238 (6.674eV)		**U-238 (20.871eV)**		**U-238 (36.682eV)**	
Temp (K)	**NJOY**	**ADC**	**NJOY**	**ADC**	**NJOY**	**ADC**
77	1.148987E+04	1.148987e+04	1.152135E+04	1.152135e+04	8.737500E+03	8.737498e+03
293.6	7.185715E+03	7.185712e+03	6.926944E+03	6.926941e+03	5.458244E+03	5.458242e+03
1100	4.152143E+03	4.152141e+03	3.907597E+03	3.907596e+03	3.151735E+03	3.151734e+03
1300	3.857621E+03	3.857619e+03	3.622438E+03	3.622436e+03	2.927983E+03	2.927982e+03
	PU-239 (0.2945eV)		**XE-135 (0.0253eV)**		**SM-149 (0.0959eV)**	
Temp (K)	**NJOY**	**ADC**	**NJOY**	**ADC**	**NJOY**	**ADC**
77	2.234414E+03	2.234414e+03	2.640631E+06	2.640631e+06	1.273629E+05	1.273629e+05
293.6	2.194571E+03	2.194571e+03	2.652683E+06	2.652682e+06	1.246251E+05	1.246250e+05
1100	2.074636E+03	2.074636e+03	2.697482E+06	2.697482e+06	1.164763E+05	1.164763e+05
1300	2.049774E+03	2.049774e+03	2.708572E+06	2.708572e+06	1.148073E+05	1.148073e+05

As can be seen from Table 3.5, ADC can calculate the Doppler broadened cross sections with excellent accuracy. Absorption cross sections, computed by ADC, were compared against NJOY at the VHTR average fuel temperature of 1300K and results are shown in Figure 3.11 for the U238 resonances at 6.674eV, 20.871eV, and 36.682eV resonances of U238 and the PU239 resonance at 0.28 eV. U238 and Pu239 are two of the strongest and most important resonance absorber nuclides for thermal reactors. It was found that the maximum relative difference in absorption cross sections over the entire energy grid points is less than 1×10^{-5}% between NJOY and ADC.

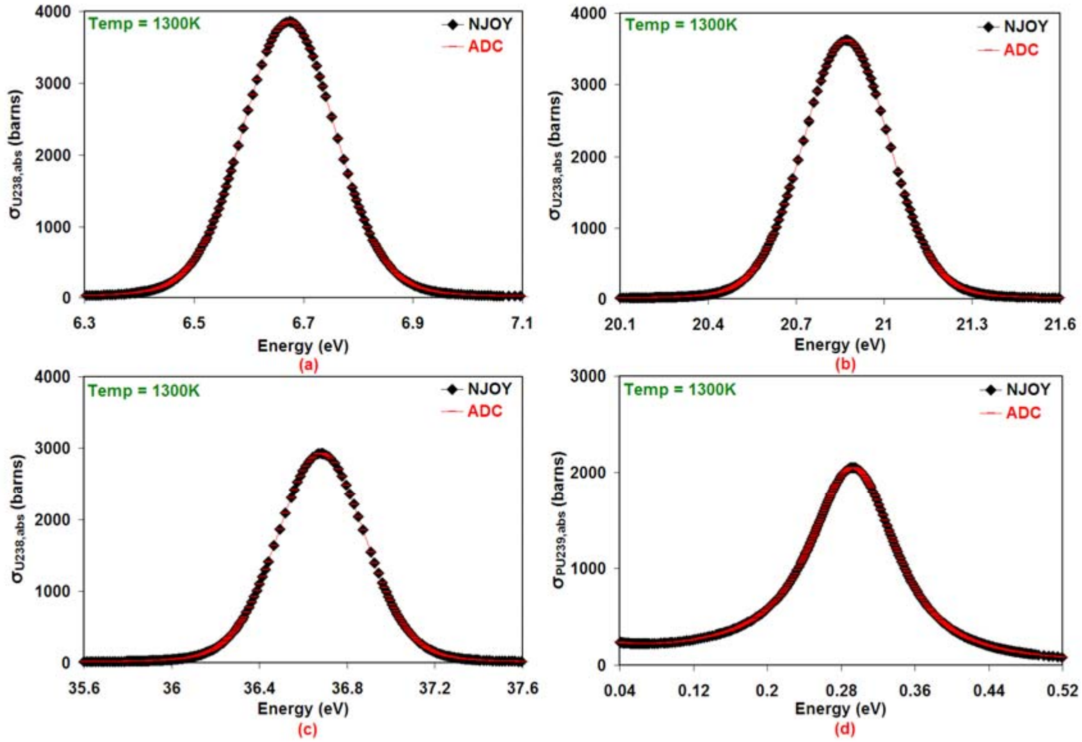

Figure 3.11. Comparison of Resonance Cross Sections between NJOY and ADC.

The comparison between ADC and NJOY was extended to cover resonances of U-238 in the keV range. Since these resonances are very closely spaced, they start interfering with each other when Doppler broadening of the cross sections is performed and must be analyzed carefully. Figure 3.12 shows two closely spaced U235 resonances in keV range where they overlap with increasing material temperature due to the Doppler broadening of the cross sections.

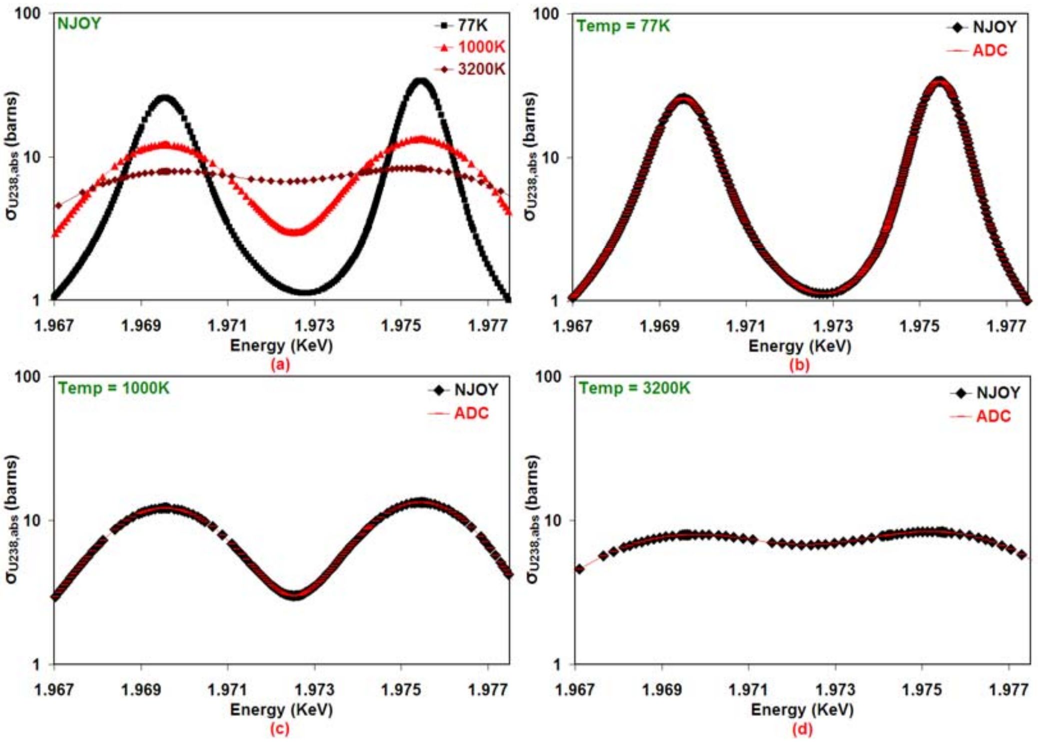

Figure 3.12. Resonance overlapping due to Doppler broadening.

3.4 Numerical Analysis of the Regression Model

The combined Doppler broadening regression model equation developed in the previous section was applied to the discrete temperature dependent U238 absorption cross section data generated by ADC at every 1K interval between 77K and 3200K. Constants of the model equation were adjusted by least squares linear regression.

In regression modeling $\sigma(T)=\sum_{k=1}^{N} a_k f_k(T)$, the term 'linear' does not mean that the function of T itself is linear, but that the model dependence on its parameters a_k is linear. Our model equation has N=13 constants to be adjusted by Least Squares linear regression. In addition, the regression model was compared with the equivalent polynomial regression model of degree N-1.

Figure 3.13 shows the evolution of U238 absorption cross sections as a function of energy at room temperature, T=293.6K. The combined regression model was tested in both the eV and keV energy ranges to ensure that resonance overlapping effects are accounted for.

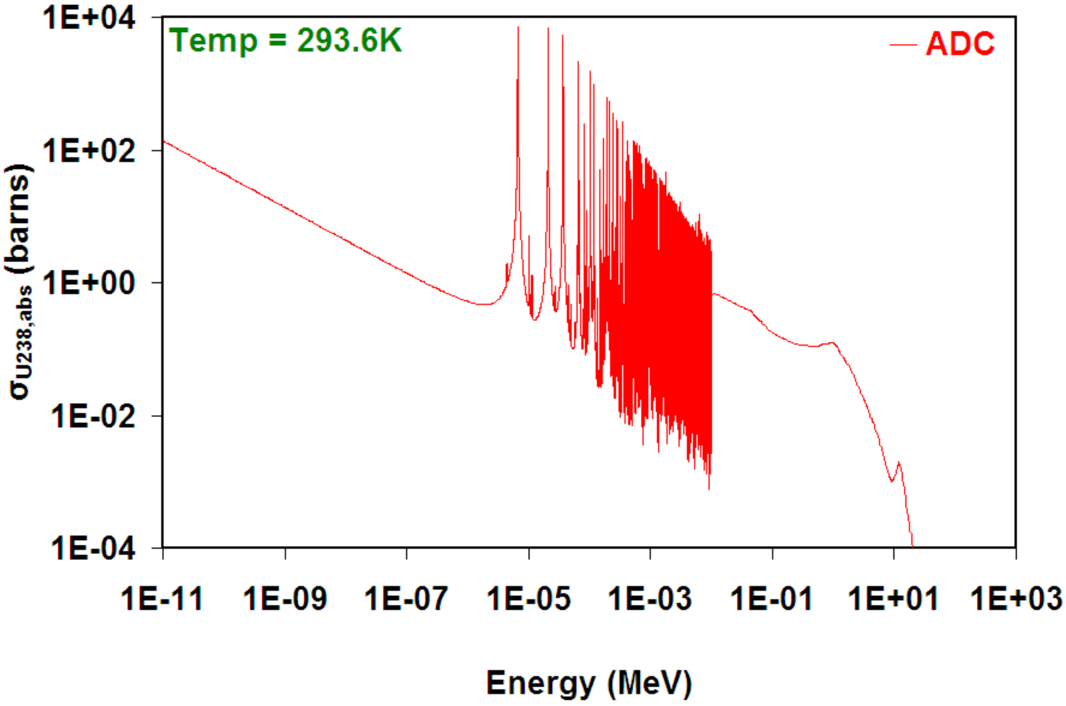

Figure 3.13. σ_a^{U238} as a Function of Energy.

3.4.1 Maximum Relative Error Analysis

After applying our regression model equation to the discrete temperature dependent U238 absorption cross section data at every energy grid point, the maximum relative differences (%) in cross sections were calculated:

$$\text{Max. Relative Diff. (\%)} = MAX_{T\in[77K-3200K]}\left\{\frac{\sigma_a^{Exact}(T)-\sigma_a^{Model}(T)}{\sigma_a^{Exact}(T)}x100\right\} \quad (3.51)$$

Results were compared with the equivalent simple polynomial regression model of degree N-1 as shown in Figure 3.14.

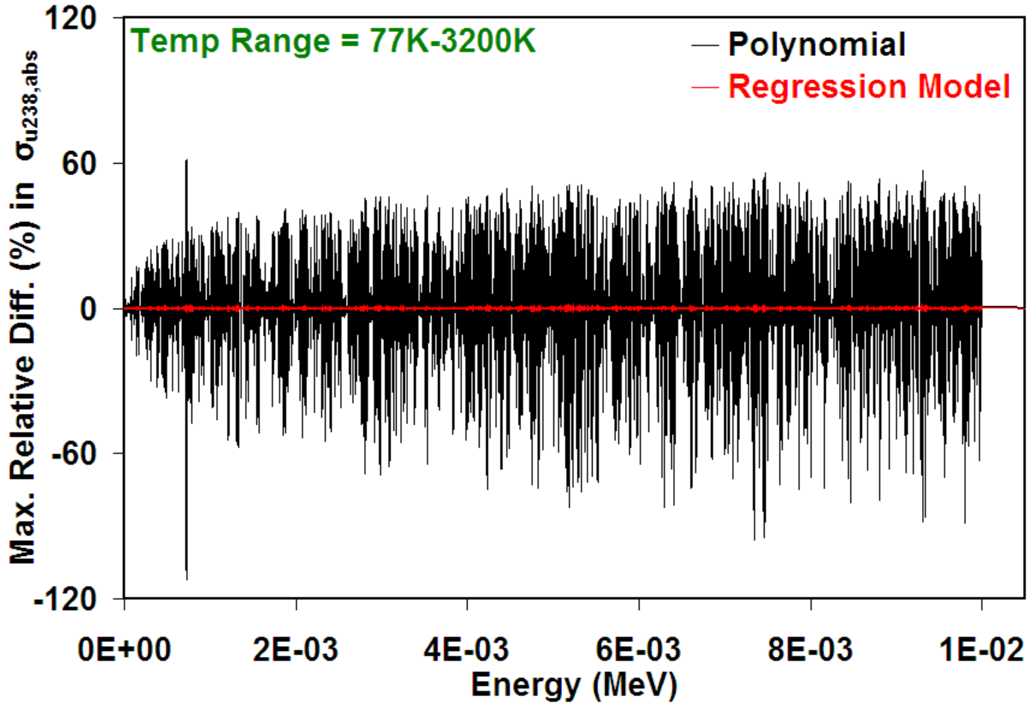

Figure 3.14. σ_a^{U238} as a function of energy.

It was found that our regression model equation can accurately calculate the temperature dependent cross section using N=13 constants adjusted by least squares linear regression. For comparison, an equivalent polynomial regression model of degree N-1 was used resulting in maximum relative differences around 3-4% for the resonances in eV region and up to 100% in the keV region as shown in Figure 3.15.

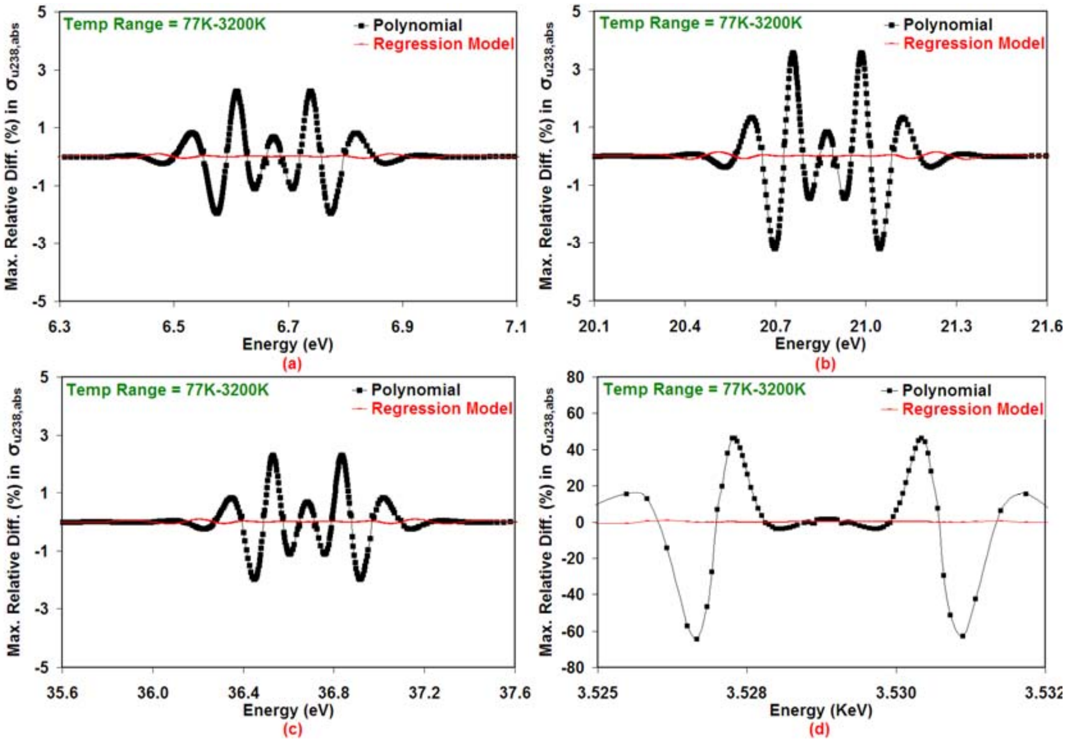

Figure 3.15. Maximum relative differences (%) for σ_a^{U238} at selected resonances.

3.4.2 Residual Scatter Analysis

Residuals for U238 absorption cross sections at selected energy grid points of important resonances were calculated for temperatures in the range 77K and 3200K by applying our linear regression model equation. The main reason to compute the residuals in cross sections was to observe the change of error with temperature. Results were compared with the equivalent simple polynomial regression model of degree N-1 as shown in Figure 3.16. The residual error is defined as follows:

$$\text{Residual error} = \sigma_a^{Exact}\left(T\right)-\sigma_a^{Model}\left(T\right) \tag{3.52}$$

As seen in Figure 3.16a, the maximum residual error in σ_a^{U238} was calculated as $6\text{x}10^{-7}$ barns with our regression model at 77K. Residuals in σ_a^{U238} decrease down to $1\text{x}10^{-9}$ barns as the temperature increases. With the equivalent polynomial model, the residuals change from 5 to 35 barns for those selected energy grid points of important resonances as shown in Figures 3.16b, 3.16c, and 3.16d.

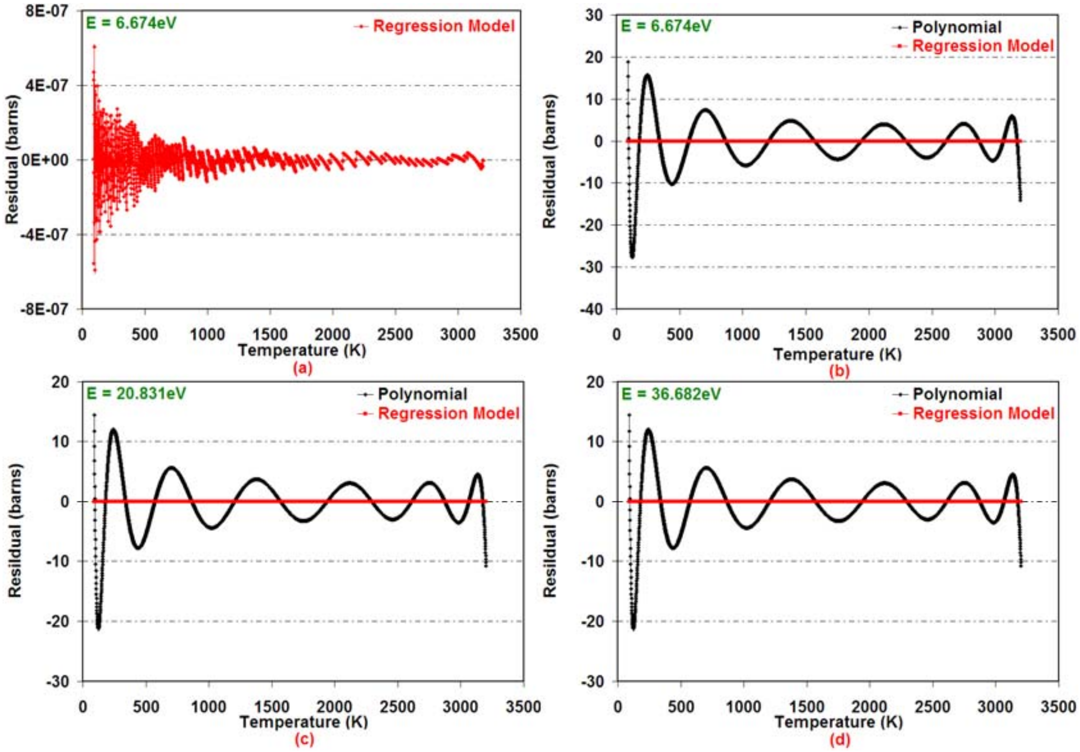

Figure 3.16. Residual scatter for σ_a^{U238} at selected resonance energy grid points.

3.4.3 Goodness of the Linear Regression Model

Another means of comparison is the goodness of the proposed combined regression model as measured by the SSE and RMSE over a given temperature range. The SSE statistic measures the total deviation of the response values from the fit to the response values. It is also called the summed square of residuals. The RMSE statistic is also known as the fit standard error or the standard error of the regression. The SSE and RMSE statistics are defined as:

$$SSE = \sum_{T=77}^{3200} \left[\sigma_a^{Exact}(T) - \sigma_a^{Model}(T) \right]^2 \tag{3.53}$$

$$RMSE = \sqrt{\frac{SSE}{v}} \tag{3.54}$$

where $v = n - m$ is the residual degrees of freedom, n is the number of response values, and m is the number of fitted coefficients estimated from the response values. The quantity v indicates the number of independent pieces of information involving the n data points that are required to calculate the sum of squares. For example, for a temperature range of 77K-3200K and 13 constants in the model equation, v=(3200-77+1)-13=3111.

Plots of SSE and RMSE near selected important resonances of σ_a^{U238} are shown in Figure 3.17. It can be seen that both SSE (~1x10^{-11}) and RMSE (~6x10^{-8}) are very close to zero indicating an outstanding fit of the data to the combined regression model.

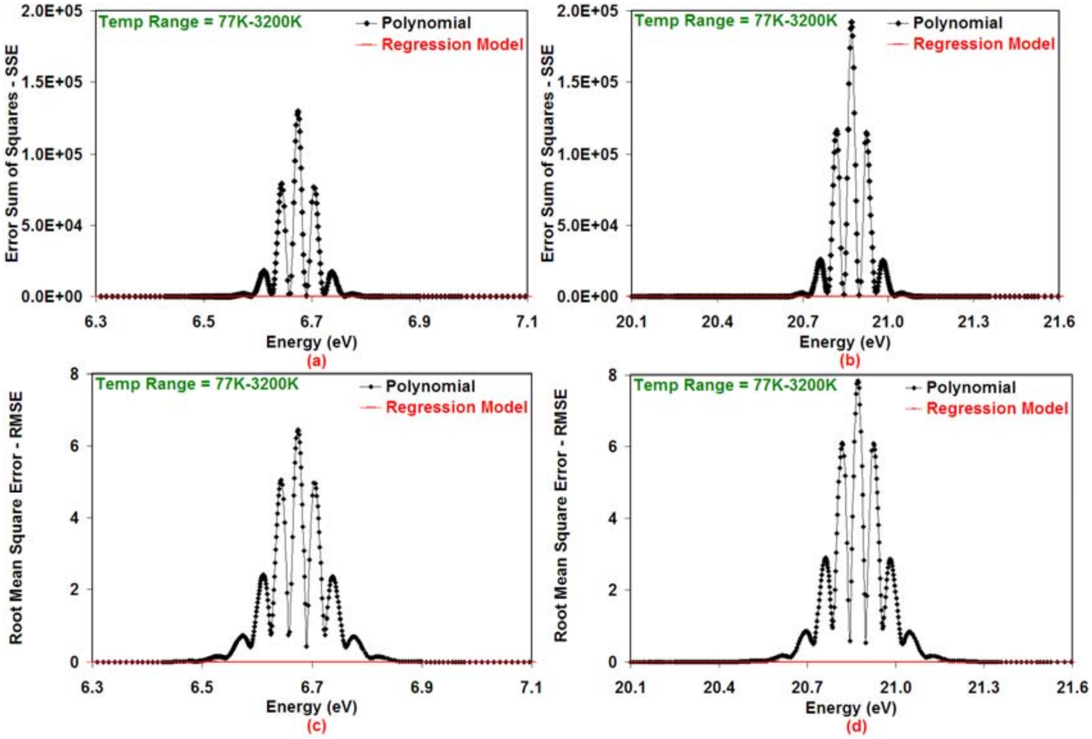

Figure 3.17. SSE and RMSE around selected important resonances of σ_a^{U238}.

3.5 Timing Analysis

A Monte Carlo code was implemented in c++ to determine the computing cost of the combined regression model to calculate broadened cross sections at the energy grid points during the Monte Carlo random walk. This Monte Carlo code is based on well-known methods to sample from the free gas scattering kernel. It was observed that the additional computing cost to evaluate the three sets of cross sections (σ_t, σ_a and σ_f) at a collision site by the combined regression model Eq. (3.24) is less than 1%, compared with the conventional approach where cross sections are linearly interpolated between the energy grid points. So the negligible overhead to perform on-the-fly Doppler broadening can be understood by noting that on-the-fly broadening requires an evaluation of 13 terms in a summation while conventional cross section determination requires linear interpolation between the given grid points. While this difference is not negligible, the computational effort to determine cross sections is relatively small compared to the effort to carry out the random walk of the neutron, including distance to boundary calculations, collision processing, and tallying. For that reason, the overhead is small for our test code and is likely even smaller for a production code with many other options such as MCNP5.

3.5.1 Monte Carlo Code

The thermal distribution of nuclides in a medium can be represented with the Maxwellian Gas model[4,36,37]. Although this model is not exact, it was shown by Lamb[38] that many materials of interest in reactor physics calculations can be treated as an ideal gas at an effective temperature. As the temperature increases, the crystalline effects become less important so the model gets better. Since the purpose of this effort is to obtain reasonable estimates of computational efficiency for a realistic Monte Carlo simulation code, this thermalization model is sufficient.

3.5.1.1 Thermal Motion of Target Nuclide

The following analysis is based on previously published works[36-37]. The distribution of the nuclide energy is given as:

$$M\left(E_t\right)=\frac{2\pi}{\left(\pi kT\right)^{3/2}}\sqrt{E_t}\exp\left(-\frac{E_t}{kT}\right) \tag{3.55}$$

where k is the Maxwell-Boltzmann constant, E_t is the target nuclide energy and T is the material temperature. When the free gas thermal treatment is applied to sample the motion of the target atom in the medium, the reaction rate can be expressed as;

$$R\left(v_t,\mu\right)dv_t d\mu=\left[N\sigma_s\left(v_{rel}\right)\right]\left[v_{rel}M\left(E_t\right)\right]dE_t\frac{d\mu}{2} \tag{3.56}$$

where v_t is the target velocity, v_{rel} is the relative velocity between target nuclide and incoming neutron, N is the number density of the target nuclide in the material region and $\sigma_s\left(v_{rel}\right)$ is the scattering cross section at relative energy.

Historically, the zero temperature scattering cross sections are assumed to be almost independent[2,36,37] of the incoming neutron energy. In practice, the scattering cross section is a slowly varying function of relative velocity for light nuclides. However, they can vary rapidly with relative velocity for heavy nuclides but the moderating effect of scattering is small in that case. Therefore, it is assumed that the variation of $\sigma_s(v)$ with target velocity can be ignored. (This is sufficient for the purpose of our test Monte Carlo code but recent research[39,40,41] has pointed out the importance of strongly varying scattering cross sections in the resonance range of heavy nuclides. This topic is beyond the scope of this thesis.) With this assumption the total reaction rate can be written as

$$R(v_t,\mu)\,dv_t d\mu = \left[N\sigma_s\right]\left[v_{rel} M\left(E_t\right)\right] dE_t \frac{d\mu}{2} \tag{3.57}$$

$M\left(E_t\right)$ can be easily transformed into $M\left(v_t\right)$ with the help of the Jacobian transformation:

$$M\left(v_t\right) = \frac{4}{\sqrt{\pi}}\left[\frac{A}{2kT}\right]^{3/2} v_t^2 \exp\left(-\frac{Av_t^2}{2kT}\right) \tag{3.58}$$

The reaction rate can be rewritten as:

$$R(v_t,\mu)\,dv_t d\mu = \left[N\sigma_s\right]\left[v_{rel}\frac{4}{\sqrt{\pi}}\beta^3 v_t^2 \exp\left(-\beta^2 v_t^2\right)\right] dE_t \frac{d\mu}{2} \tag{3.59}$$

where

$$v_{rel} = \left|v_n - v_t\right| = \left[v_n^2 + v_t^2 - 2v_n v_t \mu\right]^{1/2}, \beta = \left(\frac{A}{2kT}\right)^{1/2} \tag{3.60}$$

Integrating R(v_t, μ) over μ and inserting x=βv_t and a=βv_n, we have;

$$R(x)\,dx = \frac{2N\sigma_s}{3\sqrt{\pi}a}\left[\left(a-x\right)^3 - \left|a-x\right|^3\right] x \exp\left(-x^2\right)\frac{dx}{\beta} \tag{3.61}$$

Integrating R(x) over x, we obtain;

$$R = \int_0^\infty R(x)\,dx = \frac{N\sigma_s a}{\beta}\left[\left(1+\frac{1}{2a^2}\right) erf\left(a\right) + \frac{1}{a\sqrt{\pi}}\exp\left(-a^2\right)\right] \tag{3.62}$$

The Probability Density Function (PDF) for x is calculated by $R\left(x\right)dx/R$:

$$f\left(x\right)dx = \frac{2}{3\sqrt{\pi}a^2}\frac{\left[\left(a-x\right)^3 - \left|a-x\right|^3\right] x \exp\left(-x^2\right)dx}{\left(1+\frac{1}{2a^2}\right) erf\left(a\right) + \frac{1}{a\sqrt{\pi}}\exp\left(-a^2\right)} \tag{3.63}$$

The target velocity-like term x is sampled by using the above probability density function. The probability of having a velocity x decreases rapidly with increasing x due to the exponential term in Eq. (3.62) and becomes almost zero when sampled outside the range of [0,4].

The PDF for the collision angles[42] that would produce the effective cross section for the given neutron and the target velocities is determined by selecting from the distribution for the cosine μ:

$$f(\mu) = C\left[a^2 + x^2 - 2ax\mu\right]^{1/2} \tag{3.64}$$

Then integrating over [-1,1]:

$$\int_{-1}^{1} f(\mu)\,d\mu = 1 \tag{3.65}$$

The constant C is found as:

$$C = \frac{3ax}{(a+x)^3 - |x-a|^3} \tag{3.66}$$

So the PDF for the collision angle is;

$$f(\mu) = 3ax\frac{\left[a^2 + x^2 - 2ax\mu\right]^{1/2}}{(a+x)^3 - |x-a|^3} \tag{3.67}$$

The cumulative PDF can be defined as:

$$\xi = F(\mu) = \int_{-1}^{\mu} f(\mu)\,d\mu \tag{3.68}$$

So μ can be calculated analytically;

$$\mu = \frac{1}{2ax}\left[a^2 + x^2 - \left[(x+a)^3 + \xi\left[|x-a|^3 - (x+a)^3\right]\right]^{2/3}\right] \tag{3.69}$$

where $\xi[0,1]$. With these equations, one can sample the thermal motion of the target atom.

3.5.1.2 Collision Site and Nuclide

The distance to a collision site is sampled by[2]:

$$d_l = -\frac{1}{\Sigma_t}\ln(1-\xi) \tag{3.70}$$

where $\xi[0,1]$. The kth nuclide is chosen as the collision nuclide[2] if

$$\sum_{i=1}^{k-1}\Sigma_{ti} < \xi\sum_{i=1}^{n}\Sigma_{ti} < \sum_{i=1}^{k}\Sigma_{ti} \tag{3.71}$$

where $\xi[0,1]$, n is the total number of nuclides at the collision site and Σ_{ti} is the total cross section of the ith nuclide.

3.5.1.3 Collision Kinematics

The post collision neutron velocity in the LAB frame, $w_{n,lab}$, must be calculated to complete the description of the MC code.

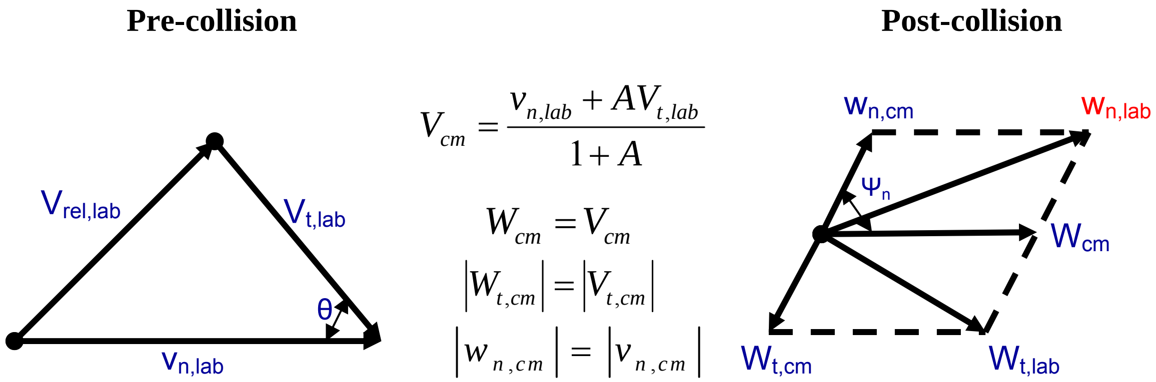

Figure 3.18. Collision kinematics.

Pre- and post- collision lines of travel were rotated through a random angle Ψ_n about W_{cm} or V_{cm}.

$$w_{n,lab} = w_{n,cm} + W_{cm} = w_{n,cm} + V_{cm} = w_{n,cm} + \frac{v_{n,lab} + AV_{t.lab}}{1+A} \tag{3.72}$$

$$w_{n,cm} = \left|v_{n,cm}\right| \Omega_0 \tag{3.73}$$

where Ω_0 is the post-collision unit vector.

$$\left|v_{n,cm}\right| = \left|v_{n,lab} - V_{cm}\right| = \left|v_{n,lab} - \frac{v_{n,lab} + AV_{t,lab}}{1+A}\right| = \frac{A}{1+A}\left|v_{rel,lab}\right| \tag{3.74}$$

$$\left|v_{rel,lab}\right| = \sqrt{v_n^2 + V_t^2 - 2v_n V_t \mu_t}\,, \mu_t = \cos\theta \tag{3.75}$$

$\Omega_0=(u_0,v_0,w_0)$ is isotropic in the center of mass frame. So;

$$w_0 = 2\xi_1 - 1 \tag{3.76}$$

$$u_0 = \sqrt{1-w_0^2}\cos(2\pi\xi_2) \tag{3.77}$$

$$v_0 = \sqrt{1-w_0^2}\sin(2\pi\xi_2) \tag{3.78}$$

where $\xi_1[0,1]$ and $\xi_2[0,1]$. So we have;

$$w_{n.lab} = \frac{A}{1+A}\left|v_{rel,lab}\right|\Omega_0 + \frac{1}{1+A}v_{n,lab} + \frac{A}{1+A}V_{t,lab} \tag{3.79}$$

$$\frac{(1+A)}{\left|v_{n,lab}\right|}w_{n.lab} = \frac{v_{n,lab}}{\left|v_{n,lab}\right|} + A\left[\frac{\left|v_{rel,lab}\right|}{\left|v_{n,lab}\right|}\Omega_0 + \frac{V_{t,lab}}{\left|v_{n,lab}\right|}\right] = \Omega_n + A\left[\delta\Omega_0 + \frac{x}{a}\Omega_t\right] \tag{3.80}$$

where Ω_n and Ω_t are the unit vectors in the v_n and V_t directions. δ is defined as:

$$\delta = \frac{v_{rel,lab}}{v_{n,lab}} = \sqrt{1 + \frac{V_{t,lab}^2}{v_{n,lab}^2} - \frac{2V_{t,lab}}{v_{n,lab}}\mu_t} = \sqrt{1 + \frac{x^2}{a^2} - \frac{2x\mu_t}{a}} \tag{3.81}$$

Defining vector R which is parallel to $w_{n,lab}$:

$$R = \frac{\left(1+A\right)}{\left|v_{n,lab}\right|} w_{n.lab} \tag{3.82}$$

$$R_u = u + A\left(\delta u_0 + \frac{x}{a} u_t\right), R_v = v + A\left(\delta v_0 + \frac{x}{a} v_t\right), R_w = w + A\left(\delta w_0 + \frac{x}{a} w_t\right) \tag{3.83}$$

$$u^{'} = \frac{R_u}{|R|}, v^{'} = \frac{R_v}{|R|}, w^{'} = \frac{R_w}{|R|}, E^{'} = E\frac{R^2}{\left(1+A^2\right)} \tag{3.84}$$

3.5.2 Testing Monte Carlo (MC) Against MCNP5

A simple test problem was setup to compare the accuracy and timing of our Monte Carlo code against MCNP5 in a homogeneous mixture of U-238 and H-1 at 293.6K. A mono-energetic source at 10eV was placed in an infinite medium to populate the U-238 6.67eV resonance at room temperature. Number densities of H-1 and U-238 are 5.9754x10^{-04} and 4.5536x10^{-02} respectively.

Our Monte Carlo code was run by utilizing the on-the-fly regression model and direct use of the exact Doppler broadening Eq. (2.1) separately for the test problem summarized above. As can be seen from Figure 3.19, both MC codes agree with each other perfectly.

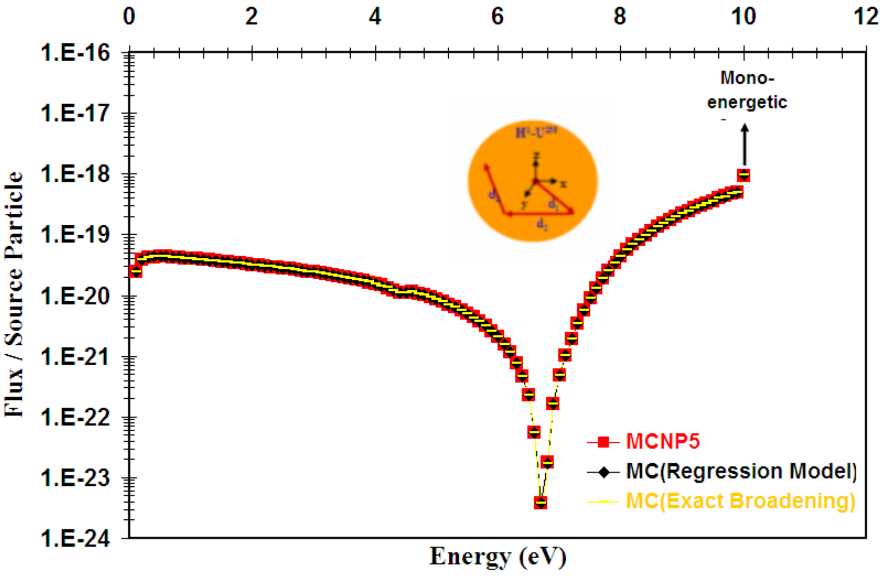

Figure 3.19. Flux Comparison between different broadening methods.

However, the timing result for the exact broadening Monte Carlo case MC(Exact Broadening) is substantially worse than other methodologies. Results are presented in Table 3.6. Utilization of the on-the-fly regression model MC(Regression Model) yields almost the same timing result as MC(Linear Interpolation).

Table 3.6. Computing time.

	CPU Time (min)	X-Sec Calculation
MC(Linear Interpolation)	14.7	Linear Interpolation
MC(Regression Model)	14.8	On-the-fly + Linear interpolation
MC(Exact Broadening)	623.3	Exact

3.6 Calculation of Total NDF Size

In addition to fuel resonance absorbers, there are numerous fission products (FPs) that, as a result of their concentration and thermal neutron absorption cross section, have a strong poisoning effect on reactor operation. As the number of resonance absorbers increases during reactor operation, nuclear data must be loaded into memory at a given temperature in order to perform the Monte Carlo calculations. Therefore, it is important to determine the list of resonance absorbers including FPs for a given uranium based fuel type to estimate the approximate size of the nuclear data that will be needed when accounting for Doppler broadening.

The lattice physics burnup code, CPM3[32], was chosen to determine the list of resonance absorbers including FPs. The CPM-3 code package includes a nuclear data file derived from ENDF/B-VI that contains cross-section data and nuclear parameters in 97 energy groups for over 300 nuclides. This nuclear data file includes extended data representations to perform resonance treatments and isotopic burnup calculations of fuel and fission product chains and burnable absorber materials.

A simple VHTR[43] fuel compact cell with a homogeneous fuel region was set up in CPM3 as shown in Figure 3.20. Reflected boundary conditions were specified on the boundaries of the hexagonal fuel compact cell. Room temperature (293.6K) was used in the fuel and moderator regions. The fuel compact radius is 0.6225cm and the fuel compact cell center-to-flat distance is 0.9398cm.

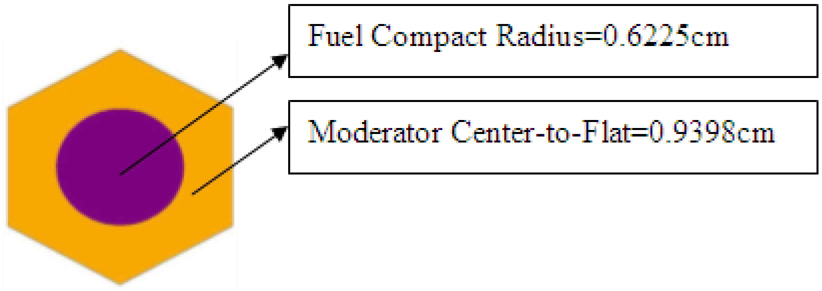

Figure 3.20. VHTR Fuel Compact Cell.

The material composition of the fuel compact cell is given in Table 3.7. The natural boron concentration in the moderator region was specified as 6.9 ppm.

Table 3.7. Material Composition.

	CPM3	MCNP5	
Fuel Compact	**Weight (%)**	**Number Density (at/cc)**	**Density (g/cc)**
U-235	1.2689E+00	6.4621E-05	1.9877E+00
U-238	1.0978E+01	5.5203E-04	
C	8.0158E+01	7.9957E-02	
O	1.2360E+00	9.2499E-04	
Si	6.3587E+00	2.7206E-03	
Moderator	**Weight (%)**	**Number Density (at/cc)**	**Density (g/cc)**
C	9.9999E+01	8.7241E-02	1.7384E+00
B-10	1.3743E-04	1.4369E-07	
B-11	6.0823E-04	5.7838E-07	

In CPM3, burnup steps were specified as accumulated exposure in GWd/MT-HM. Table 3.8 presents the burnup steps in GWd/MT-HM used for the CPM3 calculation.

Table 3.8. Burnup Steps and Accumulated Exposure in GWd/MT-HM.

Burnup Step	GWd/MT-HM	Burnup Step	GWd/MT-HM	Burnup Step	GWd/MT-HM	Burnup Step	GWd/MT-HM
0	0.0	**10**	1.0	**20**	12.5	**30**	55.0
1	0.1	**11**	2.0	**21**	15.0	**31**	60.0
2	0.2	**12**	3.0	**22**	17.5	**32**	65.0
3	0.3	**13**	4.0	**23**	20.0	**33**	70.0
4	0.4	**14**	5.0	**24**	25.0	**34**	75.0
5	0.5	**15**	6.0	**25**	30.0	**35**	80.0
6	0.6	**16**	7.0	**26**	35.0	**36**	85.0
7	0.7	**17**	8.0	**27**	40.0	**37**	90.0
8	0.8	**18**	9.0	**28**	45.0	**38**	95.0
9	0.9	**19**	10.0	**29**	50.0	**39**	100.0

At the end of each burnup step, the list of resonance absorber nuclides can be found for each fuel material region in the CPM3 output file. Table 3.9 presents all of the resonance absorber nuclides including FPs encountered during the time to reach 100 GWd/MT-HM burnup.

Table 3.9. Resonance Absorber Nuclides.

Resonance Absorber Nuclides for The Fuel Compact									
U234	U235	U236	U238	NP237	PU238	PU239	PU240	PU241	PU242
AM241	AM242	AM243	CM242	CM244	KR83	ZR93	MO95	MO97	TC99
RU101	RH103	RH105	PD105	PD108	AG109	CD113	IN115	XE131	XE135
CS133	CS134	CS135	CE141	PR141	ND143	ND145	PM147	PM148	PM148m
SM147	SM149	SM150	SM151	SM152	EU153	EU154	EU155		

As a result of this burnup analysis, 48 resonance absorber nuclides were generated for the uranium based fuel. Then, NJOY99 was used to generate temperature dependent nuclear data files for each resonance absorber nuclide in Table 3.9 using a fractional tolerance of 0.1%. Two different temperatures, T=1100K and T=1300K, were used, corresponding to average fuel temperatures for PWR and VHTR configurations, respectively. Table 3.10 gives the total size of the cross section files needed for these isotopes for the union grid versus the conventional approach where cross sections for two temperatures are stored. Although the storage requirement for the union grid is higher, it provides cross sections for all temperatures in the range 77K-3200k, whereas the PWR and VHTR entries only provide cross sections for two temperatures.

Table 3.10. Total Data File Size of 48 Resonance Absorber Nuclides for MCNP5.

	Union Grid	**PWR**	**VHTR**
	T=77K-3200K	**T=1100K**	**T=1300K**
Total Size (MB)	195	132	129

To estimate the amount of cross section storage needed for a realistic case, it was assumed that each fuel rod (or fuel compact) in the problem would have its own temperature. Using this assumption and the results in Table 3.10, Table 3.11 presents these estimates for full core VHTR and LWR configurations. Table 3.12 shows the amount of storage needed for on-the-fly Doppler broadening, which does not depend on the number of fuel rods or fuel compacts.

Table 3.11. Cross section storage for conventional Doppler broadening.

	Assembly Type	Size of NDFs/Road (MB)	# of Assemblies	Fuel Rods / Assembly	Sym	# of Regression Constants	Total size (GB)
PWR	Square	132	193	264	1/8	N/A	841
VHTR	Prismatic	129	1020	222	1/12	N/A	2,434

Table 3.12. Cross section storage for on-the-fly Doppler broadening.

	Assembly Type	Size of NDFs/Road (MB)	# of Assemblies	Fuel Roads / Assembly	Sym	# of Regression Constants	Total size (GB)
PWR	Square	195	N/A	N/A	N/A	13	2.5
VHTR	Prismatic	195	N/A	N/A	N/A	13	2.5

As illustrated in Table 3.12, the new on-the-fly Doppler method is independent of the number of temperature regions for any given problem and the approximate total size of the 48 resonance nuclear data files, generated by CPM3, was calculated to be ~2.5GB, covering the temperature range of 77K-3200K. Furthermore, the accuracy in cross sections for all nuclides, energies, and temperatures was found to be in excellent agreement with NJOY when the proposed regression model was used. Moreover, the storage required to perform the same analysis by using the discrete temperature dependent nuclear data files is prohibitive, requiring 841GB for a typical PWR configuration and 2,434GB space for a typical VHTR configuration.

CHAPTER 4

Coupled Monte Carlo / Collision Probability Method for VHTR Analysis

4.1 Theory

Two different methodologies were developed to account for the first level heterogeneity due to fuel kernels within a conventional lattice physics code. The initial approach involved the simultaneous execution of MCNP5 and CPM3, with direct communication of MCNP5 shielded multi-group resonance cross sections into CPM3 during the simulation, effectively overwriting the CPM3 resonance integrals. This task was performed with the help of an Application Program Interface (API), developed to link the CPM-3 and MCNP5 codes. Subsequently, an alternative approach was developed based on defining a double heterogeneity factor (DHF), yielding similar results but with substantial advantages for realistic VHTR analyses. Actually, the DHF method involves an array of DHFs for each nuclide, with a separate DHF computed for each of two different microscopic cross sections (absorption and nu-fission) for each of 65 resonance groups, or 130 DHFs per nuclide. The DHF approach was applied to both CPM3 and Helios[44] lattice physics codes.

Computation of shielded multi-group cross sections of any type can be performed in MCNP5 by tallying the corresponding multi-group flux and reaction rate within a given region of interest, for a given resonance nuclide and reaction type. The desired multi-group resonance microscopic cross section of any type in a given region can be calculated as:

$$\sigma^{i}_{x,g} = \frac{A^{i}_{x,g}}{\phi^{i}_{g}} \tag{4.1}$$

where i is the material region, x is the type of reaction and g is the energy group. ϕ^{i}_{g} and $A^{i}_{x,g}$ are group fluxes and reaction rates in region i respectively. $A^{i}_{x,g}$ is defined as:

$$A^{i}_{x,g} = \sum_{r \in g} \int_{\text{res r}} \sigma^{i}_{x,r}(E)\phi^{i}_{r}(E)dE \tag{4.2}$$

where the summation is taken over all resonances r within energy group g. The CPM3 multi-group energy structure was introduced into MCNP5 to compute $\sigma^{i}_{x,g}$ by tallying multi-group fluxes and reaction rates in fuel kernels for each resonance nuclide.

4.1.1 Direct Communication of Cross Sections between MCNP5 and CPM3

With this approach, CPM3 analyzes the homogeneous assembly model at the same time that MCNP5 analyzes the heterogeneous assembly model. MCNP5 calculates 65 group resonance shielded effective resonance cross sections (σ_a and $\nu\sigma_f$) in each fuel kernel, averaged over the whole assembly for the resonance absorber materials (U-235 and U-238). These assembly-averaged 65 group cross sections are transferred to CPM3 during the coupled execution of MCNP5 and CPM3. CPM3 then proceeds to perform its transport calculation of the homogeneous fuel assembly with the MCNP5 resonance cross sections. The communication between CPM-3 and MCNP5 was managed by an Application Program Interface (API), which is described next.

4.1.1.1 Application Program Interface

CPM-3 is a code system comprised of six modules. The logic flow diagram of the CPM-3 code is illustrated in Figure 4.1.

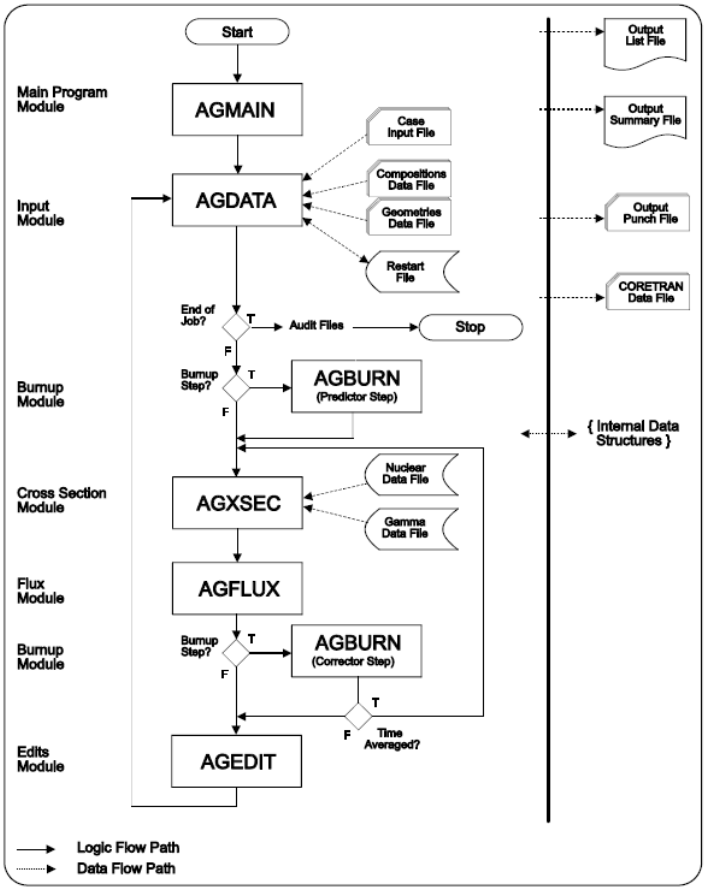

Figure 4.1. Logic flow diagram of CPM3.

Each code module performs a specific task such as processing user input data, performing the flux calculation and editing the results of the calculations. Each loop through the program represents an eigenvalue calculation or a burnup step. The cross section processing module AGXSEC was modified to allow it to use MCNP5-generated multi-group effective resonance cross sections in CPM3. Since these cross sections are properly shielded, they account for the double heterogeneity. Macroscopic cross sections are prepared based on the microscopic cross sections in the AGXSEC module for each nuclide to perform flux, reaction rate edit, and burnup calculations. The resonance self-shielding calculation is performed within a fuel rod (or compact) for absorber nuclides within this module. Ray-tracing is used to calculate generalized Dancoff factors in a two dimensional lattice but again this option is not needed if MCNP5 cross sections are used. In fact, since the resonance cross sections computed by CPM3 are overwritten by the MCNP5-generated cross sections, much of the existing coding in AGXSEC is moot for this approach.

The API consists of a Fortran-90 code that was implemented and embedded in the CPM3 source code to couple CPM3 and MCNP5. It prepares the MCNP5 flux and reaction rate tallies for the corresponding double heterogeneous configuration to calculate shielded microscopic resonance cross sections (σ_γ , σ_f and $\nu\sigma_f$) for each resonance nuclide. Capture and fission cross sections are combined to obtain absorption cross sections. Once the MCNP5 code is executed, the resulting reaction rates and fluxes are used to obtain resonance absorption and fission cross sections for the resonance nuclides and these cross sections are communicated to CPM3 for its subsequent analysis. The average reaction rate and group flux are computed over all fuel kernels within the assembly for each resonance group and nuclide in MCNP5. Then, Eq. (4.1) is used to calculate assembly averaged cross sections of any type to feed into CPM3. The following Figure 4.2 illustrates the logic flow diagram of the coupling methodology.

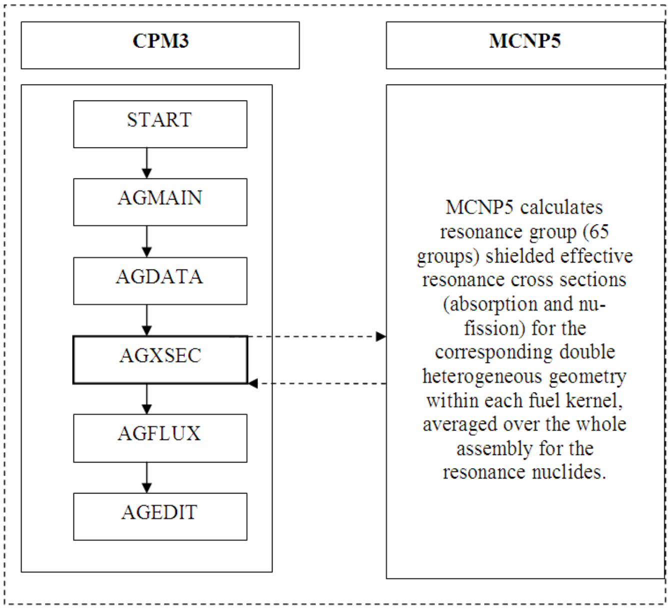

Figure 4.2. CPM3-MCNP5 coupling.

The calculation of the fine group resonance cross sections is performed in subroutine EFRES1. Subroutines EFRES2 and SHDXS perform resonance calculations based on a two-term rational approximation. These subroutines are called within module AGXSEC. A Fortran-90 code fragment was embedded into the subroutine called EFRES2 to stop the CPM3 effective multi-group resonance calculation, generate the MCNP5 input file, perform the MCNP5 calculation, calculate the fine group resonance cross sections, and update the CPM3 resonance cross section arrays prior to performing any region-wise macroscopic cross section and transport calculation.

The 65-group resonance cross sections determined by MCNP5 were transferred back into CPM3 with the API. Two 2-D arrays, one for each isotope, were created in CPM3 to hold the MCNP5-generated 65-group resonance absorption and fission cross sections. These arrays, ABSMOD and FISMOD, are described in Table 4.1:

Table 4.1. New arrays to store resonance cross sections.

Array	Description
ABSMOD (1,1:65)	U-235 absorption x-sections
ABSMOD (2,1:65)	U-238 absorption x-sections
AFISMOD (1,1:65)	U-235 fission x-sections
AFISMOD (2,1:65)	U-238 fission x-sections

The following code was also implemented into EFRES2 routine to insert the MCNP5 resonance cross sections in CPM3. In addition, 3-D arrays called SA and SNYF in CPM3 hold the 65-group resonance absorption and ν-fission cross sections respectively, as shown in Figure 4.3.

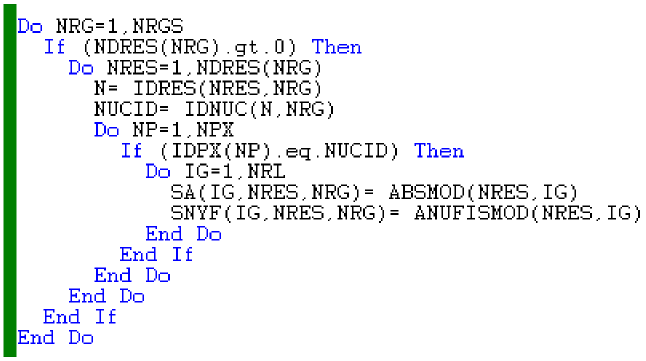

```
Do NRG=1,NRGS
  If (NDRES(NRG).gt.0) Then
    Do NRES=1,NDRES(NRG)
      N= IDRES(NRES,NRG)
      NUCID= IDNUC(N,NRG)
      Do NP=1,NPX
        If (IDPX(NP).eq.NUCID) Then
          Do IG=1,NRL
            SA(IG,NRES,NRG)= ABSMOD(NRES,IG)
            SNYF(IG,NRES,NRG)= ANUFISMOD(NRES,IG)
          End Do
        End If
      End Do
    End Do
  End If
End Do
```

Figure 4.3. Inserting MCNP5 resonance x-sections into EFRES2.

After importing and inserting the MCNP 65-group resonance cross sections into CPM3, all of the microscopic cross section data is written into a CPM3 internal file by the code to calculate the region-wise macroscopic cross sections and perform the flux calculation.

There are some disadvantages with this approach. The treatment of depletion would be quite tedious with this direct approach because both CPM3 and MCNP5 would need to be depleted simultaneously. In addition, spatial dependence of resonance cross sections of any type requires additional factorization as a function of space within a given assembly. Therefore, an alternative methodology was developed based on the Double Heterogeneity Factor (DHF), yielding similar results with the direct approach but with substantial advantages for realistic VHTR analyses.

4.1.2 Double Heterogeneity Factor (DHF) Approach

The basic idea behind the DHF approach is that CPM3 and MCNP5 will yield approximately the same cross sections for an assembly with a homogeneous fuel region (i.e., no particle level heterogeneity). Therefore, two MCNP5 calculations, with homogeneous and heterogeneous fuel regions, can be used to define a correction factor which is the ratio of the group cross sections for these two cases. If this ratio (or correction factor) is then applied to the CPM3 cross section, the resultant cross section should be close to the MCNP5 heterogeneous cross section. Therefore, CPM3 analyzes the assembly with homogeneous fuel model whereas MCNP5 analyzes configurations that include both heterogeneous and homogeneous fuel regions, to calculate DHFs once for at Beginning of Life (BOL). (It has been found that the DHF is not sensitive to burnup, which is discussed later.) MCNP5 calculates 65 group resonance DHFs for both absorption and nu-fission reactions within each fuel kernel, averaged over the whole assembly for the resonance absorber materials (U-235 and U-238). These assembly-averaged 65 group DHFs are read into CPM3. Then CPM3 performs its transport calculation by multiplying its resonance group cross sections (calculated with homogeneous fuel regions) by the MCNP5 DHFs. In essence, the method can be summarized by the following equation:

$$\sigma_{xg}^{i,\mathrm{CPM3-MOD}} \approx \sigma_{xg}^{i,\mathrm{MCNP-het}} \tag{4.3}$$

where $\sigma_{xg}^{i,MCNP-het}$ is the MCNP5-generated fine group g resonance cross section for isotope i and $\sigma_{xg}^{i,CPM3-MOD}$ is the corresponding cross section in CPM3 after the DHF is applied. In other words, the fine group resonance cross sections from a heterogeneous fuel MCNP5 calculation replace the fine group resonance cross sections computed by CPM3 using homogeneous fuel.

The new approach is ostensibly a minor variation on the original method but it has major implications for ease of use and practicality for routine analysis, and can be applied to more general configurations than the original method. The new method can be described by the following equation:

$$\sigma_{xg}^{i,CPM3-MOD} \approx \sigma_{xg}^{i,CPM3} \times DHF_{xg}^{i} \tag{4.4}$$

where DHF_{xg}^{i} is a "correction factor", basically a "self-shielding factor" and can be defined as:

$$DHF_{xg}^{i} = \frac{\text{fine group x} - \text{sec tion from MCNP5}\left(\text{heterogeneous fuel compacts}\right)}{\text{fine group x} - \text{sec tion from MCNP5}\left(\text{hom ogeneous fuel compacts}\right)} \tag{4.5}$$

$$DHF_{xg}^{i} = \frac{\sigma_{xg}^{i,MCNP5-het}}{\sigma_{xg}^{i,MCNP5-hom}} \tag{4.6}$$

In this case, the DHF multiplies the CPM3 cross section and consists of the ratio of fine group resonance cross sections computed by MCNP5 for heterogeneous fuel versus homogeneous fuel. For comparison, the earlier cross section replacement method is equivalent to using a DHF defined by:

$$DHF_{xg}^{alt,i} = \frac{\text{fine group x} - \text{sec tion from MCNP5}\left(\text{heterogeneous fuel compacts}\right)}{\text{fine group x} - \text{sec tion from CPM3}\left(\text{hom ogeneous fuel compacts}\right)} \tag{4.7}$$

$$\mathrm{DHF}_{xg}^{alt,i} = \frac{\sigma_{xg}^{i,MCNP5-het}}{\sigma_{xg}^{i,CPM3}} \tag{4.8}$$

Since CPM3 can analyze a VHTR configuration with homogeneous fuel, the denominators of Eqs. (4.6) and (4.8) should be about the same, i.e., $\sigma_{xg}^{i,CPM3} \approx \sigma_{xg}^{i,MCNP5-hom}$ hence $\mathrm{DHF}_{xg}^{alt,i} \approx \mathrm{DHF}_{xg}^{i}$, and the resultant corrected resonance cross sections $\sigma_{xg}^{i,CPM3-mod}$ from both methods should be comparable. The DHF approach has a number of advantages which will be discussed later.

4.1.3 Description of VHTR Fuel Assembly

A heterogeneous VHTR fuel assembly with explicit TRISO fuel was constructed in MCNP5. The corresponding homogenized assembly was modeled in both MCNP5 and CPM3. The VHTR fuel assembly is composed of 222 fuel compacts and 109 coolant holes. The MCNP5 assembly geometry consisted of three different hexagonal unit cells corresponding to coolant holes (white), fuel compacts (yellow), and graphite regions (green) as shown in Figure 4.4. The outer graphite edge of the assembly was modeled explicitly with both MCNP5 and CPM3. The distance between two flat surfaces is 0.3581 m.

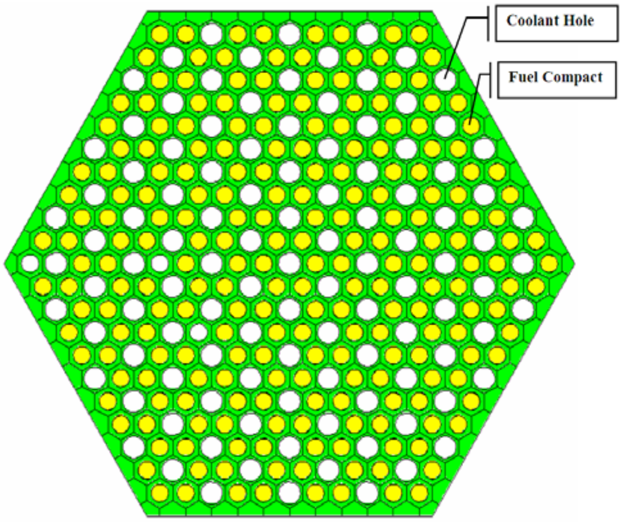

Figure 4.4. Cross-section view of the VHTR fuel assembly.

4.1.3.1 Geometry

The VHTR fuel compact cell is an idealized unit cell that consists of a fuel compact surrounded by its share of the graphite in an assembly. It is a useful geometry because it is simple yet includes the double heterogeneity, and can be used to compare alternative computational models. For the VHTR, the compact cell is composed of an inner cylindrical fuel compact and an outer hexagonal graphite moderator region containing boron impurities. The fuel compact region consists of fuel kernels surrounded by SiC and PyC layers. The packing fraction is 29%. Table 4.2 summarizes the dimensions of the VHTR fuel compact that is modeled by both MCNP5 and CPM3.

Table 4.2. Heterogeneous and homogeneous VHTR fuel compact cell dimensions.

Fuel Particle		**Fuel Compact**		**Hexagonal Compact Cell**	
	Radius (cm)	*Radius (cm)*	*Height (cm)*	*Pitch (cm)*	*Height (cm)*
Fuel Kernel	0.0175	0.6225	4.5553	1.8796	4.5553
Porous PyC	0.0275	**Coolant Hole**			
Inner PyC	0.0315	*Radius (cm)*	*Height (cm)*		
SiC	0.0350	0.7938	4.5553		
Outer PyC	0.0390				

4.1.3.2 Material Composition

Number densities and weight fractions for the fuel compacts that were used by MCNP5 and CPM3 are summarized in Table 4.3.

Table 4.3. Material composition of fuel compact for MCNP5 and CPM3 calculations.

MCNP5	**MCNP5**	**CPM3**
Heterogeneous Fuel Compact Cell	**Homogeneous Fuel Compact Cell**	**Homogeneous Fuel Compact Cell**
Fuel Kernel *N (at/cc)*	*N (at/cc)*	*Weight (%)*
U-235 2.4749E-03	*U-235* 6.4622E-05	*U-235* 1.2691E+00
U-238 2.1142E-02	*U-238* 5.5204E-04	*U-238* 1.0981E+01
C 1.1808E-02	*C* 7.9957E-02	*C* 8.0153E+01
O 3.5426E-02	*O* 9.2499E-04	*O* 1.2363E+00
	Si 2.2706E-06	*Si* 6.3603E+00
Porous PyC		
C 5.0183E-02		
Inner PyC		
C 9.5348E-02		
SiC		
C 4.8060E-02		
Si 4.8060E-02		
Outer PyC		
C 9.5348E-02		
Graphite Matrix		
C 8.5312E-02		
Moderator	*Moderator*	*Moderator*
C 8.7241E-02	*C* 8.7241E-02	*C* 9.9999E+01
B-10 1.4369E-07	*B-10* 1.4369E-07	*B-10* 1.3743E-04
B-11 5.7838E-07	*B-11* 5.7838E-07	*B-11* 6.0823E-04

4.1.3.3 Modeling of Fuel Assembly with MCNP5

A hexagonal fuel assembly universe was filled with the bodies shown in Figure 4.5 to obtain the full fuel assembly model shown in Figure 4.4. The repeated structure feature in MCNP5 makes this relatively easy. Reflecting boundary conditions were specified on each face of the hexagonal assembly.

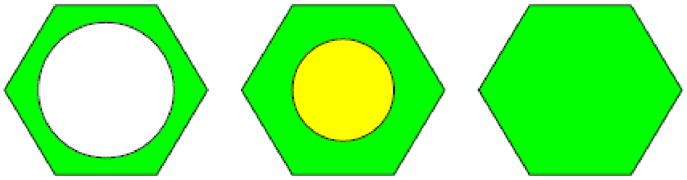

Figure 4.5. Repeating cells in the VHTR fuel assembly.

4.1.3.4 Modeling of Fuel Assembly with CPM3

A different approach to construct the assembly had to be found with CPM3 because of its restricted geometry features. Bodies must be defined explicitly in CPM3 but the graphite bodies on the outer surface of the assembly are different sizes and are aligned at different rotational angles. The bodies that are available in CPM3 are shown in Figure 4.6 and these can only be rotated by 90, 180, or 270 degrees. Because of these restrictions, the VHTR assembly shown in Figure 4.4 cannot be explicitly modeled with CPM3.

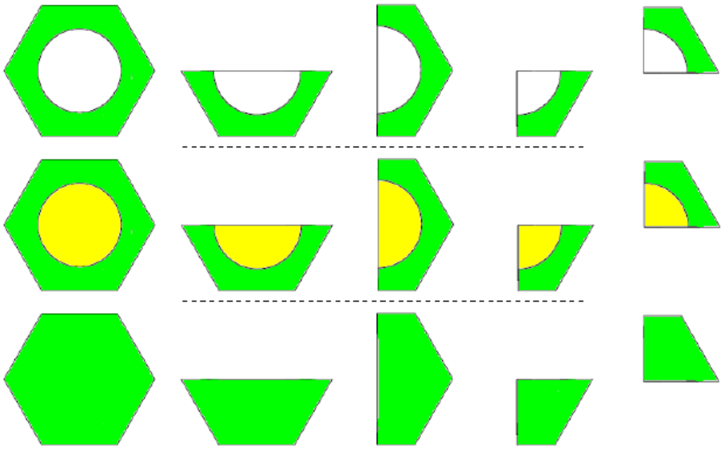

Figure 4.6. Available hexagonal unit cells in CPM3.

This problem was overcome by identifying a portion of the repeating hexagonal lattice that is rectangular with reflecting boundary conditions, which can be modeled by

CPM3. Portions of two assemblies were combined to model an infinite hexagonal lattice of fuel assemblies. This is shown in Figure 4.7, where the rectangle (marked with solid red lines) represents a repeating rectangular geometry that exactly represents an infinite lattice of hexagonal assemblies. Thus the rectangle in Figure 4.7 models the VHTR fuel assembly exactly, including the outer graphite edge. For this rectangular region, the available bodies and allowable rotational angles are sufficient to allow CPM3 to model the geometry shown in Figure 4.7, which corresponds to an infinite lattice of hexagonal fuel assemblies.

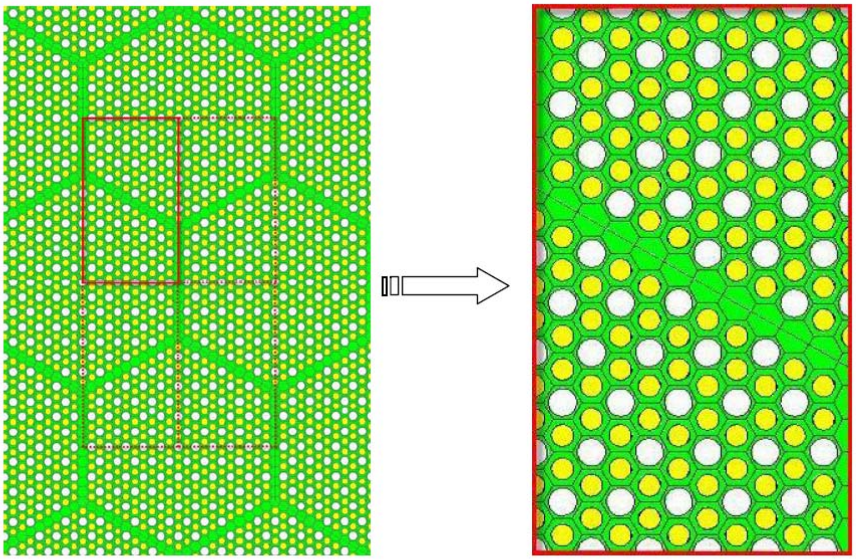

Figure 4.7. CPM3 Model of the VHTR Assembly Lattice.

Homogeneous MCNP5 and CPM3 models were obtained by homogenizing the fuel region as shown in Figure 4.8. Only the TRISO fuel region is homogenized and the homogeneous and heterogeneous fuel assemblies are otherwise identical to Figure 4.4.

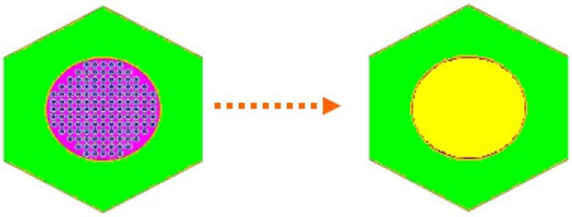

Figure 4.8. Heterogeneous and corresponding homogeneous model.

4.1.4 CPM3 Energy Group Structure

The CPM-3 code package includes a nuclear data file derived from ENDF/B-VI that contains cross-section data and nuclear parameters in 97 energy groups for over 300 nuclides. Neutron cross section data is provided in 97 energy groups over the energy range of 0-10 MeV. Gamma-ray cross-section data is provided in 18 energy groups up to 10 MeV. The user may specify condensed energy group structures for both eigenvalue and editing calculations by using the discrete energy group boundaries given on the nuclear data file. There are 65 resonance energy groups that are numbered from 25 to 89. Groups 1-24 are the fast neutron groups where there are no resolved resonances, and groups 90-97 are the lower thermal energy groups that are below the resonance range. Multi-group energy boundaries of CPM3 are shown in Table 4.4. Resonance groups are marked with red.

Table 4.4. CPM3 97 Multi-Group Energy Boundaries.

Grp	Energy Range (eV)	Grp	Energy Range (eV)	Grp	Energy Range (eV)
1	1.00E+07 - 7.79E+06	**34**	2.61E+03 - 2.04E+03	**67**	1.31E+00 - 1.17E+00
2	7.79E+06 - 6.07E+06	**35**	2.04E+03 - 1.59E+03	**68**	1.17E+00 - 1.10E+00
3	6.07E+06 - 4.72E+06	**36**	1.59E+03 - 1.23E+03	**69**	1.10E+00 - 1.07E+00
4	4.72E+06 - 3.68E+06	**37**	1.23E+03 - 9.61E+02	**70**	1.07E+00 - 1.06E+00
5	3.68E+06 - 2.87E+06	**38**	9.61E+02 - 7.49E+02	**71**	1.06E+00 - 1.05E+00
6	2.87E+06 - 2.23E+06	**39**	7.49E+02 - 5.83E+02	**72**	1.05E+00 - 1.04E+00
7	2.23E+06 - 1.74E+06	**40**	5.83E+02 - 4.54E+02	**73**	1.04E+00 - 1.01E+00
8	1.74E+06 - 1.35E+06	**41**	4.54E+02 - 3.54E+02	**74**	1.01E+00 - 9.51E-01
9	1.35E+06 - 1.05E+06	**42**	3.54E+02 - 2.75E+02	**75**	9.51E-01 - 7.82E-01

10	1.05E+06 - 8.21E+05	**43**	2.75E+02 - 2.15E+02	**76**	7.82E-01 - 6.25E-01
11	8.21E+05 - 6.39E+05	**44**	2.15E+02 - 1.67E+02	**77**	6.25E-01 - 5.03E-01
12	6.39E+05 - 4.98E+05	**45**	1.67E+02 - 1.30E+02	**78**	5.03E-01 - 4.17E-01
13	4.98E+05 - 3.88E+05	**46**	1.30E+02 - 1.01E+02	**79**	4.17E-01 - 3.58E-01
14	3.88E+05 - 3.02E+05	**47**	1.01E+02 - 7.89E+01	**80**	3.58E-01 - 3.21E-01
15	3.02E+05 - 2.35E+05	**48**	7.89E+01 - 6.14E+01	**81**	3.21E-01 - 3.01E-01
16	2.35E+05 - 1.83E+05	**49**	6.14E+01 - 4.79E+01	**82**	3.01E-01 - 2.91E-01
17	1.83E+05 - 1.43E+05	**50**	4.79E+01 - 3.73E+01	**83**	2.91E-01 - 2.71E-01
18	1.43E+05 - 1.11E+05	**51**	3.73E+01 - 2.90E+01	**84**	2.71E-01 - 2.51E-01
19	1.11E+05 - 8.65E+04	**52**	2.90E+01 - 2.26E+01	**85**	2.51E-01 - 2.28E-01
20	8.65E+04 - 6.74E+04	**53**	2.26E+01 - 1.76E+01	**86**	2.28E-01 - 1.84E-01
21	6.74E+04 - 5.25E+04	**54**	1.76E+01 - 1.37E+01	**87**	1.84E-01 - 1.46E-01
22	5.25E+04 - 4.09E+04	**55**	1.37E+01 - 1.07E+01	**88**	1.46E-01 - 1.12E-01
23	4.09E+04 - 3.18E+04	**56**	1.07E+01 - 8.32E+00	**89**	1.12E-01 - 8.20E-02
24	3.18E+04 - 2.48E+04	**57**	8.32E+00 - 6.48E+00	**90**	8.20E-02 - 5.69E-02
25	2.48E+04 - 1.93E+04	**58**	6.48E+00 - 5.04E+00	**91**	5.69E-02 - 4.28E-02
26	1.93E+04 - 1.50E+04	**59**	5.04E+00 - 3.93E+00	**92**	4.28E-02 - 3.06E-02
27	1.50E+04 - 1.17E+04	**60**	3.93E+00 - 3.06E+00	**93**	3.06E-02 - 2.05E-02
28	1.17E+04 - 9.12E+03	**61**	3.06E+00 - 2.38E+00	**94**	2.05E-02 - 1.24E-02
29	9.12E+03 - 7.10E+03	**62**	2.38E+00 - 1.86E+00	**95**	1.24E-02 - 6.33E-03
30	7.10E+03 - 5.53E+03	**63**	1.86E+00 - 1.73E+00	**96**	6.33E-03 - 2.28E-03
31	5.53E+03 - 4.31E+03	**64**	1.73E+00 - 1.60E+00	**97**	2.28E-03 - 2.53E-04
32	4.31E+03 - 3.36E+03	**65**	1.60E+00 - 1.46E+00		
33	3.36E+03 - 2.61E+03	**66**	1.46E+00 - 1.31E+00		

The CPM3 data file is based on ENDF/B-VI Release IV whereas MCNP5 uses ENDF/B-VI Release V. It was reported in the CPM3 nuclear data manual[45] that ENDF/B-VI Release V virtually gives identical results as ENDF/B-VI Release IV for thermal reactors. Although they give identical results for the light water reactors, the results are very different for CANDU reactors, which are also thermal reactors but use D2O rather than H2O as moderator[46].

4.2 Computational Results

4.2.1 Sensitivity Study

Since CPM3 was designed to analyze LWR lattices, the key numerical integration parameters for the collision probability calculation were analyzed in detail for the infinite lattice of the VHTR assemblies. The integration parameters are the spacing between integration lines and the number of angles chosen to represent the 360 degree rotation of the integration lines. Table 4.5 shows the multiplication factor results for the case of the VHTR assembly shown in Figure 4.4. The default spacing and number of angles in CPM3 are 0.1 cm and 9 angles, respectively.

Table 4.5. Numerical integration parameters for CPM3 calculations.

Spacing (cm)	Number of Angles	k_{inf}
0.1	9	1.4375
0.1	12	1.4391
0.1	60	1.4380
0.1	90	1.4381
0.05	9	1.4375
0.05	12	1.4391
0.05	60	1.4380
0.05	90	1.4381
0.01	9	1.4374
0.01	12	1.4390
0.01	60	1.4380
0.01	90	1.4381

As a result of the CPM3 sensitivity study, the spacing was chosen to be 0.1 cm and the number of angles was chosen to be 60 (shaded yellow in Table 4.5), yielding the optimum CPM3 ray tracing parameters for the VHTR assembly configuration.

4.2.2 Direct Transfer of Cross Sections

Direct transfer of shielded cross sections, provided by MCNP5, into CPM3, yields excellent agreement with the corresponding double heterogeneous MCNP5 case for both k_{inf} and resonance escape probability. MCNP5 was chosen as the reference case due to its flexible geometric modeling feature to account for all spatial heterogeneities within the geometry of interest, including the double heterogeneities posed by TRISO fuel. Table 4.6 presents the infinite medium multiplication factors and resonance escape probability (P_{esc}) obtained with the coupled MCNP5-CPM3 (modified) methodology compared with the standalone CPM3 (original) calculations for the infinite lattice of assemblies described above. The CPM3 calculation was performed with both transport options: the Method of Characteristics (MOC) and the Collision Probability Method (CPM), and are shown in Table 4.6. The relative difference between MOC and CPM was found to be negligible. For the purpose of comparing the coupled MCNP5/CPM3 methodology, the CPM option was chosen for the transport calculation, providing benchmark-quality results and was used for the rest of the assembly calculations discussed in this report. The assembly configuration as well as geometry and material composition was summarized in the previous section.

Table 4.6. Coupled MCNP5/CPM3 vs CPM3 for VHTR Fuel Assembly.

	MCNP5 (ref)	**CPM3 (original)**	**Difference (%)**	**CPM3 (modified)**	**Difference (%)**
$K_{inf-moc}$	1.4975	1.4409	3.8	1.4970	.03
$K_{inf-cpm}$	1.4975	1.4409	3.8	1.4970	.03
P_{esc}	0.704	0.675	4.1	0.705	-.14

The relative difference in the infinite medium multiplication factors for the coupled MCNP5-CPM3 calculations was found to be 0.03% for the fuel assembly with heterogeneous fuel, as shown in Table 4.6. In this case, CPM3 by itself can only treat the fuel as homogeneous and yields k_{inf} = 1.4409, compared to 1.4975 for MCNP5, thus showing that it totally misses the particle fuel heterogeneity posed by the TRISO fuel. On the other hand, if MCNP5 resonance cross sections are inserted into CPM3, k_{inf} becomes 1.4970, which is very close to the MCNP5 result. This agreement is very encouraging and affirms the basic methodology.

Since k_{inf} is a global parameter, it may be masking errors from different portions of the CPM3 calculation unrelated to the resonance calculation. Therefore, a comparison of the resonance escape probability, p_{esc}, was also performed and was included in Table 4.6, with excellent results. This quantity is a direct measure of the accuracy of the resonance calculation, which is the only portion of the CPM3 methodology that is changed.

4.2.3 DHF Approach

4.2.3.1 VHTR Assembly

Multi-group DHFs were calculated with MCNP5 for each of the resonance nuclides (U-235 and U-238) in fuel kernels, averaged over an assembly with reflected boundary conditions. DHFs were read into CPM3 to multiply the homogeneous fuel compact cross sections to yield self shielded resonance cross sections accounting for the double heterogeneity. The assembly configuration, geometry and material composition were summarized in the previous section.

Results are given in Tables 4.7 and 4.8 with two different lattice physics codes, CPM3 and Helios.

Table 4.7. DHF Approach with CPM3.

	MCNP5 (ref)	**CPM3 (original)**	**Difference (%)**	**CPM3 (modified)**	**Difference (%)**
$K_{inf\text{-}cpm}$	1.4975	1.4409	3.8	1.4990	-.10

Table 4.8. DHF Approach with HELIOS.

	MCNP5 (ref)	**Helios (original)**	**Difference (%)**	**Helios (modified)**	**Difference (%)**
$K_{inf\text{-}cpm}$	1.4975	1.4458	3.4	1.4951	.16

The relative difference in infinite multiplication factor was found to be -0.10% with CPM3 whereas the difference goes up to 0.16% with Helios. Although the results for both codes are quite good, the fact they disagree can be explained in terms of the differences in nuclear data files, different resonance approximation methods and different resonance energy group structures. In summary, both CPM3 and Helios lattice physics codes yield reasonable results in k-inf for VHTR configurations when used with the DHF approach.

4.2.3.2 Deep Burn Concept – Driver Fuel Compact

While the use of nuclear power grows, the waste produced by the existing nuclear reactors increases at the same rate. In other words, new repository capacity equal to the Yucca Mountain in US is required about every 20 years[47]. Therefore, a new concept called Deep Burn[47,48] was proposed to use thermal Modular Helium Reactor systems

(MHRs) for the transmutation of waste from nuclear reactors. As an essential feature of this concept, ceramic coated fuel particles are used. They are strong enough, durable and have high resistance to irradiation, providing extensive destruction levels in one burnup cycle. All of the weapon-usable materials as well as 95% of all transuranics (TRUs) can be destroyed. With the Deep Burn concept, nuclear waste volume and toxicity can be reduced, avoiding the construction of new repository sites. In other words, one of the most important limitations to expand the nuclear power capacity can be eliminated. However, the analysis of this concept is complicated because the fuel consists of TRU isotopes (e.g., plutonium and neptunium) that are recycled from thermal reactors.

The applicability of the double heterogeneity factor (DHF) approach was tested for the analysis of TRISO fuel in CPM3 lattice physics calculations for a realistic TRU fuel composition characteristic of the Deep Burn concept developed by General Atomics. The MCNP5 and CPM3 cases were performed for the fuel compact, where the fuel kernel comprises Pu-Np-CO, representing the Pu-Np isotopics in typical used nuclear fuel (UNF) from light water reactors. The purpose of this simulation was to check the applicability of the Double Heterogeneity Factor (DHF) methodology to treat the low-lying resonances of Pu-loaded fuel. Although the uranium-fueled cases have TRU isotopes as a result of burnup, the concentration of these isotopes is far less than would be encountered with Deep Burn fuel, and one can expect the DHFs will be somewhat different as a result.

Driver fuel compact cell dimensions are different than that of VHTR. The kernel diameter and the buffer layer thickness were chosen to limit particle internal pressure arising from the fission products from the deep burnup and the helium generated from alpha decay of the TRUs. Tucker's Deep Burn design report[49] was used to perform the analysis for the driver fuel. Driver fuel geometry and resonance material composition are presented in Table 4.9 and Table 4.10, respectively.

Table 4.9. Deep Burn - Driver fuel compact cell dimensions

Region	**Radius (cm)**
Fuel Kernel	0.0150
Buffer PyC	0.0300
Inner PyC	0.0335
SiC	0.0370
Outer PyC	0.0410
Driver Fuel Compact	0.6223
Region	**Radius (cm)**
Moderator	0.9398

Table 4.10. Driver fuel material composition.

Resonance Nuclide	**Weight (%)**
Np-237	5.2
Pu-238	1.5
Pu-239	57.0
Pu-240	23.0
Pu-241	8.3
Pu-242	5.0

Several CPM3 calculations were performed to assess the adequacy of the DHF approach, compared with our original approach based on replacement of the CPM3 resonance group cross sections with cross sections from a heterogeneous MCNP5 run. The heterogeneous MCNP5 run is considered to be the benchmark calculation as mentioned earlier. Three different CPM3 calculations were performed for homogenized driver fuel, using different cross sections for the 65 resonance groups in CPM3 as summarized in Table 4.11.

Table 4.11. Explanation of different Deep Burn cases.

Case Number	Case Name	Description
1	**MCNP5 (het)**	MCNP5 calculation with heterogeneous TRISO fuel.
2	**CPM3 (orig)**	Original version of CPM3 with its own 65 group resonance cross sections.
3	**CPM3 (mod2)**	Direct replacement of 65 group resonance absorption and nu-fission cross sections with MCNP5 cross sections.
4	**CPM3 (mod3)**	Using DHFs from MCNP5 to correct 65 group resonance absorption and nu-fission cross sections in CPM3.

In order for CPM3 to run for the Pu lattices, a trace amount of uranium (10^{-5} %) was required. This is small enough to have no effect on the resultant CPM3 run. This is probably a consequence of the fact that CPM3 was designed for slightly enriched uranium fuel. The infinite multiplication factors k_∞ for the three CPM3 cases are compared in Table 4.12 with those from the two MCNP5 cases.

Table 4.12. Infinite Multiplication Factor Comparison

Case #	Case Name	k_{inf}
1	**MCNP5 (het)**	1.1043
2	**CPM3 (orig)**	1.0347
3	**CMP3 (mod1)**	1.1038
4	**CMP3 (mod2)**	1.1032

The test of the DHF methodology is the comparison of Cases 1 and 4, where the difference is approximately 0.1%, indicating the DHF methodology is yielding excellent results for Pu-fueled fuel compacts. A comparison of Cases 1 and 3 indicates that our original methodology of replacing CPM3 cross sections with MCNP5 cross sections yields better results ((<.05%) than the DHF methodology. However, the advantages of the DHF approach, coupled with its acceptable results, make this the preferred methodology. Overall, the comparison indicates that the DHF approach provides a sufficiently accurate treatment for the TRISO double heterogeneity for realistic Pu-Np compositions for Deep Burn applications.

4.2.4 Detailed DHF Analysis

In order to determine the applicability of the DHF approach for the analysis of TRISO fuel in lattice physics calculations, the effort was extended to assess the DHF sensitivity to spatial location in the assembly, burnup, and packing fraction. The motivation for this work was to minimize the number of MCNP5 runs by parameterizing the calculation of DHFs from a few MCNP5 runs and then build a "library" of DHFs that CPM3 could use without having to repeat the MCNP5 calculations.

4.2.4.1 Spatial Dependence

DHFs were calculated for fuel compacts at different locations in an assembly to determine the spatial dependence of the DHFs. Two limiting assembly configurations shown in Figure 4.9 were analyzed to calculate 65 group DHFs for U-238 and U-235. One case is an assembly with reflecting boundary conditions representative of an interior assembly near the center of the core, and the second is a configuration representative of an exterior assembly near the outer edge of the core.

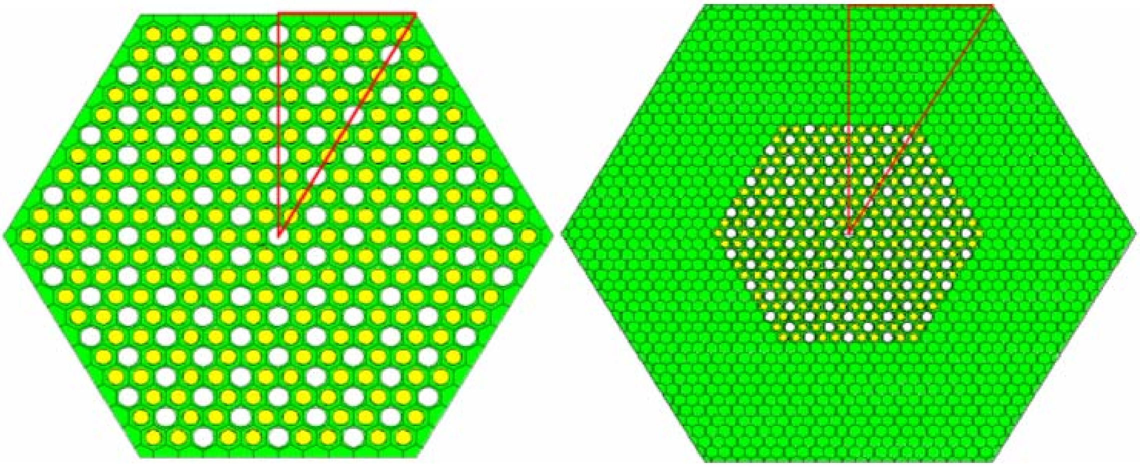

Figure 4.9. Two limiting assembly configurations; interior and exterior.

Spatial distribution of DHFs was determined for a 1/12 symmetric portion of the fuel assembly as shown in Figure 4.9 marked with red triangles. Results were obtained for all 65 resonance groups but are only shown for the important resonance energy groups for U-238 shown in Table 4.13, which includes both low and high energy resonances:

Table 4.13. Energy Group Boundaries.

Grp	*Lower (eV)*	*Higher (eV)*
57	6.476	8.315
53	17.6	22.6
51	29.02	37.27
38	748.5	961.1

The MCNP5 simulations for the heterogeneous and the corresponding homogeneous assembly configurations used 500,000 histories per cycle with a total of 400 active cycles, yielding standard deviations in k_{eff} of less than .004% and in the DHF of less than 0.5%. Figures 4.10-4.13 show the comparison of the DHFs for the energy groups given in Table 4.13 for these limiting assembly configurations. Standard deviations in flux as well as Reaction Rate (R.R.) are also shown in Figures 4.10-4.13.

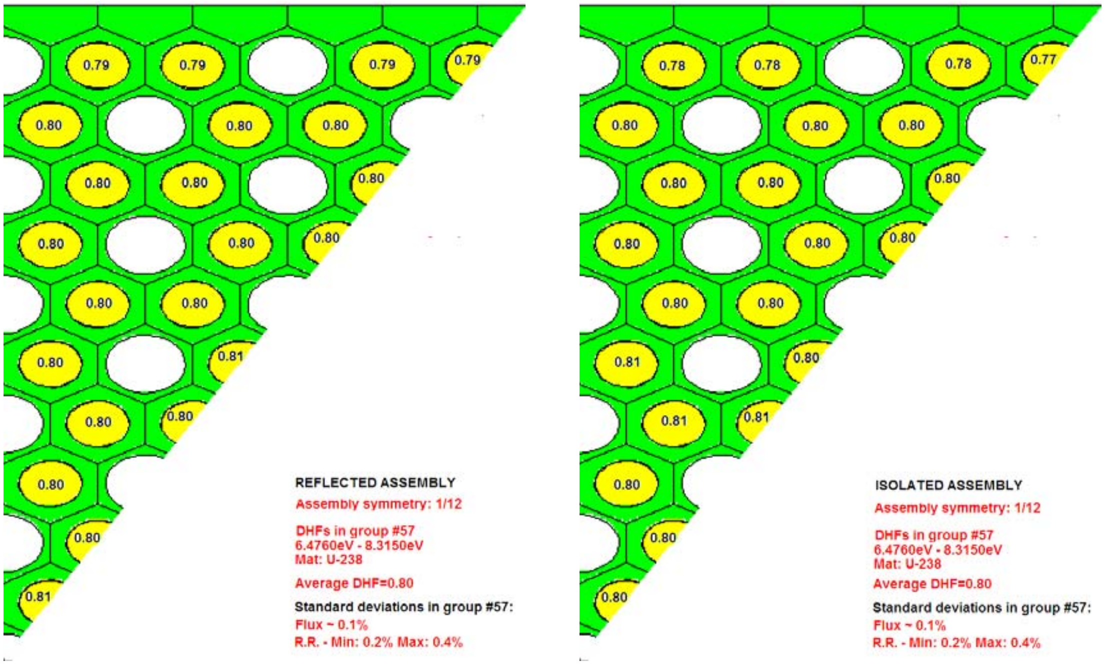

Figure 4.10. Spatial comparison of DHFs over two limiting assemblies at group #57.

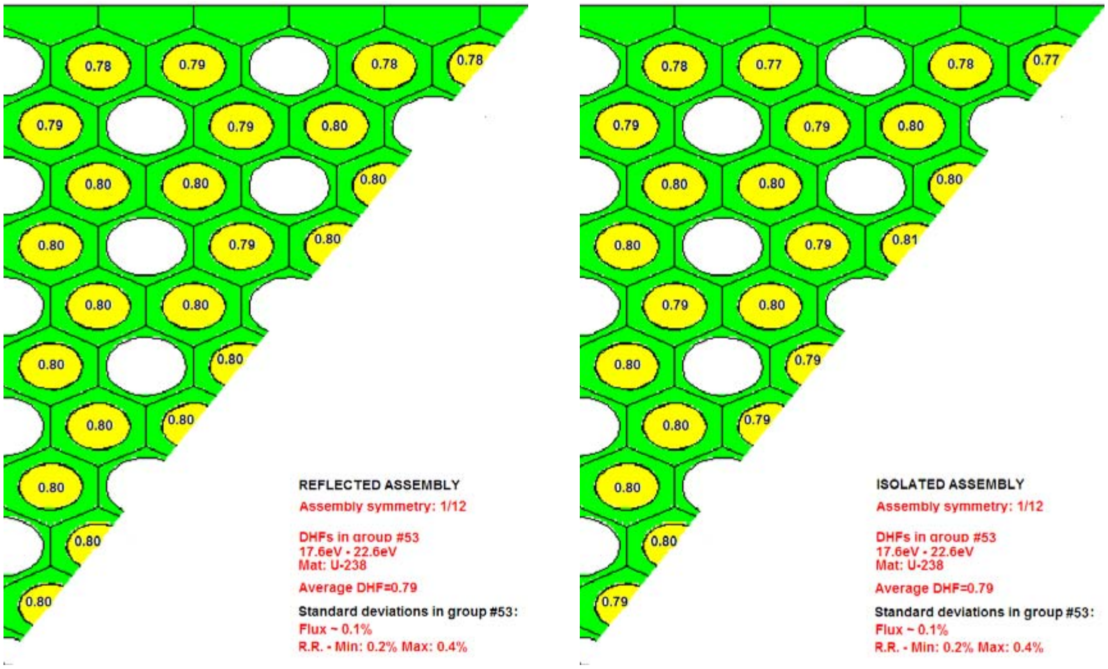

Figure 4.11. Spatial comparison of DHFs over two limiting assemblies at group #53.

Figure 4.12. Spatial comparison of DHFs over two limiting assemblies at group #51.

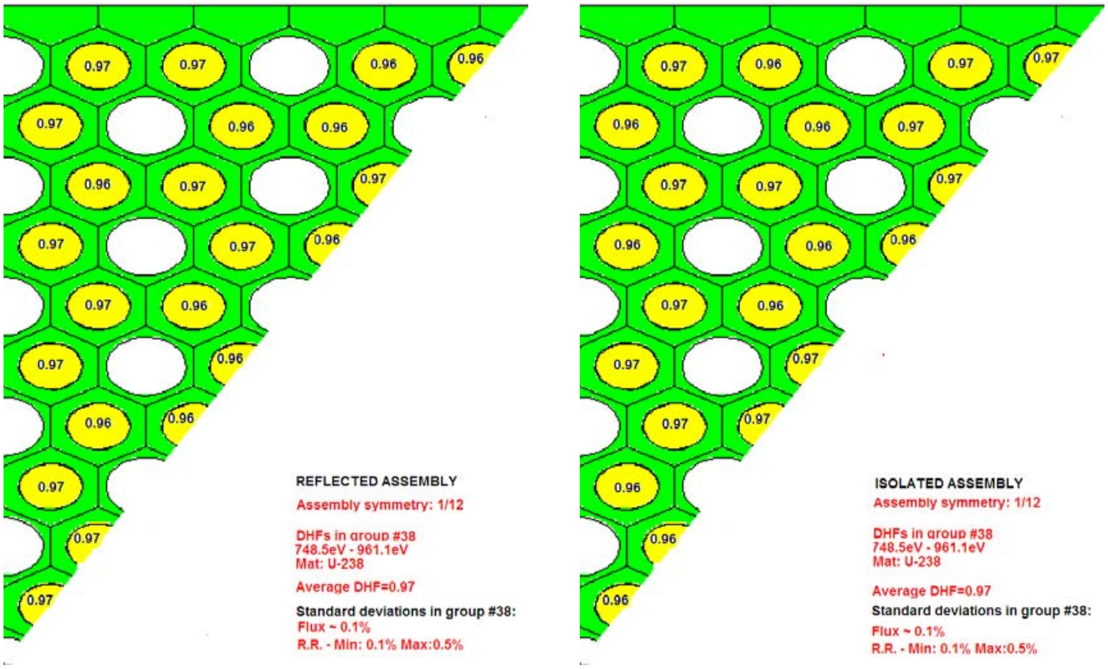

Figure 4.13. Spatial comparison of DHFs over two limiting assemblies at group #38.

As can be seen in Figures 4.10-4.13, spatial dependence of the DHFs, calculated in fuel kernels and averaged over each fuel compact, is negligible for these limiting assemblies. They were found to be within the standard deviation in each of the limiting assemblies except the edges. The small deviation of the DHFs at the edges is due to the effect of the moderator region surrounding the assemblies. Dancoff factors at the edges change slightly but the DHFs are still very close to assembly averaged multi-group DHFs, yielding a negligible effect on k-inf as shown previously. As will be shown later, Dancoff factors mainly depend on the kernel packing fraction in fuel compacts.

Furthermore, DHFs are almost the same for the corresponding fuel compact locations within the two limiting assemblies, suggesting the use of one set of multi-group DHFs for each resonance nuclide and VHTR fuel assembly at any location in the full core. It should also be pointed out that the DHFs for U-235 are equal to, or close to, unity for all resonance groups. This is due to the fact that the concentration of U-235 is relatively dilute compared to U-238, hence the self-shielding is relatively small, leading to a DHF close to unity.

4.2.4.2 Material Composition Dependence

The original lattice physics burnup code CPM3 was used to deplete the fuel materials in an infinite lattice of fuel compact cells with a total burnup of 100GWd/MT-HM. Burnup time steps are presented in Table 3.8. The accumulation of the fission products were accurately determined by specifying very fine initial time steps. The initial heterogeneous and homogeneous VHTR fuel compact cell dimensions as well as material composition are illustrated in Table 4.2 and Table 4.3. Resonance material compositions as a function of burnup are shown in Table 4.14 for the MCNP5 and CPM3 cases.

Table 4.14. Resonance material compositions as a function of burnup time step.

	0 GWd/MT-HM	**50 GWd/MT-HM**	**100 GWd/MT-HM**
Compact	**MCNP Het**	**MCNP Het**	**MCNP Het**
	(at/cc)	(at/cc)	(at/cc)
Fuel			
U-235	2.4749E-03	1.2494E-03	4.6613E-04
U-238	2.1142E-02	2.0426E-02	1.9546E-02
PU-239	0.0000E+00	3.4243E-04	3.6760E-04
PU-240	0.0000E+00	6.0620E-05	1.0465E-04
Compact	**MCNP Hom**	**MCNP Hom**	**MCNP Hom**
	(at/cc)	(at/cc)	(at/cc)
Fuel			
U-235	6.4621E-05	3.2622E-05	1.2171E-05
U-238	5.5203E-04	5.3335E-04	5.1036E-04
PU-239	0.0000E+00	8.9412E-06	9.5983E-06
PU-240	0.0000E+00	1.5828E-06	2.7325E-06
Compact	**CPM3**	**CPM3**	**CPM3**
	Weight (%)	Weight (%)	Weight (%)
Fuel			
U-235	1.2689E+00	6.4566E-01	2.4291E-01
U-238	1.0978E+01	1.0691E+01	1.0316E+01
PU-239	0.0000E+00	1.7999E-01	1.9483E-01
PU-240	0.0000E+00	3.1996E-02	5.5697E-02

As can be seen in Table 4.14, the initial number density of U-235 decreases by 50% at 50GWd/MT-HM and 81% at 100GWd/MT-HM. On the other hand, total PU concentration at 100GWd/MT-HM becomes almost the same as the final concentration of U-235. The decrease in U-238 concentration was found to be 6% at 100GWd/MT-HM.

MCNP5 calculations were performed by using 50,000 histories/batch with a total of 200 active cycles. The resultant statistics were found to be less than 0.1%. The DHFs were calculated for each nuclide at burnup time steps 0, 50 and 100 MWd/MT-HM. Results are illustrated in Table 4.15.

Table 4.15. Multi-group DHFs at different burnup time steps.

	0 GWd/MT-HM				**50 GWd/MT-HM**				**100 GWd/MT-HM**			
	U^{235}	U^{238}	PU^{239}	PU^{240}	U^{235}	U^{238}	PU^{239}	PU^{240}	U^{235}	U^{238}	PU^{239}	PU^{240}
25	1.00	1.00	0.00	0.00	1.00	1.00	1.00	1.00	1.00	1.00	1.00	1.00
26	1.00	1.00	0.00	0.00	1.00	1.00	1.00	1.00	1.00	1.00	1.00	1.00
27	1.00	1.00	0.00	0.00	1.00	1.00	1.00	1.00	1.00	1.00	1.00	1.00
28	1.00	1.00	0.00	0.00	1.00	1.00	1.00	1.00	1.00	1.00	1.00	1.00
29	1.00	1.00	0.00	0.00	1.00	1.00	1.00	1.00	1.00	1.00	1.00	1.00
30	1.00	0.99	0.00	0.00	1.00	0.99	1.00	1.00	1.00	0.99	1.00	1.00
31	1.00	1.00	0.00	0.00	1.00	1.00	1.00	1.00	1.00	1.00	1.00	1.00
32	1.00	0.99	0.00	0.00	1.00	0.99	1.00	1.00	1.00	0.99	1.00	1.00
33	1.00	0.99	0.00	0.00	1.00	0.99	1.00	1.00	1.00	0.99	1.00	1.00
34	1.00	0.98	0.00	0.00	1.00	0.98	1.00	1.00	1.00	0.98	1.00	1.00
35	1.00	0.97	0.00	0.00	1.00	0.97	1.00	1.00	1.00	0.97	1.00	1.00
36	1.00	0.98	0.00	0.00	1.00	0.98	1.00	1.00	1.00	0.98	1.00	1.00
37	1.00	0.97	0.00	0.00	1.00	0.97	1.00	1.00	1.00	0.97	1.00	1.00
38	1.00	0.97	0.00	0.00	1.00	0.97	1.00	1.00	1.00	0.97	1.00	1.00
39	1.00	0.96	0.00	0.00	1.00	0.96	1.00	1.00	1.00	0.96	1.00	1.00
40	1.00	0.96	0.00	0.00	1.00	0.96	1.00	1.00	1.00	0.96	1.00	1.00
41	1.00	0.98	0.00	0.00	1.00	0.98	1.00	1.00	1.00	0.98	1.00	1.00
42	1.00	0.93	0.00	0.00	1.00	0.93	1.00	1.00	1.00	0.93	1.00	1.00
43	1.00	0.93	0.00	0.00	1.00	0.93	1.00	1.00	1.00	0.93	1.00	1.00
44	1.00	0.87	0.00	0.00	1.00	0.87	1.00	1.00	1.00	0.87	1.00	1.00
45	1.00	0.98	0.00	0.00	1.00	0.98	1.00	1.00	1.00	0.98	1.00	1.00
46	1.00	0.86	0.00	0.00	1.00	0.86	1.00	1.00	1.00	0.86	1.00	1.00
47	1.00	0.97	0.00	0.00	1.00	0.97	1.00	1.00	1.00	0.97	1.00	1.00
48	1.00	0.84	0.00	0.00	1.00	0.84	0.98	0.99	1.00	0.84	0.98	0.99
49	1.00	1.00	0.00	0.00	1.00	1.00	1.00	1.00	1.00	1.00	1.00	1.00
50	1.00	1.00	0.00	0.00	1.00	1.00	1.00	0.99	1.00	0.99	1.00	0.99
51	1.00	0.81	0.00	0.00	1.00	0.81	1.00	0.99	1.00	0.81	1.00	0.99
52	1.00	1.00	0.00	0.00	1.00	1.00	1.00	1.00	1.00	1.00	1.00	1.00
53	0.99	0.81	0.00	0.00	0.99	0.81	1.00	1.00	0.99	0.81	1.00	1.00
54	1.00	1.00	0.00	0.00	1.00	1.00	1.00	1.00	1.00	1.00	1.00	1.00
55	0.99	1.00	0.00	0.00	1.00	1.00	1.00	1.00	1.00	1.00	1.00	1.00
56	0.99	1.00	0.00	0.00	0.99	1.00	1.00	1.00	1.00	1.00	1.00	1.00
57	1.00	0.81	0.00	0.00	1.00	0.81	1.01	1.00	1.00	0.81	1.01	1.00
58	0.99	0.99	0.00	0.00	0.99	0.99	1.00	1.00	0.99	0.99	1.00	1.00
59	1.00	1.00	0.00	0.00	1.00	1.00	1.00	1.00	1.00	1.00	1.00	1.00
60	1.00	1.00	0.00	0.00	1.00	1.00	1.00	1.00	1.00	1.00	1.00	1.00
61	1.00	1.00	0.00	0.00	1.00	1.00	1.00	1.00	1.00	1.00	1.00	1.00
62	1.00	1.00	0.00	0.00	1.00	1.00	1.00	1.00	1.00	1.00	1.00	1.00
63	1.00	1.00	0.00	0.00	1.00	1.00	1.00	1.00	1.00	1.00	1.00	1.00
64	1.00	1.00	0.00	0.00	1.00	1.00	1.00	1.00	1.00	1.00	1.00	1.00
65	1.00	1.00	0.00	0.00	1.00	1.00	1.00	1.00	1.00	1.00	1.00	1.00
66	1.00	1.00	0.00	0.00	1.00	1.00	1.00	1.00	1.00	1.00	1.00	1.00
67	1.00	1.00	0.00	0.00	1.00	1.00	1.00	1.00	1.00	1.00	1.00	1.00
68	1.00	1.00	0.00	0.00	1.00	1.00	1.00	1.00	1.00	1.00	1.00	1.00
69	1.00	1.00	0.00	0.00	1.00	1.00	1.00	1.00	1.00	1.00	1.00	1.00
70	1.00	1.00	0.00	0.00	1.00	1.00	1.00	1.00	1.00	1.00	1.00	1.00

71	1.00	1.00	0.00	0.00	1.00	1.00	1.00	1.00	1.00	1.00	1.00	1.00
72	1.00	1.00	0.00	0.00	1.00	1.00	1.00	1.00	1.00	1.00	1.00	1.00
73	1.00	1.00	0.00	0.00	1.00	1.00	1.00	1.00	1.00	1.00	1.00	1.00
74	1.00	1.00	0.00	0.00	1.00	1.00	1.00	1.00	1.00	1.00	1.00	1.00
75	1.00	1.00	0.00	0.00	1.00	1.00	1.00	1.00	1.00	1.00	1.00	1.00
76	1.00	1.00	0.00	0.00	1.00	1.00	1.00	1.00	1.00	1.00	1.00	1.00
77	1.00	1.00	0.00	0.00	1.00	1.00	1.00	1.00	1.00	1.00	1.00	1.00
78	1.00	1.00	0.00	0.00	1.00	1.00	1.00	1.00	1.00	1.00	1.00	1.00
79	1.00	1.00	0.00	0.00	1.00	1.00	1.00	1.00	1.00	1.00	1.00	1.00
80	1.00	1.00	0.00	0.00	1.00	1.00	1.00	1.00	1.00	1.00	1.00	1.00
81	1.00	1.00	0.00	0.00	1.00	1.00	1.00	1.00	1.00	1.00	1.00	1.00
82	1.00	1.00	0.00	0.00	1.00	1.00	1.00	1.00	1.00	1.00	1.00	1.00
83	1.00	1.00	0.00	0.00	1.00	1.00	1.00	1.00	1.00	1.00	1.00	1.00
84	1.00	1.00	0.00	0.00	1.00	1.00	1.00	1.00	1.00	1.00	1.00	1.00
85	1.00	1.00	0.00	0.00	1.00	1.00	1.00	1.00	1.00	1.00	1.00	1.00
86	1.00	1.00	0.00	0.00	1.00	1.00	1.00	1.00	1.00	1.00	1.00	1.00
87	1.00	1.00	0.00	0.00	1.00	1.00	1.00	1.00	1.00	1.00	1.00	1.00
88	1.00	1.00	0.00	0.00	1.00	1.00	1.00	1.00	1.00	1.00	1.00	1.00
89	1.00	1.00	0.00	0.00	1.00	1.00	1.00	1.00	1.00	1.00	1.00	1.00

As can be seen from Table 4.15, multi-group DHFs of the initial resonance materials are not sensitive to burnup. Furthermore, DHFs for most of the important TRU nuclides like Pu-239 and Pu-240 are equal to, or close to, unity throughout the burnup process as can be seen in Table 4.15. In addition, relative concentration of TRU nuclides is negligible in the VHTR fuel. Therefore, it is concluded that fuel depletion of the resonance nuclides has a negligible effect on DHFs for the resonance nuclides. The concentrations of these nuclides are insufficient to cause significant self-shielding within a fuel kernel hence the only heterogeneity that needs to be accounted for is the fuel compact heterogeneity and this is already accounted for by the original CPM3 calculation.

As can be seen in Table 4.15, DHFs, basically the self-shielding factors, may be greater than one for some resonance groups and absorbers due to resonance cross-shielding effect. If the two materials have resonances that overlap, the flux perturbation caused by each material will shield resonance reactions of the other material. The level of cross-shielding depends on the relative concentration of two absorbers as well as the specific shapes of their resonance cross sections. This is also known as resonance interference effect and was discussed by Williams[50]. It was shown that resonance shielding factors can be greater than one for some resonance groups and absorbers.

4.2.4.3 Packing Fraction Dependence

Detailed analysis of the grain shielding factor developed by Wälti [17] suggests that DHFs should mainly depend on the relative volume of the fuel kernels and moderator region (coatings + binder) in a given fuel compact cell. It was already shown that material composition has a negligible effect on the DHFs and the spatial dependence over an assembly (and core) is weak. To examine the sensitivity of the DHFs to the packing fraction, DHFs were calculated for each resonance energy group for U235 and U238 with packing fractions. Table 4.16 shows how the multi-group DHFs change as a function of packing fraction.

Table 4.16. Multi-group DHFs for U-238 as a function of kernel packing fraction.

Case #	**Packing Fraction**	**Multi-group DHFs for U-238**					
		44	**46**	**48**	**51**	**53**	**57**
1	**13.2%**	0.84	0.80	0.79	0.66	0.68	0.72
2	**14.5%**	0.83	0.81	0.79	0.68	0.69	0.72
3	**16.0%**	0.83	0.80	0.79	0.69	0.70	0.72
4	**17.5%**	0.84	0.81	0.79	0.71	0.71	0.73
5	**19.1%**	0.84	0.82	0.79	0.73	0.73	0.75
6	**20.9%**	0.85	0.82	0.80	0.74	0.75	0.76
7	**22.7%**	0.85	0.83	0.81	0.77	0.76	0.77
8	**24.7%**	0.86	0.84	0.82	0.78	0.78	0.79
9	**26.7%**	0.86	0.85	0.82	0.80	0.80	0.80
10	**28.9%**	**0.87**	**0.86**	**0.83**	**0.81**	**0.81**	**0.81**
11	**31.2%**	0.88	0.86	0.84	0.83	0.82	0.83
12	**33.6%**	0.88	0.87	0.86	0.84	0.83	0.84
13	**36.1%**	0.89	0.88	0.86	0.85	0.85	0.85
14	**38.7%**	0.90	0.88	0.87	0.86	0.86	0.86

15	**41.5%**	0.90	0.89	0.88	0.87	0.87	0.87
16	**44.4%**	0.91	0.90	0.89	0.88	0.87	0.87
17	**47.4%**	0.91	0.90	0.90	0.90	0.89	0.88
18	**50.6%**	0.92	0.91	0.90	0.90	0.89	0.89
19	**53.9%**	0.92	0.92	0.91	0.91	0.90	0.90

As can be seen, the effect of packing fraction is finite but not huge. For example, the packing fraction changes by 8% going from Case 10 to Case 11 but the DHF changes by 2%. Since the packing fraction does not change during operation, DHFs would probably be generated for each packing fraction although it may be possible to parameterize the DHFs as a function of packing fraction. This dependence can also be expressed as a function of Dancoff factor, which could account for the weak spatial dependence as well as the packing factor dependence.

CHAPTER 5

SUMMARY & CONCLUSIONS

Two of the primary challenges associated with the neutronic analysis of the Very High Temperature Reactor (VHTR) are accounting for resonance self-shielding in the particle fuel (contributing to the double heterogeneity) and accounting for temperature feedback due to Doppler broadening. The research reported in this thesis addresses both of these challenges. The double heterogeneity challenge is addressed by defining a "double heterogeneity factor" (DHF) that allows conventional light water reactor (LWR) lattice physics codes to analyze VHTR configurations. The challenge of treating Doppler broadening is addressed by a new "on-the-fly" methodology that is applied during the random walk process with negligible impact on computational efficiency. Although this methodology was motivated by the need to treat temperature feedback in a VHTR, it is applicable to any reactor design.

5.1 On-the-fly Doppler Broadening for Monte Carlo Codes

A new regression model for cross sections of any type was developed based on the Adler-Adler multi-level temperature dependent resonance representation. Furthermore, it is the only multi-level formulation based on resonance parameters in the ENDF library. The temperature dependence of the resonance model was investigated for a given nuclide and neutron energy for cross sections of any type as a function of temperature. The analysis was performed at the energy grid points of several important resonance nuclides, dividing a resonance into three sub-regions: near the peak of the resonance, near the middle of the resonance, and the wings of the resonance. The maximum relative error compared to the NJOY approach is less than $1 \mathrm{x} 10^{-9}\%$ and $1 \mathrm{x} 10^{-6}$ over the peak and mid-resonance regions respectively for U-238 in the temperature range of 77K-3200K. For the wings of the U238 resonances, the cross section difference was less than 0.1% or so but the absolute difference was negligible because the cross sections are so small in this range. This should be compared with a maximum relative difference of up to 100% for all regions with the equivalent polynomial regression model. A Monte Carlo code was implemented to apply the combined regression model to calculate the additional computing cost. It was found to be less than <1% without keeping the broadened cross sections in the memory and allowing an unlimited number of material temperatures.

5.2 Coupled Monte Carlo/Collision Probability Method for VHTR Analysis

Two related methodologies were developed to analyze VHTR configurations by the conventional advanced LWR lattice physics codes, accounting for the double heterogeneity posed by the VHTR fuel.

The initial approach involved the simultaneous execution of MCNP5 and CPM3, with direct communication of MCNP5 resonance cross sections to CPM3 during the simulation. An application program interface was implemented to provide the communication between CPM3 and MCNP5. This methodology was found to work very well, demonstrating that CPM3 (with assistance from MCNP5) is able to analyze a

VHTR assembly with TRISO fuel and yield excellent results compared with MCNP5, even though CPM3 models the TRISO fuel as a homogeneous region.

An alternative approach, based on defining a double heterogeneity factor (DHF), was developed. It yielded similar results but has substantial advantages over the direct approach for realistic VHTR analysis. DHFs, which are basically self shielding factors, were found to have important characteristics. Spatial dependence of DHFs was analyzed for two limiting assembly configurations and it was found to be negligible for both assembly configurations. Furthermore, DHFs are almost the same at the corresponding fuel compact locations between two limiting assemblies, suggesting the use of one set of multi-group DHFs for each resonance nuclide and VHTR fuel assembly at any location in the full core. Secondly, DHFs of resonance nuclides were found to be insensitive to burnup. Furthermore, DHFs for most of the important transmutation nuclides like Pu-239 and Pu-240 are equal to, or close to, unity throughout the burnup process. Since the relative concentration of transmutation nuclides is negligible in the VHTR fuel, it is concluded that fuel depletion has a negligible effect on DHFs for the resonance nuclides. As a final analysis, the dependence of the DHFs on packing fraction was investigated. Since the packing fraction does not change during operation, DHFs can be generated for each packing fraction although it may be possible to parameterize the DHFs as a function of packing fraction.

In conclusion, the DHF approach eliminates simultaneous execution of MCNP5 and CPM3. This methodology is independent of the target lattice physics code as long as it can analyze homogeneous VHTR fuel.

5.3 Future Work

A simple, accurate, and efficient closed form equation was suggested to Doppler broaden the cross sections at the energy grid points for each nucleus. Although this method appears to be a promising approach, the accuracy and efficiency of the proposed model must also be tested in production level Monte Carlo codes. Furthermore, the proposed regression model was optimized based on ENDF/B-VI library and the proposed methodology in this thesis may need to be repeated with ENDF/B-VII library for further optimization.

A new methodology based on DHFs was developed to account for double heterogeneity posed by the VHTR fuel in conventional LWR lattice physics codes. It was shown that the DHF only depends strongly on the packing fraction in a fuel compact. Therefore, it was proposed that DHFs be tabulated as a function of packing fraction to analyze the heterogeneous fuel in VHTR configuration with LWR lattice physics codes. This dependence can also be expressed as a function of Dancoff factor, which could account for the weak spatial dependence as well as the packing factor dependence.

BIBLIOGRAPHY

1. P. E. MacDonald, et al., “NGNP Preliminary Point Design – Results of the Initial Neutronics and Thermal-Hydraulic Assessments During FY-03,” *INEEL/EXT-03-00870 Rev. 1, Idaho National Engineering and Environmental Laboratory* (2003).

2. Monte Carlo Team, “A General Monte Carlo N-Particle Transport Code,” *Version 5, LA-UR-03-1987, Los Alamos National Laboratory* (2003).

3. MacFarlane, R.E. and Muir, D.W., “NJOY99.0 - Code System for Producing Pointwise and Multigroup Neutron and Photon Cross Sections from ENDF/B Data,” *PSR-480/NJOY99.00, Los Alamos National Laboratory, Los Alamos* (2000).

4. Cullen D.E. and Weisbin C.R., “Exact Doppler Broadening of Tabulated Cross Sections,” *Nuclear Science and Engineering*, **60**, pp. 199-229 (1976).

5. B. A. Hutchins et al., “ENDRUN-II, A Computer Code to Generate a Generalized Multigroup Data File from ENDF/B,” *GEAP-13704 (ENDF-145), General Electric Company, Sunny-vale, California* (1971).

6. D. M. Green and T.A. Pitterle, “ETOE, A Program for ENF/B to MC^2 Data Conversion,” *APDA-219 (ENDF-120), Atomic Power Development Associates, Inc.* (1968).

7. N. M. Greene et al., “AMPX: A Modular Code System for Generating Coupled Multigroup Neutron-Gamma Libraries from ENDF/B,” *ORNL-TM-3706, Oak Ridge national Laboratory*.

8. B. J. Toppel, A. L. Rago, and D. M. O’Shea, “MC^2 - A Code to Calculate Multigroup Cross Sections,” *Argon National laboratory report ANL-7318* (1967).

9. K. Gregson, and M. F. James, “TEMPO-A General Doppler Broadening Program for Neutron Cross Sections,” *AEEW-M518, United Kingdom Atomic Energy Establishment, Winfrith, England* (1965).

10. G. C. Panini, “Four Aces-A Program for Producing Group Averaged Cross Sections from Different Files,” *RT/F1(73)16, Comitato Nazionale Energia Nucleare* (1973).

11. ORNL, “SCALE – Version 5.1,” *Code Manual ORNL/TM-2005/39* (2006).

12. T. H. Trumbull, “Treatment of Nuclear Data for Transport Problems Containing Detailed Temperature Distributions,” *Nuclear Technology*, **156**, pp. 75-86 (2006).

13. J. L. Conlin, W. Ji, J. C. Lee and W. R. Martin, “Pseudo Material Construct for Coupled Neutronic-Thermal-Hydraulic Analysis of VHTGR,” *Trans. Am. Nucl. Soc.*, **92**, pp. 225 (2005).

14. Alessandro da Goncalves, Aquilino S. Martinez, and Fernando C. da Silva, ”Solution of the Doppler Broadening Function Based on the Fourier Cosine Transform”, *Annals of Nuclear Energy*, **35**, pp. 1878-1881 (2008).

15. L.W. Nordheim, “A New Calculation of Resonance Integrals,” *Nuclear Science and Engineering*, **12**, pp. 457-463 (1962).

16. Kim, Y.H., “Reactivity-Equivalent Physical Transformation for Elimination of Double Heterogeneity,” *Trans. Am. Nucl. Soc.*, **93**, pp. 959–960 (2005).

17. P. Wälti, “Evaluation of Grain Shielding Factors for Coated Fuel Particles,” *Nuclear Science and Engineering*, **45**, pp.321-330 (1971).

18. L. Massimo, “Physics of High-Temperature Reactors,” *Pergamon Press* (1976).

19. F.B. Brown and W.R. Martin, “Stochastic Geometry Capability in MCNP5 for the Analysis of Particle Fuel,” *Annals of Nuclear Energy,* **31**, pp. 2039-2047 (2004).

20. F. B. Brown, W. R. Martin, W. Ji, J. L. Conlin, and J. C. Lee, "Stochastic Geometry and HTGR Modeling with MCNP5," *Proc. Monte Carlo - Topical Meetin*g, American Nuclear Society (2005).

21. W. Ji, J.L. Conlin, W.R. Martin, J.C. Lee and F.B. Brown, “Explicit Modeling of Particle Fuel for the Very-High Temperature Gas-Cooled Reactor,” *Trans. Am. Nucl. Soc.,* **92**, pp. 236-238 (2005).

22. W. Ji, J.L. Conlin, W.R. Martin, and J.C. Lee, "Reactor Physics Analysis of the VHTGR Core," *Trans. Am. Nucl. Soc.* **91**, pp. 556-558, (2004).

23. W. Ji and W.R. Martin, “Determination of Chord Length Distributions in Stochastic Media Composed of Dispersed Microspheres,” *Trans. Am. Nuc. Soc.,* **96**, pp. 467-469 (2007).

24. W. Ji and W.R. Martin, “Monte Carlo Simulation of VHTR Particle Fuel with Chord Length Sampling,” *Proceedings of M&C+SNA2007, Monterey, California, April 15-19* (2007).

25. S. Fehér, J.E. Hoogenboom, P.F.A. de Leege and J. Valkó, “Monte Carlo Calculation of Dancoff Factors in Irregular Geometries,” *Nuclear Science and Engineering,* **117**, pp. 227-238 (1994).

26. U. Mäder, “Chord Length Distribution for Circular Cylinders,” *Radiation Research*, Vol. **82**, No. **3**, pp. 454-466 (1980).

27. J.A. Thie, “A Simple Analytical Formulation of the Dancoff Correction,” *Nuclear Science and Engineering*, **5**, pp. 75-77 (1959).

28. Y.A. Chao, M.B. Yarbrough and A.S. Martinez, “Approximations to Neutron Escape Probability and Dancoff Correction,” *Nuclear Science and Engineering*, **78**, pp. 89-91 (1981).

29. G.L. Olson, D.S. Miller, E.W. Larsen, and J.E. Morel, “Chord Length Distribution in Binary Stochastic Media in Two and Three Dimensions”, *J. Quant. Spectros. Rad. Transfer*, **143**, pp. 226-239 (2005).

30. E.E. Bende, A.H. Hogenbirk, J.L. Kloosterman and H. Van Dam, “Analytical Calculation of the Average Dancoff Factor for a Fuel Kernel in a Pebble Bed High-Temperature Reactor,” *Nuclear Science and Engineering,* **133**, pp. 147-162 (1999).

31. A. Talamo, “Analytical Calculation of the Average Dancoff Factor for Prismatic High-Temperature Reactors,” *Nuclear Science and Engineering,* **156**, pp. 343-356 (2007).

32. D. B. Jones and K. E. Watkins, “CPM-3 Computer Code Manual, Volume 1: Theory and Numerics Manual," *EPR-CPM-001-M-001, Rev. A, Electric Power Research Institute* (2000).

33. R. J. J. Stamm’ler, M. J. Abbate, “Methods of Steady-State Reactor Physics in Nuclear Design,” *Academic Press, London* (1983).

34. I. Carlvik, “Collision Probabilities for Finite Cylinders and Cuboids,” *Nuclear Science and Engineering*, **30**, pp. 150-151 (1970).

35. Spanier, J. and Oldham, K. B. "An Atlas of Functions,” *Hemisphere Publishing Corporation* (1987).

36. R. R. Coveyou, R. R. Bate, and R. K. Osborn, “Effect of Moderator Temperature Upon Neutron Flux in Infinite, Capturing Medium”, *Journal of Nuclear Energy*, **2**, pp. 153-167 (1956).

37. T. Hogberg, “Monte Carlo Calculations of Neutron Thermalization in a Heterogeneous System”, *Journal of Nuclear Energy*, **12**, pp. 145-150 (1960).

38. W. E. Lamb, Phys. Rev, **55**, 190 (1939).

39. Deokjung Lee, Kord Smith, and Joel Rhodes, "The impact of ^{238}U resonance elastic scattering approximations on thermal reactor Doppler reactivity," *Annals of Nuclear Energy*, **36**, pp. 274-280 (2009).

40. Ouisloumen, M., Sanchez, R., "A Model for Neutron Scattering off Heavy Isotopes that Accounts for Thermal Agitation Effects," *Nucl. Sci. Eng.* **107**, 189–200 (1991).

41. Becker, B., Dagan, R., Broeders, C. H. M., Lohnert, G. H., "Improvement of the Resonance Scattering Treatment in MCNP in View of HTR Calculations," *Annals of Nuclear Energy*, 36, pp. 281-285 (2008).

42. Stephen A. Dupree and Stanley K. Fraley, "A Monte Carlo Primer," *Kluwer Academic Publishers Group* (2001).

43. J. W. Sterbentz, B. Phillips, R. L. Sant, G. S. Chang, and Paul D. Bayless, "Reactor Physics Parametric and Depletion Studies in Support of TRISO Particle Fuel Specification for the Next Generation Nuclear Plant," *INEEL/EXT-04-02331, Idaho National Engineering and Environmental Laboratory* (2004).

44. Studsvik Scandpower, "Helios Methods v.1.9," (2005).

45. D. B. Jones and K. E. Watkins, "CPM-3 Computer Code Manual, Volume 5: Nuclear Data Manual," *EPR-CPM-001-M-005, Rev. A, Electric Power Research Institute* (2000).

46. Mosteller, R.D, LANL, *Private Communication* (2009).

47. Carmelo Rodriguez, Francesco Venneri, Alan Baxter, Donald McEachern, "Transmutation of Nuclear Waste in MHRs," *Universities reception at Reno* (2001).

48. Alberto Talamo, Waclaw Gudowski, Jerzy Cetnar, Francesco Venneri, "Key Physical Parameters and Temperature Reactivity Coefficients of the Deep Burn Helium Reactor Fueled with LWRs Waste," *Annals of Nuclear Energy*, **31**, pp. 1913-1937 (2004).

49. Tucker, B. "Deep Burn Design Parameters," *Excel Worksheet.*

50. M.L. Williams, "Correction of Multigroup Cross Sections for Resolved Resonance Interference in Mixed Absorbers," *Nuclear Science and Engineering*, **83**, pp. 37-49 (1983).